Fabio Barbosa Louza

Low probability of detection underwater acoustic communications

University of Algarve

Faculty of Sciences and Technology

2022

Fabio Barbosa Louza

Low probability of detection underwater acoustic communications

Ph.D. Thesis in Electronics and Telecommunications (Signal Processing)

Developed under supervision of:

Prof. Dr. Sérgio Manuel Machado Jesus

University of Algarve

Faculty of Sciences and Technology

2022

Low probability of detection
underwater acoustic communications

Declaração de autoria do trabalho

Declaro ser o autor deste trabalho, que é original e inédito. Autores e trabalhos consultados estão devidamente citados no texto e constam da listagem de referências bibliográficas incluída.

Fabio Barbosa Louza

À minha amada Cristiane
Ao meu filho Pedro Henrique

&

Aos meus Pais Nilton e Angela

Acknowledgements

This work has been a long journey involving several special persons to whom I must forward my appreciation. Thank you, God for your blessings and support to overcome the challenges of this work. To Our Lady of Fátima, and Saint Jude Thaddaeus, thanks for your silent support during my numerous prays.

I would like to appreciate my advisor Prof. Sergio Jesus for his encouragement, guidance, and friendship. During this 3-year Ph.D., he was always available to my questions and doubts, providing fundamental suggestions for this work.

I appreciate all my colleagues at the Signal Processing Laboratory (SiPLab) for their friendship, scientific discussions, and support, especially Prof. Orlando Rodriguez, Ricardo Duarte, and Giulia Spadoni. I am also grateful to my Brazilian Navy friend Lieutenant Fabricio Bozzi and his wife Lorana, for their friendship and for sharing nice moments during this time in Portugal.

To my friend Prof. Harry DeFerrari from the University of Miami (RSMAS), my appreciation for his contributions to this work.

From the Brazilian Navy Institute of Sea Studies "Admiral Paulo Moreira" (IEAPM), I would like to appreciate Mrs. Eliane Gonzalez (Director), Captain Marcus Simões, and other colleagues for their friendship, and support. I am also grateful for the sponsorship provided by the Brazilian Navy through the Postgraduate Study Abroad Program, Grant No. Port.227/MB/2019. I am deeply honored by the trust placed in me to carry out this challenging course.

To all my Portuguese friends, thank you so much for your friendship.

Now, it is time to appreciate the most important people in my life. To my parents Nilton and Angela, my gratitude and most deep appreciation. Your faith that only education could lead me to success was right. I will always love you. To my brothers Marcelo and Isabel, thanks for your love, encouragement, and support. To my mother-in-law Neusa, thanks for your love and care. To my grand-aunt Arminda (in memoriam), a former teacher, for her guidance and love. To my family and friends in Brazil, my deep appreciation.

Last but most important, I appreciate my beloved wife Cristiane and my son Pedro Henrique. This time in Faro has been a great challenge for all of us. Far from home, and facing the Covid-19 pandemic, we proved that we are stronger together. Your unconditional love, patience, support, and encouragement were fundamental for the success of this work. I will love you forever!!! Now, it's time to go back home full of wonderful memories in our minds and friends in our hearts.

Name: Fabio Barbosa Louza
College: Faculty of Sciences and Technology
University: University of Algarve
Supervisor: Sérgio Manuel Machado Jesus, Professor
Thesis title: Low probability of detection underwater acoustic communications

Abstract

Low probability of detection (LPD) underwater acoustic communications are an essential requirement for command and control of autonomous underwater vehicles (AUV) or submarines performing covert missions, avoiding their detection while communicating. Based on low power signals, these covert communications may also extend the autonomy of battery-operated AUVs, and contribute to reducing the impacts of the environmental noise level on marine life. The present thesis aims to develop LPD communications based on modeled and real data from three shallow water experiments. Thus, a superimposed training method has been proposed. A bitstream is created superimposing a long probe to the message before transmission. Computationally simple, the algorithm explores temporal diversity to increase the processing gain and uses a Wiener filter for equalization. Experimental results presented bit-error rates (BER) $< 10^{-2}$ for signal-to-noise ratios (SNR) < -8 dB. To understand the effects of coastal upwelling phenomena over low SNR communications, a study compares the acoustic propagation for different sound speed profiles using a propagation model and analyzes data from the BioCom'19 experiment, performed off Cabo Frio Island (Brazil). Temporal and spatial coherence of low power signals propagating in this harsh environment are estimated, and both a criterion for multichannel combining and a double Wiener filter to improve equalization are presented. Passive time-reversal (pTR) techniques have been widely employed for communications. To address the pTR channel mismatch due to the environmental variability between the probe and the data transmissions, this work proposes a superimposed training pTR (STpTR) approach for single and multichannel systems. Despite the high noise levels, varying from -5 to +6 dB, the STpTR combined with a Wiener filter achieved BER $< 10^{-2}$, for bit rates up to 220 bps. To improve covert communications for AUVs, this work also presents a study about vector sensor multichannel combining. Using the STpTR approach, results from an experiment on the coast of Algarve/Portugal indicate that combining the pressure and particle velocity channels of a vector sensor may provide an average SNR and mean squared-error gain of up to 9.4 and 3.1 dB, respectively, compared to the pressure channel. Therefore, a better understanding of the environment combined with the superimposed training pTR using a vector sensor may improve the LPD communication system's performance and robustness while keeping covertness.

Keywords: Low probability of detection, underwater acoustic communications, superimposed training, coastal upwelling, passive time-reversal, vector sensor.

Nome: Fabio Barbosa Louza
Faculdade: Faculdade de Ciências e Tecnologia
Universidade: Universidade do Algarve
Orientador: Sérgio Manuel Machado Jesus, Professor Catedrático
Título da Tese: Comunicações acústicas submarinas com baixa probabilidade de detecção

Resumo

No últimos anos, os trabalhos de investigação sobre comunicações acústicas submarinas com baixa probabilidade de detecção (BPD) tem sido incentivados pela indústria, pelos governos, e pela própria academia em razão de suas múltiplas aplicações. Na área militar, as comunicações BPD permitem que submarinos e veículos autônomos possam se comunicar sem serem detectados. Na área civil, permitem a economia de energia de sensores alimentados por baterias, aumentando o tempo de funcionamento, bem como contribui para reduzir os impactos sobre a vida marinha causados pelos altos níveis de ruído submarino, entre outras aplicações. Neste contexto, esta tese pretende desenvolver comunicações BPD utilizando um modelo de propagação acústica e dados obtidos a partir de três experimentos em águas rasas.

Este trabalho apresenta um método de treinamento superposto para comunicações submarinas em um ambiente com baixa relação sinal/ruído, e demonstra sua aplicação para comunicações BPD. Computacionalmente simples, o método foi desenvolvido para funcionar com um único projetor acústico, transmitindo com baixa potência, e um hidrofone, sem o ganho de um arranjo de sensores distribuídos no espaço. Antes da transmissão, uma longa sequência de comprimento máximo é somada à mensagem para efeitos de equalização e sincronismo. Os dois sinais são binários, modulados em fase e possuem 2047 bits. Porém, possuem amplitudes diferentes. Na realidade, a amplitude do sinal de treinamento é ligeiramente superior à da mensagem. Em um ambiente com baixa relação sinal ruído, um sinal de treinamento mais forte permite ocultar a mensagem a ser transmitida, bem como melhorar o ganho para a estimação da resposta impulsiva e para a sincronização do sistema. A mensagem é composta por 3 bits nulos e 4 sequências de 511 bits. Delimitados por uma curta sequência de comprimento máximo de 31 bits, para dupla sincronização, os pacotes de dados possuem 480 bits e transportam o seguinte pangrama: (The Quick Brown Fox Jumps Over the Lazy Dog 0123456789!@#$). O método explora a diversidade temporal do canal, transmitindo a mesma sequência diversas vezes para aumentar o ganho de processamento do sinal e implementar a correção de erros através da soma coerente dos sinais. A resposta impulsiva do canal é estimada pela transformada rápida de Hadamard, e a equalização do sinal é feita por um filtro de Wiener. A remoção da interferência causada pelo sinal de treinamento é realizada pelo método "hyperslice cancellation by coordinate zeroing (HCC0)", e a seguir a mensagem é decodificada. Resultados obtidos a partir de um experimento em águas rasas, utilizando uma fonte e um único hidrofone, apresentaram taxas de erro de bit menores que 10^{-2}, para relações sinal/ruído inferiores a -8 dB.

A ressurgência costeira é um fenômeno oceanográfico dinâmico que modifica, profundamente, a estratificação de temperatura do oceano, influenciando diretamente na propagação acústica. Por outro lado, os crescentes níveis de ruído antropogênico não apenas reduzem o desempenho dos sistema de comunicação, corrompendo a informação transmitida, mas

também afetam a vida marinha. Para compreender os efeitos da ressurgência costeira sobre as comunicações com baixa relação sinal/ruído, um estudo analisa os dados do experimento BioCom'19, realizado nas proximidades da Ilha do Cabo Frio, Rio de Janeiro (Brasil). As respostas impulsivas do canal e a propagação acústica, para diferentes perfis de velocidade do som, foram estimadas usando o modelo de propagação acústica "Monterey-Miami Parabolic Equation model (MMPE)". Além disso, o desempenho do sistema de comunicações foi correlacionado com os perfis de temperatura durante o experimento. Os resultados obtidos indicam uma significativa redução da energia acústica nos receptores durante a ressurgência, degradando o desempenho do sistema.

A coerência temporal e espacial dos sinais de baixa potência transmitidos no experimento BioCom'19 foi estimada, e um critério para combinação dos sinais, provenientes dos múltiplos hidrofones, foi proposto. Utilizando dados de um arranjo piramidal e um arranjo vertical linear, de 4 hidrofones cada, a coerência foi estimada antes e depois do filtro de Wiener para mostrar o impacto do multicaminhamento sobre a taxa de erro de bit. Os resultados mostram que a coêrencia temporal pode ser utilizada como critério para combinar sinais consecutivos em um mesmo canal, enquanto a diversidade espacial permite a combinação de múltiplos canais do arranjo de sensores. Sequências cuja coerência temporal esteja acima de um limite pré-definido são somadas. A coerência espacial entre canais foi estimada e comparada em termos da taxa de erro de bit. Para diferentes taxas de transmissão, as taxas de erro de bit estão em concordância com a evolucão da coerência espacial. Quanto mais elevada a coerência, melhor o desempenho e menor a taxa de erro de bit.

Um duplo filtro de Wiener para melhorar a equalização dos sinais de baixa potência, durante a ressurgência, tambem foi proposto. Utilizando dados dos 4 hidrofones de um arranjo piramidal, as respostas impulsivas foram estimadas para observar a variabilidade das condições de propagação. Em uma condição de perfil de temperatura isotérmico, as respostas impulsivas apresentaram multicaminhamento curto, com chegadas mais fortes nos receptores. À medida que a ressurgência ocorria, foram observadas quedas abruptas de temperatura superiores a 10°C, na posição dos hidrofones, acarretando uma forte refração da onda sonora para o fundo marinho. Em consequência, sinais mais fracos foram observados nos hidrofones. Os resultados obtidos com dados do BioCom'19 mostram que, para uma relação sinal/ruído variando entre -3.9 e 7.3 dB, o duplo filtro de Wiener forneceu um ganho do erro médio quadrático de até 2.8 dB, comparado com o filtro de Wiener simples.

As técnicas de tempo reverso passivo (TRP) tem sido amplamente empregadas nas comunicações submarinas. Porém, as rápidas alterações das condições de propagação em canais submarinos variantes no tempo, durante as transmissões da sequência de treinamento e da mensagem, degradam o desempenho das técnicas TRP de equalização. Assim, esse trabalho propõe um método de TRP utilizando treinamento superposto, para sistemas com um ou múltiplos sensores. O método proposto utiliza uma sequência de treinamento, com o efeito Doppler corrigido, para estimar o canal e realizar o TRP. O método compara 3 differentes estratégias para melhorar a performance do sistema de comunicação: a diversidade temporal devido aos sinais idênticos transmitidos continuamente, a diversidade espacial devido aos 2 arranjos de hidrofones, piramidal e linear, com 4 hidrofones cada um, além da combinação dos 2 arranjos (8 hidrofones). Neste método, a técnica de TRP com treinamento superposto minimiza o multicaminhamento e realiza a correção de erros através da soma coerente dos diferentes canais. A interferência intersimbólica residual é removida pelo filtro de Wiener. Resultados obtidos com dados do experimento BioCom'19 mostram que o método proposto pode fornecer um ganho do erro médio quadrático de até 1.62 dB para canais

independentes, e 3.13 dB, para canais combinados, comparativamente ao método sem o TRP, usando apenas o filtro de Wiener. Neste contexto, o método de TRP utilizando treinamento superposto alcançou taxas de erro de bit $< 10^{-2}$ para uma relação sinal ruído, na banda de transmissão, variando entre -5 a $+6$ dB.

Focado em comunicações com baixa probabilidade de detecção para pequenos veículos submarinos, este trabalho também apresenta um estudo sobre a combinação dos canais de pressão e velocidade de partícula dos sensores vetoriais. Os sensores vetoriais possuem pequenas dimensões, adequadas à utilizacão em veículos autônomos, e permitem obter um ganho de diversidade para as comunicações BPD. Para testar o método de treinamento superposto com o tempo reverso passivo utilizando sensores vetoriais, um experimento foi realizado, em águas rasas, na costa do Algarve/Portugal. Para reduzir a relação sinal/ruído para uma faixa de 0 a -10 dB, foi adicionado ruído gravado no experimento. Os resultados experimentais indicam que a combinação dos canais podem fornecer um ganho da relação sinal/ruído e do erro médio quadrático de até 9.4 e 3.1 dB, respectivamente, comparados com os resultados do sensor de pressão.

Portanto, as principais contribuições dessa tese são (i) a proposta do método de treinamento superposto para comunicações com baixa probabilidade de detecção, (ii) a compreensão dos efeitos da ressurgência costeira sobre as comunicações, e seus impactos sobre a coerência temporal e espacial, (iii) o método de treinamento superposto em conjunto com o tempo reverso passivo para lidar com a variação do canal entre o tempo de recepção do sinal de treinamento e da mensagem, e (iv) a combinação dos múltiplos canais dos sensores vetoriais para comunicações BPD. Dessa forma, uma melhor compreensão do canal submarino e a utilização dos métodos propostos combinados com sensores do estado da arte, como os sensores vetoriais, se configura como um avanço neste campo do conhecimento, permitindo aumentar a robustez do sistema BPD, bem como reduzir a probabilidade de detecção, mantendo a ocultação das comunicações.

Palavras-chave: Comunicações submarinas, baixa probabilidade de detecção, filtro de Wiener, coerência, tempo reverso passivo, sensores vetoriais.

Contents

List of Acronyms

AUV Autonomous Underwater Vehicle

AWGN Additive White Gaussian Noise

BER Bit Error Rate

BPSK Binary Phase Shift Keying

CIR Channel Impulse Response

CTD Conductivity, Temperature and Depth

DFE Decision Feedback Equalizer

DSSS Direct Sequence Spread Spectrum

FFT Fast Fourier Transform

FHT Fast Hadamard Transform

FSK Frequency Shift Keying

HCC0 Hyperslice Cancellation by Coordinate Zeroing

IEAPM Brazilian Navy Inst. of Sea Studies "Adm. Paulo Moreira"

ISI Intersymbol Interference

LPD Low Probability of Detection

LPI Low Probability of Interception

MMPE Monterey-Miami Parabolic Equation model

MSE Mean Squared Error

MSeq M-sequence

OFDM Orthogonal Frequency Division Multiplexing

PA Pyramidal Array

PTR Passive Time Reversal

SCOH Spatial Coherence

SNR Signal-to-Noise Ratio

SSP Sound Speed Profile

STPTR Superimposed Training Passive Time Reversal

TCOH Temporal Coherence

TL Transmission Loss

VLA Vertical Linear Array

VS Vector Sensor

List of Figures

List of Tables

Chapter 1

Introduction

Abstract *This chapter presents an overview of underwater acoustic communications, and introduces the concept of low probability of detection communications, describing the state-of-the-art in the field. Furthermore, it shows the motivation of this work and states the objectives that have guided the research. Section 1.1 introduces underwater acoustic communications, the main challenges, restrictions, and the state-of-the-art in the field. Section 1.2 introduces the concept of low probability of detection communications, and the most common approaches for covert communications. The motivations of this thesis are detailed in Section 1.3. The main objectives and goals of this work are stated in Section 1.4. Section 1.5 presents the thesis outline.*

1.1 Underwater acoustic communications

"If you cause your ship to stop and place the head of a long tube in the water and place the outer extremity to your ear, you will hear ships at a great distance from you."

Leonardo da Vinci, 1490

Wireless underwater acoustic communications may be traced back to the time of Leonardo Da Vinci. Listening on a long tube submerged in the water, Da Vinci observed that ships could be heard at great distances. Since then, the idea of using sound to transmit information underwater, eliminating the physical connection of tethers, has been explored for multiple

purposes such as acoustic telemetry from environmental monitoring sensors, ocean mapping, remote control of valves in the oil industry, communications between divers, command and control of submarines or autonomous underwater vehicles, and underwater networks [1].

The main reason for using acoustic waves is that both radio and optical communication systems have severe restrictions to operate in the sea. Radio communication systems have been exhaustively researched using extremely (3 Hz - 3 KHz) and very low frequency (3 kHz - 30 kHz), named ELF and VLF, to communicate with submerged receivers. However, electromagnetic waves are strongly attenuated as they propagate through the ocean [2]. Research from the US Navy has shown that despite ELF and VLF waves can propagate with low attenuation, a communications system requires a high-power land station to transmit the signal, and a large receiving antenna at the receiver end, limiting the system's applicability. The use of full electromagnetic bandwidth to achieve long ranges at high data rates is impractical. An overview of radio communications in the ocean and current research projects may be found in [3].

On the other hand, underwater optical communications, using laser, can provide high data rates, in the order of Megabits, but the range is limited up to a few hundred meters. Optical waves are less affected by attenuation but scattering is a serious issue. Optical communications require line-of-sight between transmitter and receiver, high precision in pointing the laser beams, and depends on the turbidity of the water. The most recent advances in underwater optical wireless communications may be found in [4].

The sound travels through the water much more effectively than radio and optical waves. However, the ocean is considered one of the most complex environments for communications [5]. The time-space varying ocean waveguide poses numerous problems for signal

transmission. Regarded as the most significant environmental issue, multipath propagation causes intersymbol interference (ISI), degrading communication performance. Multipath is mainly due to the multiple reflections of the sound wave from the sea surface and the bottom, but can also be caused by the refraction of the sound wave [5, 6]. The time-varying multipath structure depends on several factors such as the channel geometry, sound speed profile, source/receiver depths, range, and frequency of the signals amongst others. Attenuation increases with frequency, limiting bandwidth and data rate. The ambient noise due to both natural and man-made sources also corrupts information being transmitted. Furthermore, Doppler shift generated by movements between transmitters and receivers, and Doppler spread due to currents and channel reverberation modify the transmitted signals' frequency and bandwidth [6, 7].

Since World War II, underwater acoustic communications have been studied for military applications. One of the first underwater communication systems was an underwater telephone developed in the United States for communicating with submarines, which still exists nowadays in most military vessels. Using a single-sideband suppressed carrier amplitude modulation, in the frequency range from 8-11 kHz, the telephone was capable of communicating over several kilometers. In the 60's, most systems were based on non-coherent detection methods [7]. Due to the predominantly linear nature of propagation, most of the frequency content of transmitted signals remains within its original band whereas the amplitude and phase of the coherent signals can vary in time and space due to reverberation effects and ocean properties fluctuations, leading to the use of incoherent modulations. To deal with ISI, a guard time between consecutive signals is inserted to ensure that reverberation and multipath vanish before the next pulse. Thus, these non-coherent systems

even presenting poor spectral efficiency and low bit rates are still used when robustness is the main requirement of the system [7]. In recent years, several bandwidth-efficient phase-coherent communication systems have been proposed and tested at sea [8, 9]. In contrast to incoherent receivers that avoid the ISI effects of reverberation, coherent receivers must actively mitigate it to preserve a reliable phase reference [7]. Exploring temporal and spatial diversity, multichannel equalizers improve signal demodulation [8]. Non-adaptive equalizers attempt to undo distortions to the signal caused by the multipath propagation, designing an inverse filter. Meanwhile, multiple receiver elements in an array minimize the likelihood of a simultaneous signal fading in all channels [9], improving signal demodulation. Equalization techniques for underwater acoustic communications have been discussed in [8, 10, 11], but the architecture is based on a phase-locked loop (PLL) to track signal phase shifts, followed by a decision feedback equalizer (DFE). However, the DFE+PLL equalizer presents reduced performance when dealing with fast time-varying channel impulse responses (CIR) [8].

Significant advancements have been made in the development of underwater acoustic communication systems in terms of their operational range, data throughput, and reliability. Several applications, both commercial and military, are calling for real-time communication with submarines and autonomous underwater vehicles. However, most systems require high signal-to-noise ratios (SNR) to work properly. In recent years, concerns about the impacts of man-made underwater noise on marine life, and the need to communicate with submarines and underwater vehicles covertly have led to a relatively new field of studying, and the core of this thesis: the low probability of detection underwater acoustic communications.

1.2 Low probability of detection communications

Covert or LPD communications have been conceived in the radio-frequency (RF) domain, for military purposes, and extended to the underwater channel. The main goal is to allow communication in a maximal range while minimizing the probability of detection by an illegitimate receiver [12, 13]. In military applications, LPD communications have the potential to keep submarines and autonomous underwater vehicles (AUV) undetected while communicating to other submarines, surface vessels, or underwater network nodes [12, 13]. Covert communications also have civilian applications including environmental monitoring telemetry, underwater sensor networking, and command and control of AUVs [12]. Several assumptions must be made to perform an LPD experiment and analyze data. The LPD properties from the legitimate receiver and interceptor perspectives differ depending on the range to the source or to the interceptor capabilities. Assuming that the eavesdropper does not have previous knowledge about the signal, detection of the low SNR signals relies on an energy detector. However, literature about covert communications shows that it is unfeasible to guarantee a covertness of 100% [13]. Thus, estimating the LPD capability of a communication system has been proposed in several papers [14, 15]. Performed at very low SNR (SNR< -8 dB) [16], in the transmission frequency band, most of the solutions, brought from the RF channel [17], are not adequate. The LPD concept for underwater acoustic communications presents several challenges. The rapid signal fluctuation in time and space, the long multipath delay spread, the Doppler shift induced by the motion of the sensors and the sea surface, and the high noise levels due to human and biological activities are factors that severely degrade low power signal demodulation, motivating new signal pro-

cessing approaches [7, 12, 18, 19]. Thus, in an attempt to improve the performance, a mix of concepts for digital communications such as Direct Sequence Spread Spectrum (DSSS), Orthogonal Frequency Division Multiplexing (OFDM), and time-reversal have been employed and tested at sea [13, 16, 20–22]. Furthermore, mimicking marine mammals has also been tried to disguise the signals, reducing the probability of detection.

1.2.1 Direct Sequence Spread Spectrum

Most common state-of-the-art low SNR coherent-modulated communication systems are based on direct-sequence spread-spectrum (DSSS) [12, 21–23]. The symbols are spread by a code sequence, typically an M-sequence, resulting in a wideband signal [24]. Assuming that the receiver shares the same code, the matched filter can compress the signal, and bring it above the noise level. The matched filter pulse compression provides a SNR gain equal, in theory, to the time-bandwidth product of the spreading code, permitting message retrieval for low SNR [23]. Considering that the spreading code is unknown to any unauthorized receiver accessing the communication network, a low probability of interception (LPI) is said to be achieved with DSSS modulation, transmitting at low power levels [21, 23]. DSSS permits multi-access communications due to several possibilities of orthogonal spreading codes that avoid mutual interference between users. However, there is an inevitable tradeoff between the data rate and the SNR. Operating at low data rates, DSSS exploits frequency diversity and benefits from the spreading gain in a low SNR environment to improve the communication system performance [21, 25]. Some drawbacks are the reduced data rate due to the length of the spreading code, high Doppler sensitivity, and difficult synchronization. Furthermore, multipath degrades codes orthogonality causing inter-chip and inter-symbol

interference. In [23], two methods using DSSS combined with pTR are presented for single receivers. Signals were recorded at sea with high SNR and added ambient noise to simulate low power signals. Using time-updated CIR as a matched filter, the methods achieved similar performance, yielding BER $< 10^{-2}$ at -12 dB input SNR. DSSS and a coherent RAKE receiver were also investigated to design spreading waveforms that can cope with the frequency selective nature of the underwater channel, and also have properties for LPD communications [21]. Adding additive white Gaussian noise (AWGN) to the data, the scheme achieved BER $< 10^{-2}$ for a SNR varying between -7 and -9 dB. The data rate was 156.25 bps. A study on adaptive modulation for low SNR/covert communications based on a set of DSSS signals is presented in [22]. The authors proposed a channel estimate-based DFE and boosted trees for adaptive modulation. The data rate varied from 13 to 116 bps. Using AWGN to reduce the SNR at the receiver, BER lower than 10^{-2} using binary phase-shift keying (BPSK) at -5 dB were achieved. In another work, focused on bio-friendly communications, the authors presented a spread spectrum M-ary orthogonal code keying (M-OCK) modulation [25]. Based on recordings from a sea trial, with SNR adjusted by adding AWGN, the scheme achieved BER $< 10^{-3}$ for a SNR $= -14$ dB, and a data rate of 35.63 bps.

1.2.2 Orthogonal Frequency Division Multiplexing (OFDM)

The orthogonal frequency division multiplexing (OFDM) is another technique explored for covert underwater communications [13, 20, 26]. A relatively simple implementation of the OFDM system and its capability to transmit efficiently over long time spread channels has motivated the research. The need for a long symbol duration at each sub-band permits a

reduction of the source level. In the form of multicarrier modulation, OFDM finds application in highly dispersive channels, achieving high data rates in frequency selective environments. OFDM allows overlapping between subcarriers, improving bandwidth efficiency. The data is sent using several subcarriers, after multiplexing. Therefore, the system may achieve high data rates. Furthermore, modulation/demodulation techniques using Fourier transforms are computationally efficient. However, channel variability within the symbol period may cause a loss of orthogonality among subcarriers. Doppler is an issue and must be compensated to improve acquisition and synchronization, before equalization. In [20], the authors proposed an OFDM system for covert communications, achieving 4.2 and 78 bps for SNR lower than -16 and -8 dB, respectively, for ranges up to 52 km.

1.2.3 Time-reversal processing

Time-reversal (TR) techniques are commonly used for low SNR communications, and therefore, may be extended to covert communications. Based on wave backpropagation, time-reversal exploits the reciprocity of linear wave propagation to achieve spatial and temporal focusing of the sound energy, at desired points in the waveguide, with little knowledge about the channel [10]. Generally divided into active (aTR) and passive time-reversal (pTR), the TR approach is quite simple and has attracted attention after some experiments have shown its feasibility in the ocean waveguide [9].

Active time reversal focusing may be achieved by transmitting a probe from a point source to an array of receivers, which sample the acoustic pressure field. The distorted signals, recorded by each receiver element, are then time-reversed, convolved to the data waveform, and retransmitted back to the source. Therefore, a replica of the acoustic field converges

at the source position, and approximately regenerates the original waveform, mitigating multipath [10]. Due to the focusing of the acoustic energy, active time-reversal achieves a high signal-to-noise ratio (SNR) at the intended receiver with a low probability of interception elsewhere [18,27]. The array is typically composed of several acoustic receivers and collocated sound sources. Due to its retroreflective ability to receive and retransmit the time-reversed signals, the array is commonly known as a time-reversal mirror (TRM) [9,28]. Assuming that the ocean environment is reasonably stable, not changing much during the signal round-trip travel time, the focus results from recombination of the multipath structure impinged to the signal in both ways [9]. The focalization is a consequence of the capability of the channel to deconvolve itself. Thus, no previous knowledge about the environment is necessary.

Passive time-reversal (pTR) techniques have been widely used for high multipath underwater communications in shallow water [9, 10, 18, 27, 29]. PTR usually relies on a spatio-temporal matched filter estimated by a probe sent before the data and requires a receiver array. In the absence of noise and considering that neither the channel oceanographic structure nor the geometry between source and receiver has changed in the time interval between the probe and the message, the received probes can be time-reversed and used to filter the message. To eliminate residual intersymbol interference (ISI), pTR is usually followed by an adaptive filter, typically a decision feedback equalizer (DFE) with a phase-locked loop [8, 29, 30]. However, DFE may be computationally intensive depending on the adaptation algorithm, and may also present a poor performance in a low SNR environment, due to significant uncertainties in channel estimation and imprecise synchronization [23]. In the case of moving platforms and variable source-receiver geometries, especially in a fast time-varying ocean waveguide where coherence time may be short, the classic approach of pTR

sending the probe ahead of data may not be able to cope with the environmental mismatch between the probe and the message transmissions, even at high SNR [10, 27, 29]. Therefore, an environmental model-based time-reversal is proposed in [31]. The estimated noisy channel impulse responses (CIR) were replaced by time-updated and noiseless CIR replicas computed by a ray-tracing model. An extension of the pTR technique to adaptively weight receiver contributions to compensate for degraded focusing due to the geometrical mismatch between the probe and data is presented in [10]. The interested reader is referred to [29] for an overview of time-reversal communications.

1.2.4 Marine mammals mimicking

Most LPD communication systems using DSSS and OFDM must operate at low SNR, below the environmental noise, to avoid detection by an eavesdropper. However, to take advantage of the ambient noise and to trick the eavesdropper, biologically inspired communications mimick marine mammals' sounds, being not restricted to low-power signals. The mimicked clicks and whistles can be detected but as they are recognized as marine mammals, they are not classified as an enemy. In [32], a scheme is proposed to mimic dolphin whistles by continuously varying the carrier frequency and by using antipodal symbol modulation. In [33], dolphin clicks were used to disguise the intended message. Employing a RAKE receiver, the system achieved BER $< 10^{-4}$ at 37 bps, in a lake experiment. Therefore, this technique presents LPI characteristics and has been studied for military applications.

1.3 Motivation

Research on low probability of detection underwater acoustic communications has been encouraged, in recent years, by governments, industry, and academia due to its multiple applications. Mostly based on low signal-to-noise ratio (SNR) signals, LPD communications may be used to keep submarines, autonomous underwater vehicles, and network nodes undetected while communicating. The increasing use of battery-operated AUVs to perform long-term missions requires low power demanding telemetry for coordination between multiple platforms, with reduced mutual interference, and for command and control between the AUVs and the operational center. Thus, both the autonomy and the operating range of the moving platforms may be extended. Furthermore, raising concerns about the increasing anthropogenic noise levels and their impact on marine life has led to strict legislation in several countries to limit the transmitted acoustic power in the ocean. Therefore, bio-friendly LPD communications may also contribute to the field, minimizing possible interference with marine mammals vocalizations and mitigating issues to marine life caused by the exposure to excessive acoustic power signals. However, establishing reliable LPD coherent communications in shallow water is a challenging task. The rapid signal fluctuation in time and space, the long multipath delay spread, the Doppler shift induced by the motion of the sensors and the sea surface, and the high noise levels due to human and biological activities are factors that severely degrade low power signal demodulation, motivating new signal processing approaches.

Most common systems for covert communications rely on a single or on an array of hydrophones for multichannel combining to increase the SNR at the receiver. However, these

large-size arrays are not suitable for autonomous platforms, such as AUVs. Compact in size, the acoustic vector sensors measure both the scalar acoustic pressure and the orthogonal particle velocities in a co-located device. Despite providing diversity gain, acoustic vector sensors just recently started being explored for underwater communications. Studies about the use of vector sensors for LPD communications are still limited. Therefore, this thesis may contribute to the field, proposing new methods for LPD communications, and exploring the VS multichannel combining to improve the system robustness, while keeping covertness.

1.4 Objectives

The primary objective of this thesis is to develop low probability of detection underwater acoustic communications in shallow water. To reach this main goal, specific objectives were stated to guide the research:

i) to improve research about superimposed training, fast Hadamard transforms (FHT) and hyperslice cancellation by coordinate zeroing (HCC0), in order to develop a method for covert communications using a fixed single source/receiver network node;

ii) to study passive time-reversal techniques to reduce the equalization complexity, and to understand how the superimposed training method may reduce the pTR channel mismatch in the time interval between the probe and the message transmissions for multiple receivers;

iii) to study the acoustic propagation and signal coherence in fast time-varying shallow water channels;

iv) to study the impacts of upwelling oceanographic phenomena over low SNR acoustic communications;

v) to study the acoustic vector sensors, to understand the relationship between the pressure and particle velocity channels, and to implement multichannel combining, increasing the SNR at the moving receiver;

vi) to study communication covertness from both a legitimate receiver, and an interceptor perspective.

1.5 Thesis Outline

The thesis is organized into 8 chapters.

Chapter 2 presents the simulation scenario used for LPD communications, and describes the methodology adopted in this thesis. Chapter 3 presents a superimposed training method, suitable for LPD communications using a single source/receiver in shallow water. Chapter 4 presents a study about the effects of coastal upwelling over acoustic propagation in shallow water and their impacts on communications. Chapter 5 presents a study about temporal and spatial coherence over communications in a fast time-varying channel and proposes a double Wiener filter to mitigate intersymbol interference in such channels. Chapter 6 presents a superimposed training passive time-reversal (STpTR) approach to deal with the passive time-reversal (pTR) environmental mismatch between the probe and the message transmissions in a low SNR environment, using single and multiple receivers. Chapter 7 presents a study on the vector sensor multichannel combining for LPD communications and demonstrates the feasibility of employing STpTR and VS using data from a shallow water experiment. Chapter 8 summarizes the main results, presents the scientific contributions of this thesis, and discusses some directions for future research.

Chapter 2

Methodology

Abstract *This chapter presents the simulation scenario used for LPD communications and describes the methodology adopted in this thesis. Section 2.1 presents the simulation scenario in this thesis. The Monterey-Miami Parabolic Equation model used to simulate the acoustic propagation is described in Section 2.2. Section 2.3 presents the communication system model and the proposed superimposed training method. The fast Hadamard transform and the efficient crosscorrelation are detailed in Section 2.4. Section 2.5 describes the passive time-reversal technique. The Wiener filter equalizer is commented in Section 2.6. Section 2.7 explains the Hyperslice Cancellation by Coordinate Zeroing (HCC0) method to remove the probe interference.*

2.1 Scenario for communication system simulation

This section presents the scenario used for the simulations using the Monterey-Miami Parabolic Equation (MMPE) model aiming to develop the signal processing techniques for LPD communications presented in this thesis. Fig.2.1 shows the transmission loss estimated using MMPE model for the communication scenario derived from the test site of the Brazilian Navy "Institute of Sea Studies Admiral Paulo Moreira", located in Rio de Janeiro/Brazil. Most applications for LPD and low SNR communications rely on shallow water acoustic propagation. Shallow water is arbitrarily defined as the part over

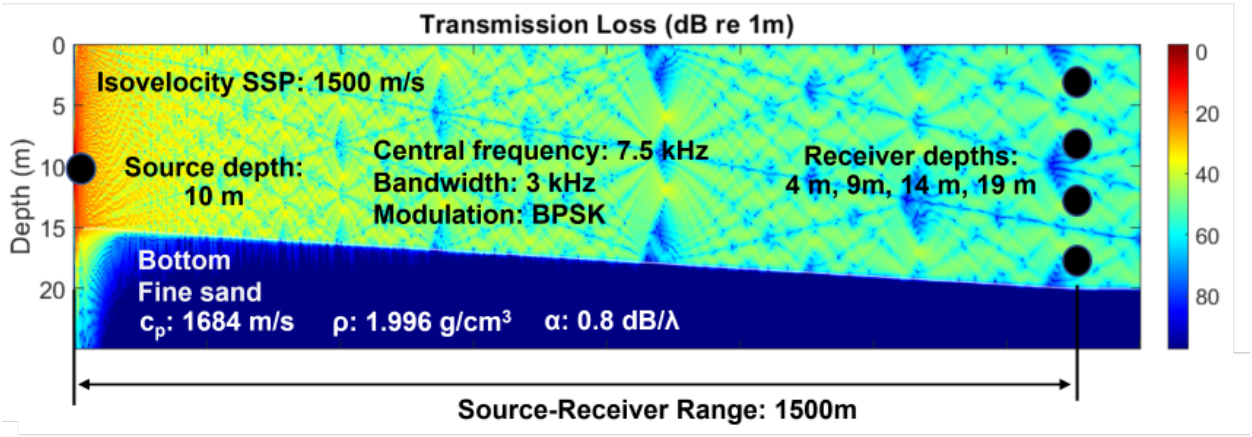

Figure 2.1: Transmission loss estimated using MMPE model for a simulation scenario defined by the channel physical parameters and the communication system setup parameters.

the continental shelf where depths are lower than 200m [2, 34]. In this work, "shallow water" means a water depth in which sound is propagated to the far-field a distance by repeated reflections from surface and bottom [2, 34]. However, the time-space varying shallow water waveguide is a complex medium to establish communications. The multipath propagation, induced by these surface/bottom reflections, causes intersymbol interference, degrading the system performance. The time-varying multipath structure depends on several factors such as the channel geometry, sound speed profile, source/receiver depths, range, frequency/bandwidth of the signals, and bottom composition amongst others.

To simulate the acoustic propagation in Fig.2.1, a source transmits broadband signals with a central frequency of 7.5 kHz, and bandwidth of 3 kHz, to a vertical linear array composed of 4 hydrophones positioned at a 1.5 km range. The source depth is 10m, and the hydrophones from the VLA are positioned at 4, 9, 14, and 19 m. The sound speed profile is isovelocity (1500 m/s).

In the model, the bottom layer is defined as a simple, homogeneous half-space with a smooth interface varying from 15 to 20 m. The bottom is classified as fine sand and the

estimated compressional speed (c_p) is 1684 m/s, according to [35]. The bottom density ρ=1.996 g/cm^3, and the compressional attenuation is $\alpha = 0.8$ dB/λ.

2.2 The Monterey-Miami Parabolic Equation model (MMPE)

In this work, the chosen acoustic propagation model is the Monterey-Miami Parabolic Equation model (MMPE) [36]. Despite several models that may compute solutions of the wave equation, just a few are both depth and range-dependent [37]. It is well-accepted that propagation models in shallow water need to have range dependent capabilities [38]. Shallow water is not only susceptible to water column temperature disturbances, but also to the sea surface variability during the acoustic propagation, and bottom properties in terms of bathymetry and sediment layers composition. The parabolic-equation methods, introduced into underwater acoustics by Hardin and Tappert in the 70s, provide numerical solutions to the Helmholtz equation based on Fast Fourier Transform. The MMPE is a broadband, full-wave acoustic propagation model and has been widely used by researchers in this field, to model the acoustic channel, especially in shallow waters due to its fast implementation and computational efficiency [39].

The standard parabolic wave equation is given by (2.1)

$$\frac{\partial^2\psi}{\partial r^2} + 2ik_0\frac{\partial\psi}{\partial r} + k_0^2(n^2-1)\psi = 0 \tag{2.1}$$

where $\psi(r,z)$ is the envelop function, and $n(r,z,\theta)$ is a function of depth (z), range (r), and grazing angle (θ). The MMPE model utilizes a split-step Fourier range-marching algorithm to solve the parabolic equation. A Gaussian field is used to generate the initial solution. Then, the marching algorithm maps the entire range-depth propagating field [38]. The

PE algorithm treats the sea surface as an ideal pressure release boundary, while the bottom boundary is treated as a fluid, with density smoothing functions to represent the discontinuity in sound speed and density. Based on the input parameters for the propagation scenario such as the source frequency and depth, frequency bandwidth, sound speed profiles, channel depth, and bathymetry, the MMPE computes the ocean impulse responses used to simulate the communication system.

2.3 Communication system model

Considering the ocean as a linear system, the transmission of a signal from a single source to a single or multiple M receivers may be modeled as an input signal $s(t)$ being convolved with the channel impulse response $h_m(t)$, added to the ambient noise component $n_m(t)$ (Fig. 2.2). The transmitted bitstream is composed of a probe code $x(k)$ superimposed to a signal of interest $d(k)$ transmitted at the same time, through the same channel and recorded at each m receiver, where k=1, 2, ..., L is a discrete time-index, $L = kT_s$ is the period of the probe sequence, and T_s is the period of each symbol. The probe $x(k)$ is a signal that must have good autocorrelation properties to estimate the channel impulse responses, used in both passive time-reversal and Wiener filter for signal equalization. The bitstream symbol sequence $A(k) = Px(k) + Qd(k)$, where P and Q are the probe and the data amplitudes, x(k)=$\pm$1 is the probe code, and d(k)=$\pm$1 is the data message. Due to the P and Q amplitudes, the resulting baseband bitstream $s(t)$ is amplitude and binary phase modulated given by $s(t) = \sum_{k=1}^{L} A(k)q(t - kT_s)$, where $q(t - kT_s)$ is the pulse shaping filter (rectangular, raised cosine...) centered at 0 with width T_s, to avoid intersymbol interference. The transmitted bandpass binary signal is given by $\tilde{s}(t) = Re[|s(t)|e^{(2\pi f_c t + x(t)\theta)}]$ where f_c is

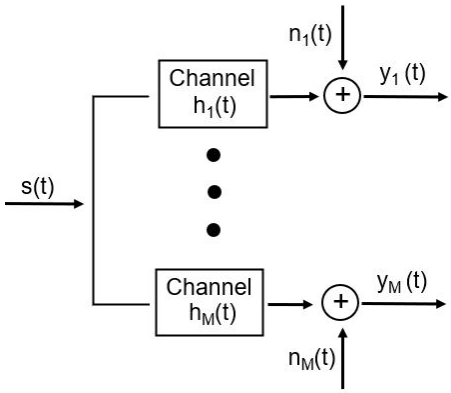

Figure 2.2: Communication system model with M channels, in baseband equivalent representation where $s(t)$ is the transmitted signal, $h_m(k)$ is the discrete CIR, $n_m(k)$ is the ambient noise, and $y_m(k)$ is the received signal in each m receiver.

the carrier frequency, $x(t)$ is the probe code in continuous time, and $\theta = \pi/2$ (BPSK).

The continuous time baseband received signal is given by (2.2)

$$y_m(t) = \sum_{k=1}^{L} h_m(\tau)s(t-\tau) + n_m(t) = s(t) * h_m(t) + n_m(t) \tag{2.2}$$

where $h_m(t)$ is the channel impulse response, and $n_m(t)$ is the ambient noise at the m receiver, and τ represents the channel multipath delay for a fixed value of t. Here and throughout this work, $*$ denotes convolution.

In this thesis, the discrete-time sampled probe $x(k)$ is equal to the value of the continuous-time probe $x(t)$ at times kT_s. Both M-sequence $x(k)$, in discrete time-domain, and $x(t)$ in continuous time-domain, may represent the probe signals transmitted through the acoustic channel for signal detection, and channel impulse response estimation. The conventional approach to cross correlate the received baseband bitstream $y_m(t)$ with the M-sequence probe $x(t)$, known to the receiver, is shown in (2.3)

$$h_m(t) = y_m(t) * x^{\dagger}(-t) \tag{2.3}$$

where † denotes complex conjugate. However, a direct M-sequence correlation can entail on

the order of L^2 operations, where $L = 2^N - 1$ is the period of the sequence and N is the degree of the feedback equation. Simplicity and efficiency of fast Walsh-Hadamard transform (FHT) to perform cyclic correlations of M-sequences have found several applications in underwater digital communications [15, 40] and sonar signal processing [41]. The correlation output can be well-approximated by a cyclic cross-correlation since the M-sequence has a good autocorrelation property. Therefore, the next section presents the similarities between the M-sequence and the Hadamard matrices and details the FHT to reduce the computational time.

2.4 Fast Hadamard Transform

The fast Walsh−Hadamard transform, also called Fast M-Sequence Transform [24], exploits the permutational equivalence between the M-sequence M_L and the Sylvester−Hadamard matrices H_{L+1} to perform cyclic cross-correlations. Thus, the matrix multiplication by the Walsh−Hadamard matrix (2.6) may proceed via a butterfly algorithm similar to the fast Fourier transform (FFT) [42]. Replacing multiplications of direct correlation by addition and subtraction operations only, the correlation number of operations is drastically reduced from L^2 to $Llog_2L$ saving computational time.

2.4.1 The M-sequence matrix

Maximal length sequence, known as M-sequence, is a binary sequence generated by a linear feedback shift register whose characteristic polynomial is primitive given by (2.4)

$$f(x) = x^N + \sum_{i=0}^{N-1} c_i x_i \tag{2.4}$$

The resulting M-sequence $[x_k] = [c_1, ...c_{2^N-1}]$ can be shown to have an impulse-like

autocorrelation function, and for this reason, are often called pseudorandom sequence. The cyclic permutations of the code may generate an orthogonal square M-sequence matrix M_L of order $L = 2^N - 1$. The first row of M_L is $[x_k]$ and the successive rows are cyclic shifts of $[x_k]$. For a given value of N, there exist several M-sequences but those created from a large N present better correlation properties. Let us consider, for example, the M-sequence code $[x_k] = [1, 1, 1, 0, 0, 1, 0]$, created from the recursive equation $f(x) = x^3 + x + 1$. Replacing the 1's for -1's, and 0's for 1's in the M-sequence code $[x_k] = [-1, -1, -1, 1, 1, -1, 1]$, the corresponding M-sequence matrix or order $2^N - 1$, where N=3, is given by (2.5)

$$M_{2^N-1} = \begin{bmatrix} c_1 & c_2 & c_3 & c_4 & c_5 & c_6 & c_7 \\ c_2 & c_3 & c_4 & c_5 & c_6 & c_7 & c_1 \\ c_3 & c_4 & c_5 & c_6 & c_7 & c_1 & c_2 \\ c_4 & c_5 & c_6 & c_7 & c_1 & c_2 & c_3 \\ c_5 & c_6 & c_7 & c_1 & c_2 & c_3 & c_4 \\ c_6 & c_7 & c_1 & c_2 & c_3 & c_4 & c_5 \\ c_7 & c_1 & c_2 & c_3 & c_4 & c_5 & c_6 \end{bmatrix} = \begin{bmatrix} -1 & -1 & -1 & +1 & +1 & -1 & +1 \\ -1 & -1 & +1 & +1 & -1 & +1 & -1 \\ -1 & +1 & +1 & -1 & +1 & -1 & -1 \\ +1 & +1 & -1 & +1 & -1 & -1 & -1 \\ +1 & -1 & +1 & -1 & -1 & -1 & +1 \\ -1 & +1 & -1 & -1 & -1 & +1 & +1 \\ +1 & -1 & -1 & -1 & +1 & +1 & -1 \end{bmatrix} \tag{2.5}$$

2.4.2 The Hadamard matrix

A Sylvester-Hadamard matrix H_{2^N} (2.6) is defined as a square matrix of order N where all entries are ± 1 and its row vectors define a complete set of orthogonal functions so that $H_N H_N^T = N I_N$, where H^T is the transpose of H_N, and I_N is the identity matrix. The Hadamard matrix exists only for a power of 2 and may be computed recursively as

$$H_{2^N} = \begin{bmatrix} H_{2^{N-1}} & H_{2^{N-1}} \\ H_{2^{N-1}} & -H_{2^{N-1}} \end{bmatrix}, \text{ for N=1,2,3... where } H_1 = [1]. \tag{2.6}$$

Thus, for N=3

$$H^8 = \begin{bmatrix} +1 & +1 & +1 & +1 & +1 & +1 & +1 & +1 \\ +1 & -1 & +1 & -1 & +1 & -1 & +1 & -1 \\ +1 & +1 & -1 & -1 & +1 & +1 & -1 & -1 \\ +1 & -1 & -1 & +1 & +1 & -1 & -1 & +1 \\ +1 & +1 & +1 & +1 & -1 & -1 & -1 & -1 \\ +1 & -1 & +1 & -1 & -1 & +1 & -1 & +1 \\ +1 & +1 & -1 & -1 & -1 & -1 & +1 & +1 \\ +1 & -1 & -1 & +1 & -1 & +1 & +1 & -1 \end{bmatrix} \tag{2.7}$$

2.4.3 Efficient cyclic correlation using FHT

The computation algorithm of the FHT to perform the cyclic correlation of M-sequences is briefly described in this section. There is a permutational equivalence between M-sequence and Hadamard matrices. The M-sequence matrix (2.5) may be decomposed as a linear modulo-2 combinations of the first N rows/columns of M as (2.8):

$$M_L = G_{L\times N} V_{N\times L} = \begin{bmatrix} -1 & +1 & +1 \\ +1 & -1 & +1 \\ +1 & +1 & -1 \\ -1 & -1 & +1 \\ +1 & -1 & -1 \\ -1 & -1 & -1 \\ -1 & +1 & -1 \end{bmatrix} . \begin{bmatrix} -1 & -1 & -1 & +1 & +1 & -1 & +1 \\ -1 & -1 & +1 & +1 & -1 & +1 & -1 \\ -1 & +1 & +1 & -1 & +1 & -1 & -1 \end{bmatrix} \tag{2.8}$$

where G consists of the first N rows of M, and Q consists of columns in M which first N rows form an identity matrix, remembering that 0's are replaced by 1's and 1's by -1's.

On the other hand, the Hadamard matrix (2.6) may be factored as (2.9):

$$H_{L+1} = B_{L+1\times N} B^T_{N\times L+1} = \begin{bmatrix} +1 & +1 & +1 \\ +1 & +1 & -1 \\ +1 & -1 & +1 \\ +1 & -1 & -1 \\ -1 & +1 & +1 \\ -1 & +1 & -1 \\ -1 & -1 & +1 \\ -1 & -1 & -1 \end{bmatrix} . \begin{bmatrix} +1 & +1 & +1 & +1 & -1 & -1 & -1 & -1 \\ +1 & +1 & -1 & -1 & +1 & +1 & -1 & -1 \\ +1 & -1 & +1 & -1 & +1 & -1 & +1 & -1 \end{bmatrix} \tag{2.9}$$

.

The permutational equivalence between the M-sequence and the Hadamard matrices, may be observed bordering the matrix G on top with a row of all 1's, and the matrix V on the left with a column of all 1's. The resulting $\hat{G}$ and B differ by a a row permutation, while $\hat{V}$ and B^T differ by a column permutation. The $\hat{G} = P_G B$ and $\hat{V} = B^T P_V$, where P_G and P_V are $L+1 \times L+1$ permutation matrices.

Therefore, instead of performing the direct crosscorrelation between the M-sequence matrix and the received signal vector y_L (2.3), the channel impulse response may be estimated much faster taking advantage of the permutational equivalence between the M-sequence and the Hadamard matrices (2.10), reducing the number of operations from L^2 to $Llog_2L$.

$$M_L = Z_R P_G B B^T P_V Z_I = Z_R P_G H_{L+1} P_V Z_I \tag{2.10}$$

where $[Z_I]_{(L+1\times L)} = \begin{bmatrix} 1 \\ I_L \end{bmatrix}$ is used to increase the size of the received signal y_L from L to L+1, I_L is the identity matrix of dimension L, P_V and P_G are $(L+1 \times L+1)$ permutation matrices, and $[Z_R]_{(L\times L+1)} = \begin{bmatrix} 1 & I_L \end{bmatrix}$ is a matrix to reduce the size of the channel impulse response vector from L+1 to L.

The correlation steps using the fast Hadamard transform (2.10) are described as follows: i) increasing the size of the received bitstream y_L to L+1 using $[Z_I]_{(L+1\times L)}$ and reordering the data according to P_V; ii) multiplication by the Walsh-Hadamard matrix via a butterfly algorithm similar to the FFT [42]; iii) reordering the transformed data according to P_G and reducing the size from L+1 to L. The interested reader is referred to [24, 42, 43] for further details.

2.5 Passive time-reversal

The passive time-reversal (pTR) is a low complexity channel equalizer that applies matched filtering at each receiver element (Fig. 2.3). The usual approach for pTR communications sends the probe before the data, to estimate the channel. However, in this thesis, a new approach for pTR is presented in chapter 6: the superimposed training pTR.

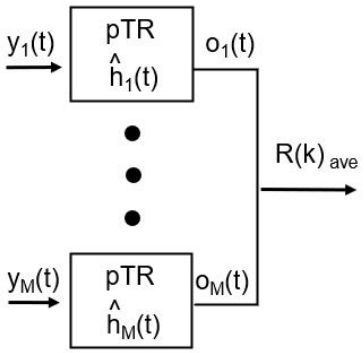

Figure 2.3: Diagram of the passive time-reversal receiver with M channels. The signals $y_m(t)$, from each m channel, are passed through the pTR where the estimated CIR $\widehat{h}_m(t)$ are time reversed, time-gated, and convolved to $y_m(t)$. The summation of the pTR outputs $o_m(t)$ yield the final pTR output signal $R(k)$.

The pTR convolves the received $y_m(t)$ with their own time-reversed CIR $\widehat{h}^{\dagger}_m(-t)$, where † denotes complex conjugate (2.11).

$$o_m(t) = y_m(t) * \widehat{h}^{\dagger}_m(-t) = s(t) * \left[h_m(t) * \widehat{h}^{\dagger}_m(-t) \right] \tag{2.11}$$

.

The outputs $o_m(t)$ of all M channels are combined coherently as given by (2.12)

$$R(k) = \sum_{m=1}^{M} o_m(t) = s(t) * \left[\sum_{m=1}^{M} h_m(t) * \widehat{h}^{\dagger}_m(-t) \right] \tag{2.12}$$

where the term in brackets represents the Q-function [27, 44].

The Q-function represents the cross-correlation between the estimated and the actual CIR summed over the channels, and determines the equalizer performance as a function of the number of receivers [29]. Fig. 2.4 (left) shows the channel impulse responses for the 4 channels of the canonical scenario shown in Sec. 2.1 at depths of 4, 9, 14, and 19m. One can observe in fig. 2.4 (middle) that the performance of time-reversal focusing depends on the complexity of the channel impulse responses $h_m(t)$, the number of multipath, the number of array elements M, and their spatial distribution.

An impulse-like shape of the Q-function means a successful compensation of the multipath distortions with the focusing of the pulse energy. Fig. 2.4 (right) shows that as the number of receivers increase, the main lobes add up in phase while the out-of-phase sidelobes are canceled out. The spatial diversity serves to reduce the intersymbol interference, minimizing the sidelobe levels of the Q-function, and to reduce the variance of the symbol phase fluctuation. One can also observe in fig. 2.4 (right) that the Q-function has many sidelobes. The highest sidelobe reach a level of 0.2 of the main lobe level, and are separated from the main lobe by several symbols (in time). The peak to the sidelobe (PSL) ratio indicates the

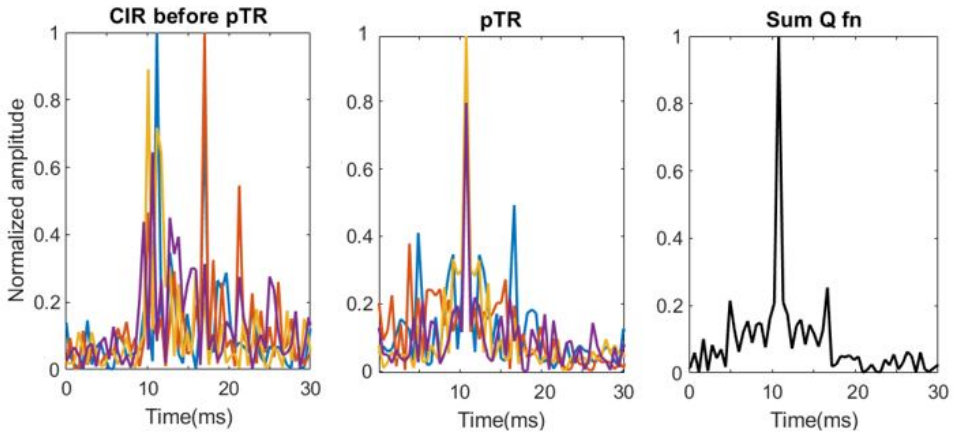

Figure 2.4: Channel impulse responses, passive time-reversal (pTR), and the Q-function for simulated received signals from the 4 channels of the canonical scenario at depths 4, 9, 14 and 19m.

pTR performance [44]. The higher the PSL, the lower the ISI. However, there is always a residual ISI, which requires equalization to be eliminated [18, 29].

2.6 Wiener filter theory

The Wiener filter [45–48] is an optimal linear equalizer based on the mean squared error (MSE), the most frequently used optimization criterion in filtering applications. Suitable for linear time-invariant (LTI) systems, the Wiener filter (Fig. 2.5) plays a role in a wide range of applications such as noise reduction, channel equalization and signal estimation [47, 48].

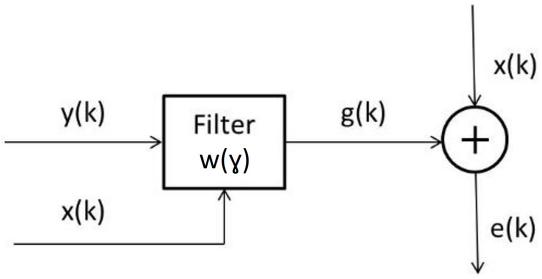

Figure 2.5: Diagram of the Wiener filter for linear MMSE estimation.

In discrete-time domain, the filter coefficients $w(\gamma)$ are calculated to provide the minimum MSE (MMSE) between the filter output $g(k)$ and the probe $x(k)$, where k=1, 2, ..., L is a discrete time-index, $L = kT_s$ is the period of the probe sequence, and T_s is the period of each symbol.

Thus, the estimated error signal $e(k)$ is given by (2.13)

$$\begin{aligned} e(k) &= x(k) - g(k) \\ &= x(k) - \sum_{\gamma=0}^{\Gamma-1} w(\gamma) y(k-\gamma) \end{aligned} \tag{2.13}$$

where Γ is the order of the filter, and $y(k)$ is the received bitstream.

Assuming that the input signal $y(k)$ and the training sequence $x(k)$ are both zero-mean stationary random processes, the MSE $\xi(k)$ can be written as (2.14)

$$\begin{aligned}\xi(k) &= E[e^2(k)] \\ &= E[(x(k) - \mathbf{w^T y})^2] \\ &= \sigma_x^2 - 2\mathbf{w^T r_{xy}} + \mathbf{w^T R_{yy} w}\end{aligned} \tag{2.14}$$

where $E[.]$ is the expectation operator, $\mathbf{w^T}$ is a transpose of the $\Gamma \times 1$ vector of the Wiener filter coefficients, $\mathbf{y}$ is the $\Gamma \times 1$ vector of the received signal, σ_x^2 is the variance of $x(k)$, $\mathbf{R_{yy}}$ is an $\Gamma \times \Gamma$ Hermitian Toeplitz matrix of autocorrelation of the input signal, and $\mathbf{r_{xy}}$ is the cross-correlation vector of the input and training signals.

In (2.14), if the matrix $\mathbf{R_{yy}}$ is invertible, the solution for the optimum Wiener filter tap weights, known as the Wiener-Hopf equation, is given by (2.15)

$$\mathbf{w} = \mathbf{R_{yy}^{-1} r_{xy}} \tag{2.15}$$

In this thesis, as Wiener is used for channel equalization, the number of filter taps Γ is selected to span the duration of the expected multipath to mitigate the ISI. The value of Γ determines the relative location of the reference peak, typically about $\Gamma/2$. However, depending on the chosen Γ, the matrix inversion may be computationally intensive. Thus, as the duration of the pre and post-symbol ISI is not equal, Γ must be selected proportionately to encompass only the most significant ISI samples.

2.7 Interference removal using HCC0

To remove the intentional probe interference to the data, a method called "hyperslice cancellation by coordinate zeroing (HCC0)" [43] is employed. Basically, HCC0 states that zeroing

the strong arrivals after pulse compression, in a "arrival space", and inverse Hadamard transforming, the interference can be removed and the weak data retrieved.

Starting from the crosscorrelation in (2.3), in matrix form, and expanding the terms defined in Sec. 2.3:

$$\begin{aligned} h'_L &= M_L y_L \\ &= M_L[Px(k) + Qd(k)] * h_L + n(k) \\ &= M_L[Px(k) * h_L] + M_L[Qd(k) * h_L] + n(k) \\ &= [P\rho_{xx} * h_L + Q\rho_{dx} * h_L] + n(k) \end{aligned} \tag{2.16}$$

where $\rho_{xx} = [M_L x(k)]$ is the M-sequence probe code auto-correlation function and $\rho_{dx} = [M_L d(k)]$ is the crosscorrelation between the message and the probe.

The ρ_{xx} estimates the CIR, while ρ_{dx}, despite an intentional interference, is treated as additive noise. After channel equalization, the multipath expressed by both ρ_{xx} and ρ_{dx} is reduced. Thus, the HCC0 is performed. The equalized ρ_{xx} is removed by zeroing out the samples having amplitude higher than a threshold η (2.17), defined by trial and error.

$$h''_L = \begin{cases} 0, & \text{if } |h'_L| > \eta \\ h'_L, & \text{elsewhere} \end{cases} for L = 0, .., kT_s. \tag{2.17}$$

After HCC0, an inverse FHT is applied over the remaining sequence h''_L to decompress the message.

$$\widehat{y}_L = M_L^{-1} h''_L = M_L^{-1}[Q\rho_{dx} * h''_L] + n(k) = Qd(k) * h''_L + n(k) \tag{2.18}$$

The IFHT (2.18) is efficiently performed, in a similar manner to the FHT in (2.10). As

the inverses of P_G and P_V are their transpose, IFHT may use the same mapping matrices as follows

$$M_L^{-1} = Z_I^T P_G^T (H_{L+1})^{-1} P_V^T Z_R^T \tag{2.19}$$

Using the butterfly algorithm, similar to the IFFT, the IFHT avoids the calculation of the inverse of a large matrix of size L. The resulting signal, $\widehat{y}_L$ contains the message, the residual intersymbol interference and the ambient noise.

2.8 Signal-to-Noise ratio (SNR) estimation

The present section details the signal-to-noise ratio (SNR) estimation method, used throughout this thesis. Data from three different shallow water experiments, in the frequency band from 6 to 9 kHz, were contaminated with ambient noise which arise from a variety of different mechanisms [49, 50]. The power spectrum density of broadband ambient noise is frequency dependent. Man-made noise is mainly due to distant shipping, oil-drilling operations and other industrial activities in the vicinities of the city's harbor, close to the experimental sites, extending from 1 Hz to 200 kHz . Nearby shipping and seismic air-guns may also contribute into the 1 kHz to 10 kHz band [49].

Natural sources of noise include wind, rain, and wave-breaking in the band 1 Hz to 100 kHz [50]. Biological organisms are also an important source of noise. The temporal character of noise is as varied as its frequency content. Clicks and impulsive noise in the experimental sites over the continental shelves generally comes from marine animals such as whales, porpoises, and snapping shrimp. Snapping shrimp noise is significant from a few kHz to above 100 kHz, close to reefs and in rocky bottom regions in warm shallow waters [50]. Furthermore, mammals vocalizations may share the same frequency band from a few Hz to

several kHz. Thus, depending on the communication system frequency band, the ambient noise may severely degrade its performance.

2.8.1 Experiments off the Cabo Frio Island (Brazil)

In the two experiments performed off the Cabo Frio Island (Brazil), described in Chapters 3 and 4, low power signals were transmitted. The received signals were severely contaminated with impulsive background noise [51]. Both experiments were performed close to the rocky shores, in a region of heavy recreational vessels traffic and wave breaking on the nearby beach.

Fig. 2.6 shows a sample of the background noise in the frequency band from 1 to 15 kHz, recorded during the first communication experiment. To minimize the noise impact over communications, the input bitstreams were band-pass filtered (6-9 kHz), baseband converted and Doppler corrected. Then, the filtered bitstreams were used to provide an in-band input SNR estimation. In these experiments, there was no extra addition of noise to the data.

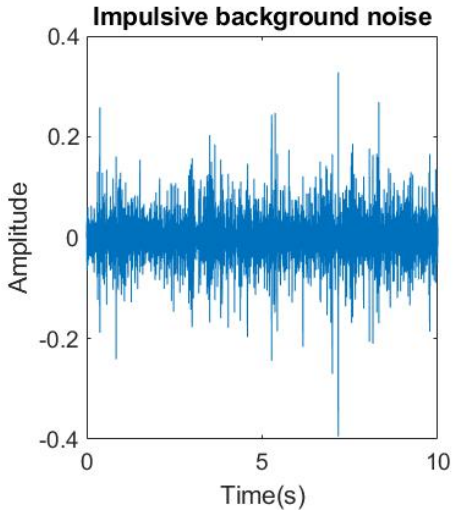

Figure 2.6: A sample of the impulsive background noise in the frequency band from 1 to 15 kHz, recorded during the first communication experiment performed off the Cabo Frio Island.

Proposed methods in this work explore temporal diversity of Z consecutive signals, for single-channel systems. Thus, the average in-band input SNR (dB) for each channel m was estimated according to (2.20)

$$SNR_m = 10log_{10}\left[(S_m - N_m)/N_m\right], \tag{2.20}$$

where S is the mean of the signal plus noise power of Z sequences, and N is the mean of the noise power of a sequence of the same length as S, estimated from a noise-only period. The noise-only period may be measured before or after transmissions, depending on the experiment.

The methods also explore spatial diversity for multichannel combining. Thus, the average in-band input SNR of the array was estimated as (2.21)

$$SNR_{array} = 10log_{10}\left[\frac{1}{M}\sum_{m=1}^{M}\left[(S_m - N_m)/N_m\right]\right], \tag{2.21}$$

where M is the number of channels.

2.8.2 Experiment EMSO'21 (Portugal)

In the experiment performed off the coast of Algarve/Portugal, described in Chapter 7, high power signals were transmitted. The received signals were recorded at high SNR. The ambient noise may be approximated by a Gaussian distribution if one considers the linear superposition of many independent noise sources [49]. Several papers related to LPD communications add additive white Gaussian noise (AWGN) to reduce the SNR at the receiver [16, 20, 22]. However, in this experiment, ambient impulsive noise recorded by each channel, at the beginning of the experiment before transmissions, was added to the data files

to reduce the in-band input SNR. After the noise addition, the resulting bitstreams $y_z(t+z\tau)$ were band-pass filtered (6-9 kHz), baseband converted and Doppler corrected. Then, the in-band input SNR (dB) for each channel m was estimated, in time-domain, according to (2.20), where S is the mean power of Z received bitstreams plus added noise, N is the mean power of the combined noise of a period of the same length of S, estimated after each transmission. Similarly, for multichannel combining, the in-band input SNR of the array was estimated using (2.21), where M is the number of channels of the vector sensor.

Chapter 3

Superimposed training low probability of detection underwater communications

Abstract *This chapter presents a superimposed training method for low probability of detection underwater acoustic communications. The approach has been developed using the Monterey-Miami Parabolic equation model to simulate the acoustic channel and tested in a shallow water experiment on the coast of Rio de Janeiro/Brazil. Section 3.1 presents the superimposed training LPD communications. Section 3.2 introduces the superimposed training bitstream. The communication system is detailed in Section 3.3. In Section 3.4 the shallow water experiment is described. Results are shown in Section 3.5. A brief discussion concludes the chapter in Section 3.6*

3.1 Superimposed training LPD communications

This chapter presents a superimposed training method for underwater acoustic communications in a low SNR environment and demonstrates its feasibility for LPD communications based on both modeling and a shallow water experiment. Superimposed training techniques present several benefits. First, no additional time slot is needed for the pilot or extra bandwidth consumption to estimate the channel impulse response (CIR). Second, there is no loss in the data rate and no data frequency spreading [52]. Computationally simple, the

proposed algorithm was developed to work with a fixed single low power source and a receiver, without an array gain. Before transmission, a bitstream is created superimposing a long training sequence to the message. Using a low power source, the bitstream is transmitted and repeated several times to permit the receiver to increase the processing gain and to implement error correction through coherent averaging. A Wiener filter [53] performs equalization. A fast Hadamard transform (FHT) [15, 24, 43] estimates the CIR and compresses the pilot energy. After synchronization and average of the filtered bitstreams, the intentional probe interference is removed using the Hyperslice Cancellation by Coordinate Zeroing (HCC0) process [15, 41, 43]. An inverse FHT over the remaining sequence decompresses the data energy, and the message is retrieved. The superimposed training approach has been proposed and tested using the Monterey-Miami Parabolic Equation (MMPE) model for communications in the canonical scenario shown in Chapter 2. To prove the concept, a shallow water experiment was performed in the bay of Arraial do Cabo on the coast of Rio de Janeiro/Brazil. Achieved bit error rates (BER) show that the approach is consistent. Compared to LPD benchmark [23] (SNR< -8 dB), the results indicated the method's suitability for covert communications.

3.2 Superimposed training bitstream

The superimposed training (ST) concept involves summing a long probe to the message, both sequences of length $L = 2047$, before transmission. Fig. 3.1(left) shows the summation, in baseband, of bit-signals using the same symbol rate. The probe is a binary phase-coded maximum length sequence, known as M-sequence (Mseq2047) [24]. M-sequences are a family of signals commonly used to estimate the impulse response

of the ocean waveguide. Pseudorandom and deterministic, M-sequences have useful properties for covert communications such as a noise-like spectrum and an impulse-like autocorrelation [15, 24]. Furthermore, as codes are orthogonal, multiple users may access the channel with a low degree of interference [15]. The message is composed of three zero-padded bits followed by four consecutive streams of 511 bits. Delimited by a short M-sequence of 31 bits (Mseq31), each 480-bit data packet is composed of the following pangram: **(The_Quick_Brown_Fox_Jumps_Over_the_Lazy_Dog_0123456789!@#$)**.

The probe and the message have different amplitudes and phases. In contrast to other superimposed training algorithms [52], the power of the pilot is slightly higher than the power of the message. In a low SNR environment, a stronger pilot can disguise the message in the background noise and yield a high pulse compression gain for channel estimation, synchronization, and equalization [16]. As explained in Sec. 2.3, the amplitude ratio between the message (Q) and the probe (P) is 4/5. Next, the baseband bitstream modulates the

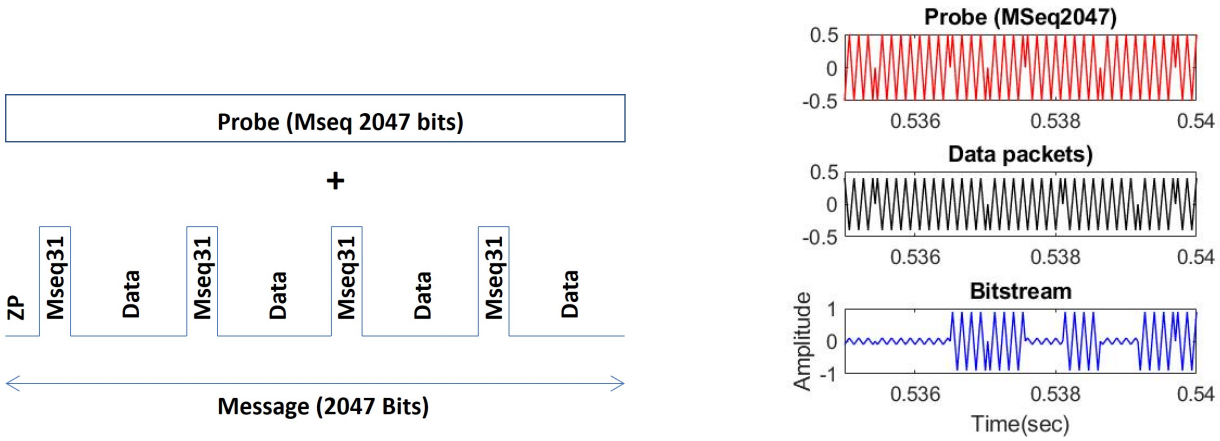

Figure 3.1: Left) Superimposed training bitstream is created by summing the probe (Mseq2047) and the message. The message has three zero-padded bits (ZP) and four data packets of the same content (480 bits), preceded by a short Mseq31 for hard synchronization. Right) The probe, the data packets and the resulting amplitude and phase modulated bitstream in BPSK waveform.

carrier wave as shown in Fig. 3.1(right). The resulting bitstream is given by

$$\tilde{s}(t) = Re[|s(t)|e^{(2\pi f_c t + x(t)\theta)}] \tag{3.1}$$

where $s(t) = \sum_{k=1}^{L} A(k)q(t - kT_s)$, $q(t)$ is the rectangular pulse shape, f_c is the carrier frequency, $x(t)$ is the Mseq2047 probe code values (± 1), and $\theta = \pi/2$ (BPSK). Each bit modulates 4 cycles of the carrier wave. The central frequency f_c is 7.5 kHz and the bandwidth is 3 kHz. Dealing with low power signals, the chosen sampling frequency f_s was four times f_c, higher than the Nyquist sampling rate. Despite the additional computational effort, the oversampling may not only avoid aliasing but also reduce the signal distortion, improve the signal resolution, and increase the signal to noise ratio.

Fig. 3.2 shows the power spectrum densities of the resulting bitstream (blue), the probe (red), and the message (black). According to the chosen amplitude relation (4/5), the message to probe ratio is -1.94 dB. As one can observe in Fig. 3.2, the message is embedded in the training sequence. Therefore, the bitstream presents LPI/LPD properties.

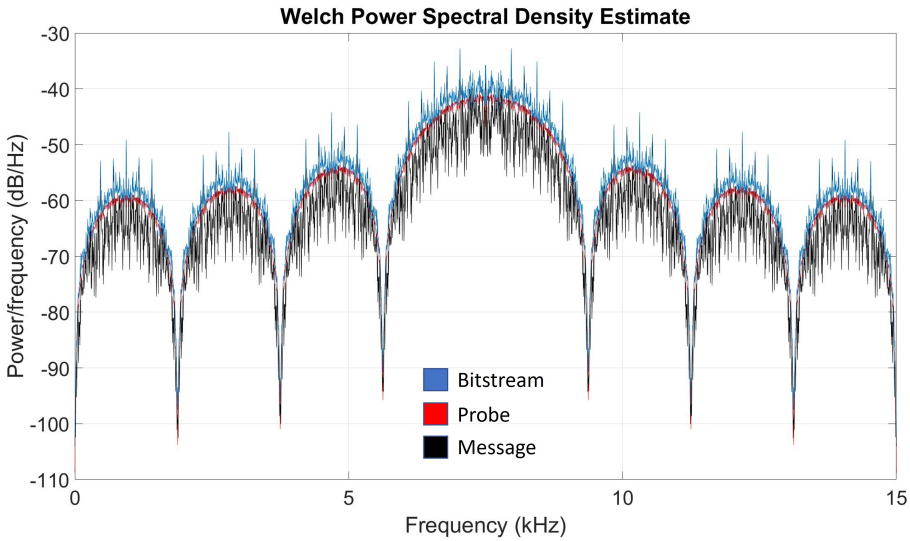

Figure 3.2: Power spectrum densities of the bitstream (blue), the probe (red), and the message (black), for a message to probe amplitude ratio of 4/5.

3.3 The LPD communication system

The LPD communication system is divided according to the block diagram in Fig. 3.3.

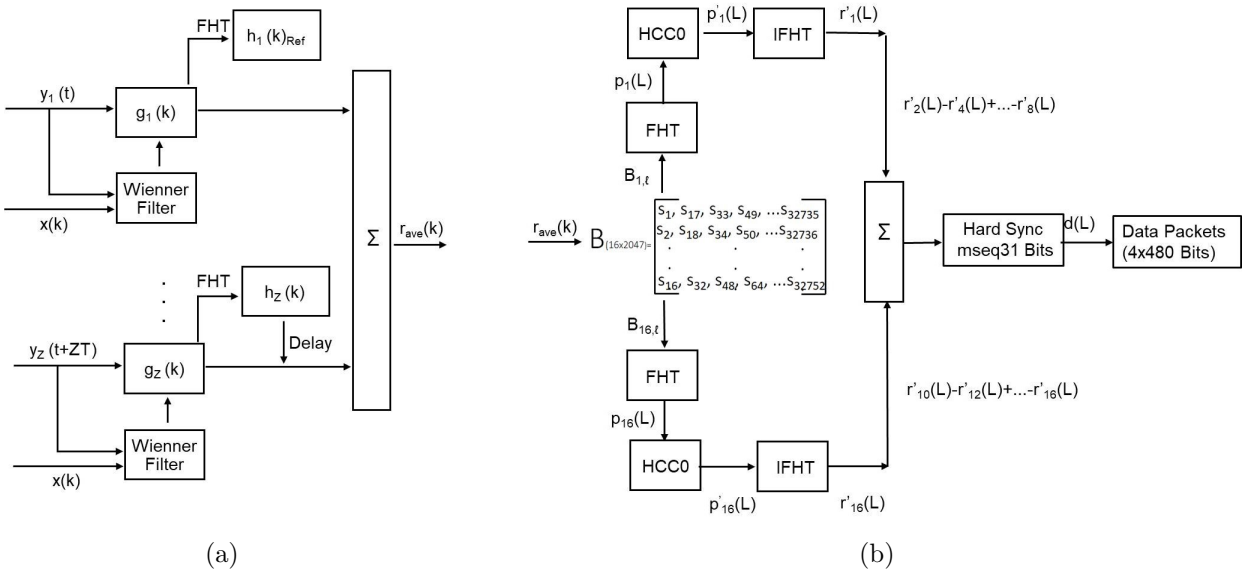

(a) (b)

Figure 3.3: a) Diagram of channel equalization, soft synchronization and coherent averaging of Z low SNR signals; b) Diagram of FHT $r_{ave}(k)$, interference removal (HCC0), inverse FHT, summation, hard synchronization and message retrieval.

3.3.1 Channel equalization and soft synchronization

The same bitstream $s(t + ZT)$ of period T is transmitted and repeated Z times to increase the processing gain and to perform error correction through coherent averaging. A Wiener filter [53] is applied over each received sequence $y_Z(t + ZT)$ to mitigate multipath and reduce intersymbol interference. Using a replica of the known pilot code $x(k)$, where k is the discrete time index, the filter performs the channel equalization, estimating $g_Z(k)$. The soft synchronization of the filtered bitstreams $g_Z(k)$ involves several CIR $h_Z(k)$ estimations. Thus, an efficient FHT, also called Fast M-Sequence Transform [24], is used to estimate $h_Z(k)$ from $g_Z(k)$. The reference for synchronization is the dominant peak of the first $h_{1_{ref}}(k)$. Time delays for later sequences are estimated using respective $h_Z(k)$ so that their strongest peaks

are coincident with the reference. After alignment, coherent averaging of Z low power signals $g_Z(k)$ plus noise provides a higher SNR bitstream $r_{ave}(k)$ (Fig. 3.3a).

3.3.2 Interference cancellation using HCC0

To let the reader understand the HCC0, the averaged bitstream $r_{ave}(k)$ is decomposed to form $B_{(16X2047)}$ (Fig. 3.3b). Fig. 3.4 shows that synchronous sampling $r_{ave}(k)$, the first row of B is filled by the first sample (s_1) of each bit. The second row starts with the second sample (s_2), and so on. The rearrangement in matrix B shows that odd rows have samples close to zero and even rows express the M-sequence probe amplitude fluctuation, phase reversed in 180°, where $B(2,l) \simeq -B(4,l) \simeq B(6,l) \simeq ... \simeq -B(16,l)$ for $l = 1...L$. This decomposition allows an easy implementation of the forward and inverse fast Hadamard transform of each row, used for channel estimation, and HCC0.

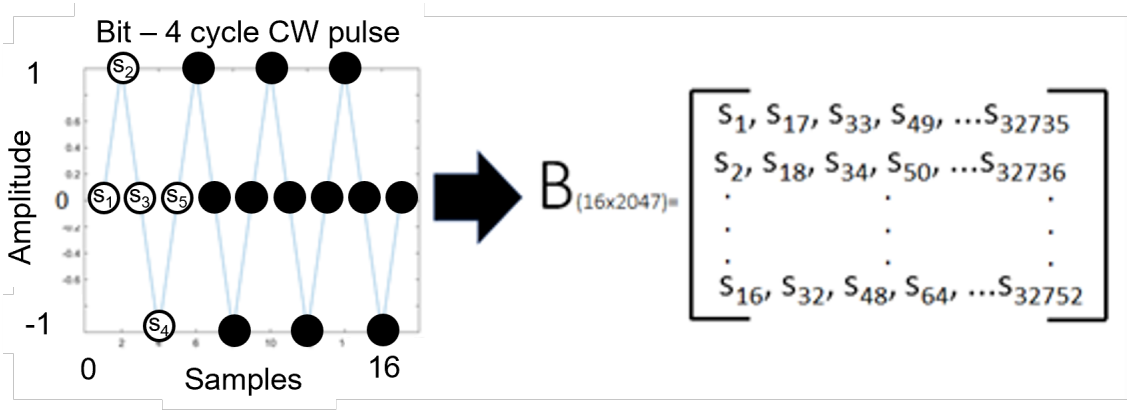

Figure 3.4: Left) One bit modulates 4 cycles of the carrier wave, sampled four times f_c. Right) Matrix $B_{(16X2047)}$ is formed by synchronous sampling the bitstream.

3.3.2.1 HCC0 using simulations and analysis about covertness

To understand the HCC0 method and verify its suitability to remove the probe interference, a transmission through the noiseless channel, described in Chapter 2, has been simulated using the Monterey-Miami Parabolic Equation (MMPE) model.

Fig. 3.5 shows the convolution of the ST bitstream with the CIR $h'(t)$ from MMPE estimated for the hydrophone at the depth of 19 m (Sec. 2.1), to simulate a received signal $y(t)$.

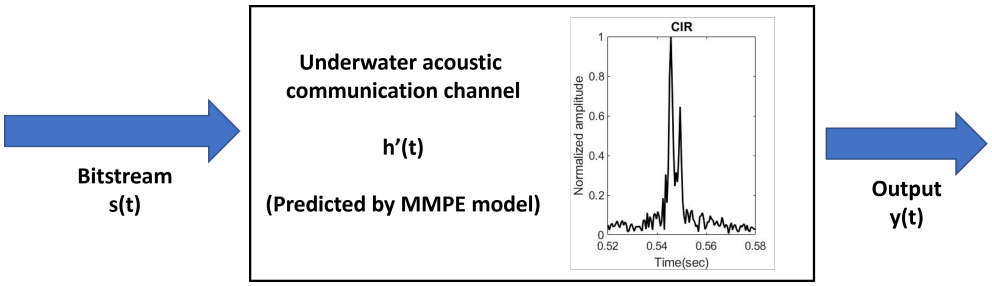

Figure 3.5: Simulation using the CIR $h'(t)$ estimated using the Monterey-Miami Parabolic Equation model. The simulated received bitstream $y(t)$ is created convolving the transmitted bitstream $s(t)$ in waveform with the CIR $h'(t)$.

The $y(t)$ was Wiener filtered using a number of taps adjusted to minimize the mean square error between $y(t)$ and the probe code $x(t)$. The length of the Wiener filter can not be too long to reduce the computational complexity of the filter and avoid the inclusion of excessive noise in the filtering process. In practice, the filter length must be long enough to compensate for most strong multipath arrivals.

The typical assumption in the literature about LPD communications is that an eavesdropper does not have the transmitted probe code used for matched fiter detection. However, to analyze the HCC0 and to observe the superimposed training approach covertness, let us assume that an eavesdropper has the two codes used for the hard (MSeq2047) and soft (MSeq31) synchronizations. Fig. 3.6 (left, upper plot) shows that the probe is clearly visible after the FHT of $y(t)$. As the probe is interfering with the message, the MSeq31 correlation peaks can not be detected. However, if a legitimate receiver performs the coordinate zeroing (HCC0) of the FHT samples above an arbitrary threshold η, the MSeq2047 is removed and the MS31 correlation peaks become visible, as shown by the red dots in Fig. 3.6 (right,

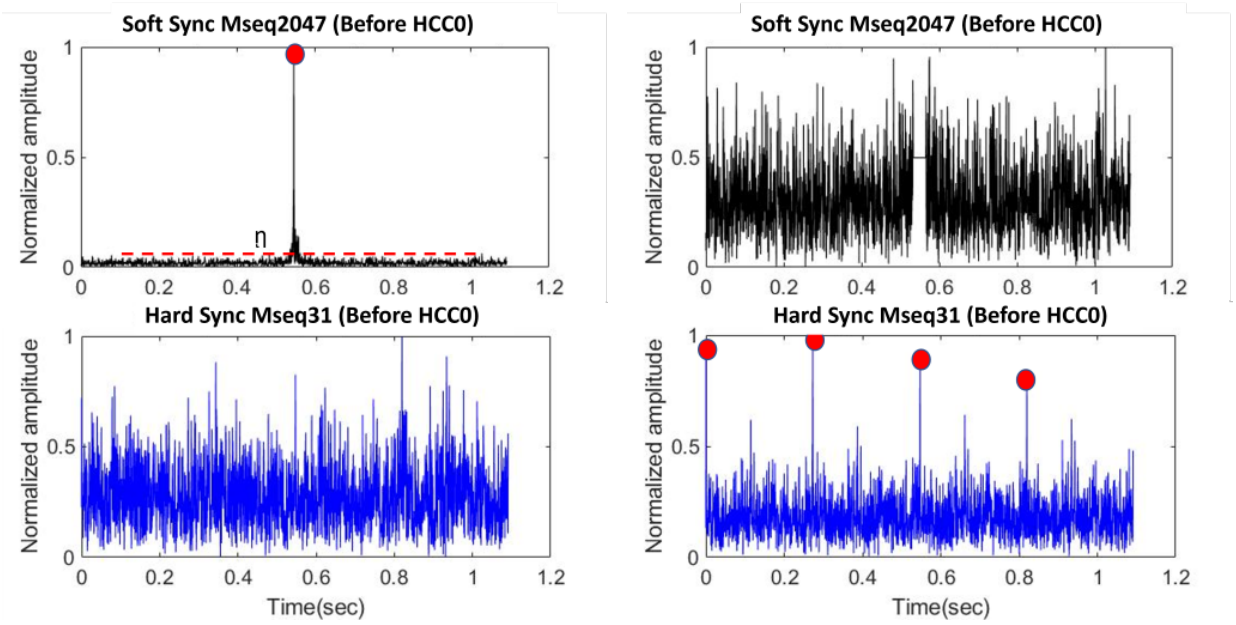

Figure 3.6: Soft and hard synchronization using simulated data from MMPE model. Left) In the upper plot, the MSeq2047 crosscorrelation peak is clearly visible. In the lower plot, the peaks from the MSeq31 correlation are not visible due to the interference. Right) In the upper plot, after the HCC0, the peak of the probe is not visible, confirming the probe removal. The lower plot shows the soft synchronization peaks (red dots).

lower plot). Therefore, the receiver may proceed with the signal processing, as the probe interference has been removed.

3.3.2.2 HCC0 using experimental results

In practice, the coordinate zeroing threshold η is adjusted by trial and error to eliminate most strong arrivals. But a real-time system may define η based on the power of the time-varying crosscorrelation peak above the average background noise. A FHT is used for $r_{ave}(k)$ pulse compression. Fig. 3.7 a) shows the CIR and the multipath spread. As detailed in Sec. 3.3.2, $r_{ave}(k)$ is rearranged to form matrix $\mathrm{B}_{(16XL)}$, where one can observe that the pilot energy of each baseband sequence $p_i(L)$ is restricted to just a few samples after pulse compression (Fig. 3.7b), where $i = 1...16$. A simple cancellation of the pilot interference to the message is performed by HCC0 [15,41,43] which zeroes out samples $q_i(l)$ having amplitudes higher than

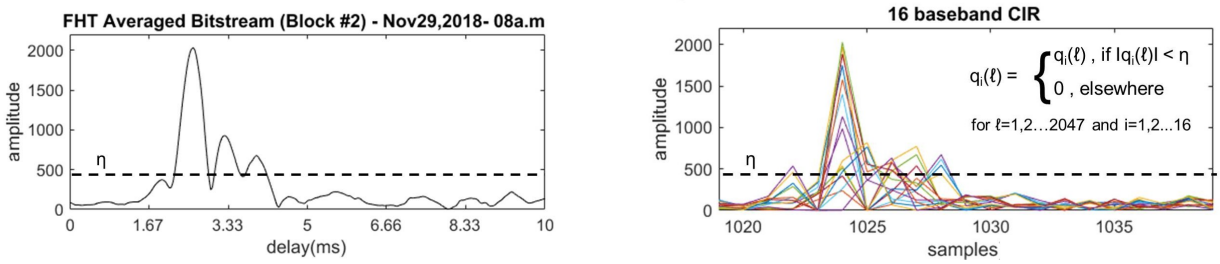

(a) (b)

Figure 3.7: a) Based on data from block #2 (Nov29,2018-08a.m), a FHT of averaged bitstream $r_{ave}(k)$ estimated the channel delay spread. The dashed line represents the threshold for removal of the pilot interference using HCC0; b) Decomposition of a) in 16 baseband CIR $p_i(L)$.

a threshold (η). As shown in Fig. 3.7b, just a few samples are removed from each subset $p_i(L)$, resulting in $p_i^{'}(L)$. However, the tradeoff between the number of zeroed samples and BER is not defined, depending on the channel multipath structure and noise level. To decompress the original message free from most interference, the 16 baseband $p_i^{'}(L)$ are rearranged and an inverse FHT (IFHT) [15, 24, 43] is used.

3.3.3 Hard Synchronization and Message Retrieval

From all 16 rows in $\text{IFHT}_{(16XL)}$, only 8 are summed up to create a single 2047-bit sequence containing the message (3.2):

$$r_{\sum}^{'}(L) = r_1^{'} + r_2^{'} \tag{3.2}$$

where $r_1^{'} = \sum r(i, L)$ for i: 2, 6,...,14 and $r_2^{'} = \sum r(j, L)$, for j: 4, 8,...16. As shown in Sec. 3.3.2, odd rows do not contribute to the summation and a change in sign of r_2 means that these sequences are 180° phase reversed compared to r_1. Using $r_{\sum}^{'}(L)$, hard synchronization is done using cross-correlation peaks from FHT of Mseq31 which precedes the data packets. After synchronization, the receiver retrieves each of the four 480-bit data packets. However, as the thesis is focused on LPD communications, the four 480-bit data packets were also averaged, forming a single 480-bit data sequence.

3.4 Shallow water LPD experiment

As proof of concept, a shallow water experiment was performed in the bay of Arraial do Cabo/Brazil, on Nov 28-29, 2018. Fig. 3.8 shows the Brazilian Navy Institute of Sea Studies Admiral Paulo Moreira acoustic test site, on the coast of Rio de Janeiro/Brazil. A single directional acoustic source and a hydrophone were both assembled in pyramidal frames, posed on the bottom, in a 4 m and 10 m deep water column. The bathymetry changed along with the 600 m range. The source was wired to shore where the transmission system modulated data on a carrier central frequency (f_c) of 7.5 kHz (BW: 3 kHz). The data acquisition system has a sampling rate of 100 kHz and a resolution of 16 bits, but signals were downsampled to 30 kHz, 4 times f_c, before processing. The quantization noise level of 96 dB is reached at approximately 40 kHz, from which the noise power becomes constant (white). Since our system operates in the band 6-9 kHz, the received signals were predominantly perturbed by ocean noise. Mainly caused by the proximity to the city's harbor, the high

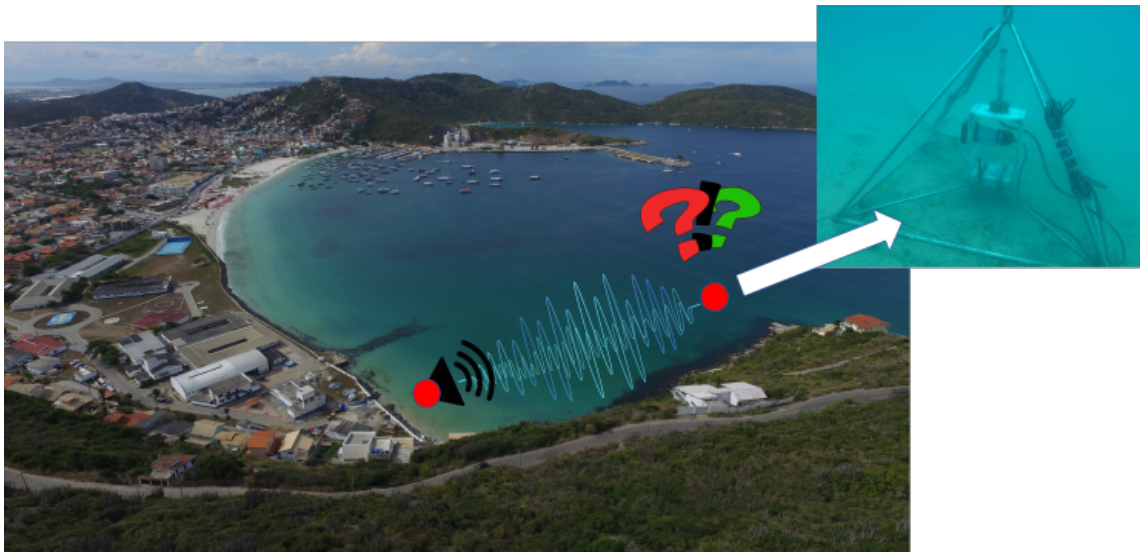

Figure 3.8: The Brazilian Navy Institute of Sea Studies Admiral Paulo Moreira acoustic test site, on the coast of Rio de Janeiro/Brazil. The 2 sides of the communication link had a directional acoustic source and a hydrophone, both mounted on a pyramidal frame posed on the bottom.

broadband noise levels created undesired interference. Thus, to evaluate the performance in different scenarios, the experiment lasted 21 hours with data transmissions occurring once every 30 minutes. Each transmission consisted of two distinct low-power level blocks. In each block, to explore channel temporal diversity, the same bitstream was repeated continuously for 87 seconds (79 sequences), with no guard time between them. Furthermore, the four data packets in each bitstream had the same content.

The received signals were contaminated with impulsive background noise. Thus, the in-band SNR (dB) was estimated according to (2.20), where N was estimated from the period preceding the block #1. Fig. 3.9 presents an in-band spectrogram (6-9 kHz) and the CIR estimated from data recorded on Nov 28, 2018, at 11:30 P.M. and Nov 29, 2018, at 08:00 A.M. Covert communications assume that the transmitted signals are much weaker than the background noise (SNR< -8 dB) within the signal band at the receiver)and that the unknown listener does not have prior knowledge of the transmitted signal [23] . Therefore, LPD signals are not expected to appear in spectrograms, commonly used energy detectors

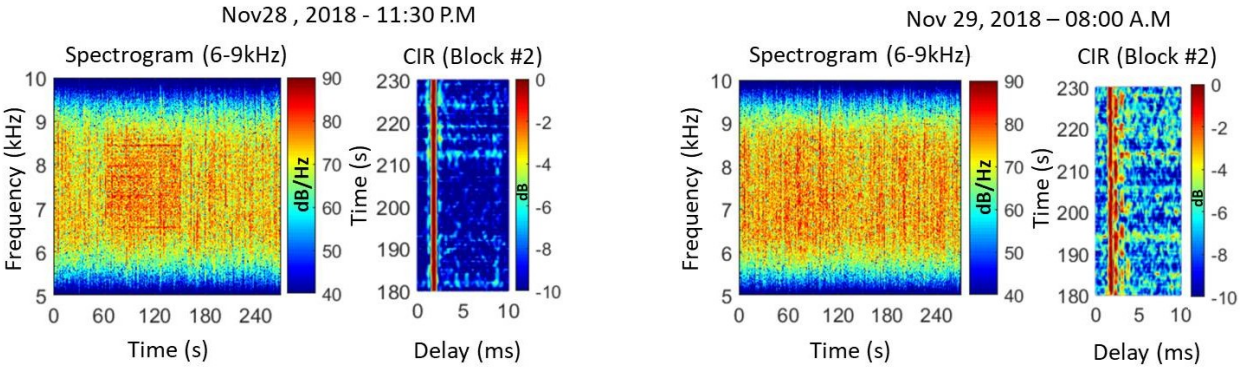

(a) (b)

Figure 3.9: a/b) Left: In band spectrograms from transmissions recorded in Nov 28, 2018 at 11:30 P.M / Nov 29, 2018 at 08:00 A.M. The block # 1 (SNR: -1.4 and -5.9 dB) from 72 to 159 s is minimally visible on the plot (a) but invisible on the plot (b). As SNR decreased, blocks #2 (SNR: -8.1 and -13.2 dB) from 174 to 261 s are invisible in a) and b) as expected. Right: CIR estimated using FHT of bitstreams from block #2 (180 to 230 s).

based on an increase of SNR as a function of time and frequency [15]. At the beginning of the experiment, the source power was set to make block #1 minimally visible (SNR: -1.4 dB) from 72 to 159 s and block #2 undetectable (SNR: -8.1 dB) from 174 to 261 s (Fig. 3.9a, left). But as the channel noise levels varied during the experiment, there were time periods where both blocks were not observed. In Fig. 3.9b (left), the SNR of block #1 and #2 are -5.9 and -13.2 dB.

Figs. 3.9 also expresses the CIR variability in time, estimated using bitstreams from block #2 received between 180 and 230 seconds. Fig. 3.9a (right) shows a low noise level and light multipath environment where the direct arrivals are dominant. This fact may be related to the sea surface state, to a downward refracting SSP, and also to the source directionality, minimizing the interactions of the acoustic waves with the sea surface and bottom. On the other hand, Fig. 3.9b (right) presents higher noise and stronger fading but still short and stable multipath of approximately 2 ms. As each chip/symbol has a duration of 0.58 ms, shorter than the multipath spread, intersymbol interference degraded performance.

3.5 Experimental results

In this work, synchronization was a major concern. Thus, 40 CIR $\mathrm{h}_z(\mathrm{k})$ estimated from data recorded on Nov 29, 2018, at 08:00 A.M (Fig. 3.9) were superimposed. After time gating around the dominant arrivals (200 samples or 6.7ms), Fig. 3.10 a, left) shows that the strongest arrivals of each sequence are not coincident. Thus, soft synchronization of CIR $\mathrm{h}_z(\mathrm{k})$, using the CIR $\mathrm{h}_{1ref}(\mathrm{k})$ as the reference, must be performed before averaging to mitigate interference (Fig. 3.10a, right). Using the averaged bitstream $r_{ave}(k)$, the hard synchronization was performed using a Mseq31 replica. Fig. 3.10b shows the first, second and

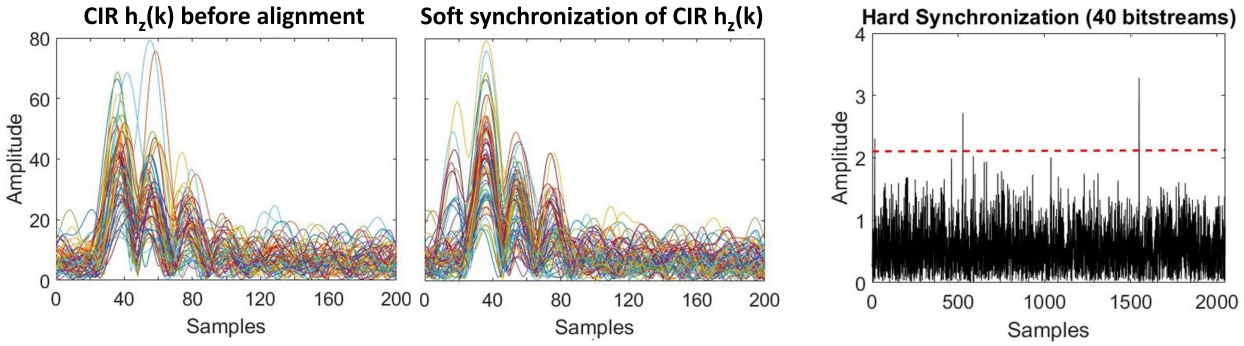

(a) (b)

Figure 3.10: a) Left: The first 40 CIR $h_z(k)$ before alignment. Right) Soft synchronization of $h_z(k)$ in the left, using the $h_{1ref}(k)$ as the reference. b) Hard synchronization of the averaged bitstream composed of sequences in a) shows the first, second and fourth synchronization peaks crossing the threshold (dashed line). Signals from block #2 recorded in Nov 29, 2018 at 08:00 A.M (SNR: -12.7 dB, BER: 3.3%).

fourth synchronization peaks (samples: 14, 525, and 1547), crossing the detection threshold (dashed line). As the SNR was -12.7 dB, the third packet (sample: 1036) was not detected degrading the result (BER: 3.3%).

The proposed system showed stability in this time-varying channel, dealing with both variable noise levels, multipath, and fading. Doppler is generally a problem, in particular with low SNR signals. However, as the source and receiver were maintained steady in the water, both soft and hard synchronizations were performed using zero Doppler Mseq2047 and Mseq31 replicas. To increase the processing gain and to implement error correction, the method performed long coherent averaging of received sequences which reduced the data rate. Fig. 3.11 shows BER and SNR fluctuating in time, for three data rates. The bitstreams of block #1 were averaged during 21.8, 43.6, and 65.4 seconds (20, 40, and 60 sequences). Therefore, the data rate was 22.1, 11, and 7.3 bps, respectively (Fig. 3.11a). Also, the need for averaging is related to the received power level. Thus, just the longer averaging times were considered for the noisier block #2: 43.6 and 65.4 seconds for a data rate of 11 and 7.3

bps (Fig. 3.11b).

During most of the experiment, the in-band SNR of block #1 varied between 0 and -8 dB while the SNR of low power block #2 remained below -8 dB, the arbitrary threshold for covert communications [23]. In both conditions, for chosen data rates, the method was able to provide BER lower than 10^{-2} in most transmissions, including several error-free messages. But Fig. 3.11a presents better BER compared to Fig. 3.11b because of the higher SNR and longer averaging times. Both Fig. 3.11a/b) do not show a significant increase of the BER as SNR decreases, as one could expect. This is probably related to the time-varying channel along the 21h of the experiment where other factors such as the sound speed profile, the sea surface conditions and the multipath structure also played a role, in addition to the noise, during the demodulation of the message. The gaps in Fig. 3.11b were caused by synchronization problems due to an increase in the channel noise levels and degradation in the propagation conditions. No analysis of optimality was performed.

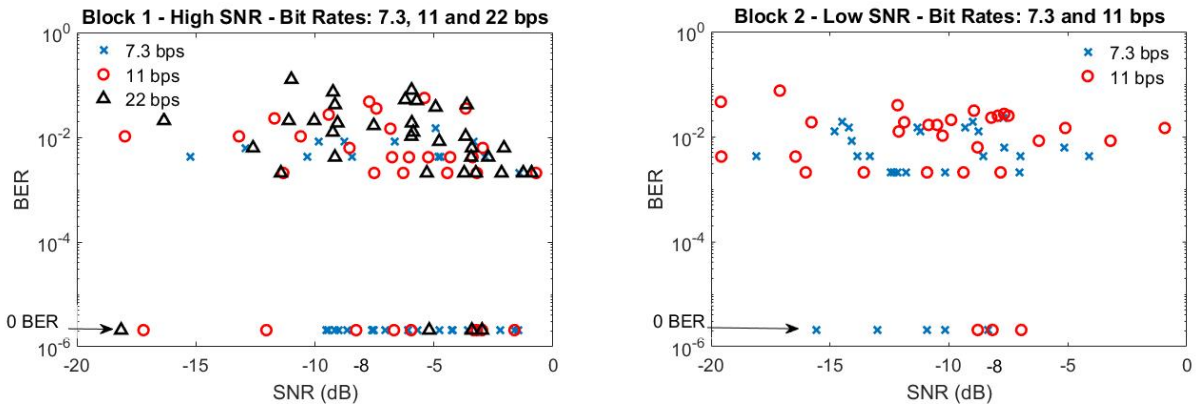

(a) (b)

Figure 3.11: a) Block #1 - BER and SNR fluctuate during the experiment. LPD benchmark: SNR< -8dB. Bit rates: 7.3, 11, and 22 bps; b) Same graph as a), for block #2. Bit rates: 7.3 and 11 bps.

3.6 Discussion

The development of LPD underwater acoustic communication methods has been encouraged in recent years. This chapter presented a new approach and verified its suitability for LPD purposes using simulations and real data. The superimposed training algorithm uses long orthogonal training codes, and therefore, may be extended for multiple users, just modifying the probe code to reduce the mutual interference. Computationally simple, the method explores the channel temporal diversity to increase the SNR at the receiver. A shallow water experiment presented encouraging results. Despite the low bit rate for long averaging times, the proposed approach achieved BER$< 10^{-2}$ for SNR< -8 dB for several received signals.

Chapter 4

The effects of coastal upwelling over low SNR communications in shallow water

Abstract *The influence of oceanographic processes on communications are not well understood. This chapter presents a study on the effects of coastal upwelling over low SNR communications in shallow water using the modeled and real data. Moreover, a correlation between the temperature evolution over time and the communication system performance is presented. Section 4.1 presents the coastal upwelling off the Cabo Frio island and its physical oceanographic mechanism. In Section 4.2, the BioCom'19 experiment is described. The communication system receiver is shown in Section 4.3. Section 4.4 studies the acoustic propagation in an upwelling scenario using the modeling and real data. Section 4.5 studies the CIR variability during upwelling. The temperature evolution vs. communication performance is studied in Section. 4.6. A discussion is presented in Section 4.7.*

4.1 Coastal upwelling off the Cabo Frio island

Coastal upwelling is a dynamical oceanographic process that severely modifies ocean temperature stratification, inducing the movement of cold water towards the sea surface [54]. Previous works reported in the literature have studied and described the functioning of wind-driven coastal upwelling mechanism in several specific locations across the ocean, due to its ecological consequences, carrying nutrient-rich sub-surface water into the euphotic zone, in-

creasing substantially the biological productivity, and therefore, fishing activities [54, 55]. However, the influence of oceanographic parameters over acoustic propagation and communication performance, if any, is not well understood. Therefore, a study based on ocean modeling to understand the role of upwelling in creating shadow coastal zones, reducing the probability of detection of an acoustic source, is presented in [56]. Another work using noncoherent acoustic communication signals showed that the thermocline variability may explain the differences in the modem performance, in terms of bit-error rate (BER) [57].

In this chapter, the main objective is to understand the effects of coastal upwelling over low SNR communications in shallow water. To support the analysis, a small subset of data from the shallow water BioCom'19 experiment [51] was used. The range-dependent bathymetry includes a depression at mid-distance between the source and receivers through which the cold water sips into the region. During the experiment, several sound speed profiles (SSP) were acquired along the propagation track. The temperature profiles were also continuously monitored along the water column at the receiver location. Furthermore, broadband low power coherent bitstreams were continuously transmitted and recorded on a pyramidal array of four hydrophones. Simulations using the range-dependent Monterey-Miami Parabolic Equation model (MMPE) [36] were used to compare the acoustic propagation for upwelling regime SSP. The resulting transmission loss (TL) plots and predicted CIR indicated a complex channel to establish communications, depending on the ocean temperature stratification. Moreover, an analysis was performed to correlate the SNR to the temperature profiles during the experiment. The resulting bit error rates show that the temporal averaging of recorded signals was able to cope with this challenging environment.

4.1.1 The upwelling oceanographic mechanism

The wind-driven coastal upwelling off the Cabo Frio Island, shown in Fig. 4.1, is a complex oceanographic mechanism triggered by the action of the predominant NE/E wind blowing regime, inducing offshore movement of surface water and, therefore, the ascending motion of cold and deep water towards the ocean surface [55, 56]. In the Southern hemisphere, as a consequence of the Ekman transport, the integrated flow of the near-surface ocean points 90^o angle to the left of the wind. Furthermore, there is an inflection of the Brazilian coast from NE/SW to E/W direction at the vicinities of the Cabo Frio region, extending hundreds of km in a straight coastline, and a continental shelf break topography that favors the phenomena. Fig. 4.1 shows that the coast-parallel component of the wind stress induces the offshore transport of water in the surface Ekmann layers, rising the South Atlantic Central Water (SACW) towards the sea surface until a dynamical equilibrium is reached. The upwelling is more intense in summer/spring due to the shallowness of the thermocline and the prevalence

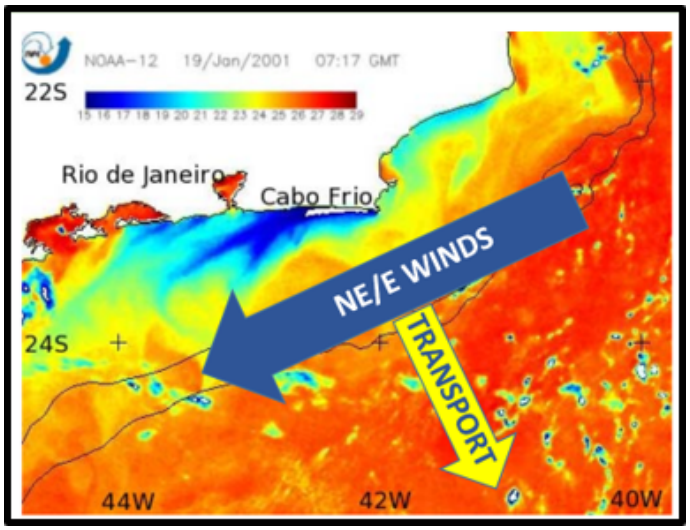

Figure 4.1: Coastal upwelling off the Cabo Frio Island (Brazil). The blue arrow indicates the predominant NE/E winds and the yellow arrow shows the offshore transport of warm and surface water. (Adapted from NOAA, 2001)

of NE/E winds in these seasons [55].

The upwelling phenomena have several implications, changing the marine biota and impacting the ocean temperature stratification. Despite covering just 1% of the ocean, the regions of occurrence are the most productive, contributing around 20% of fishing activities [55]. Furthermore, the sound speed in the ocean is a function of pressure (depth), temperature and salinity, $c = f(p, t, s)$ [58]. Therefore, the mixing of the water masses of different compositions strongly affects the sound speed profiles, influencing the propagation of acoustic signals used for communications.

4.2 The BioCom'19 experiment

The BioCom'19 experiment took place in a semi-enclosed shallow water bay, off Cabo Frio Island (Brazil) from Jan14-18, 2019 (Fig. 4.2a). Described in detail in [51], the experiment focused on biological soundscape monitoring and underwater communications. The exper-

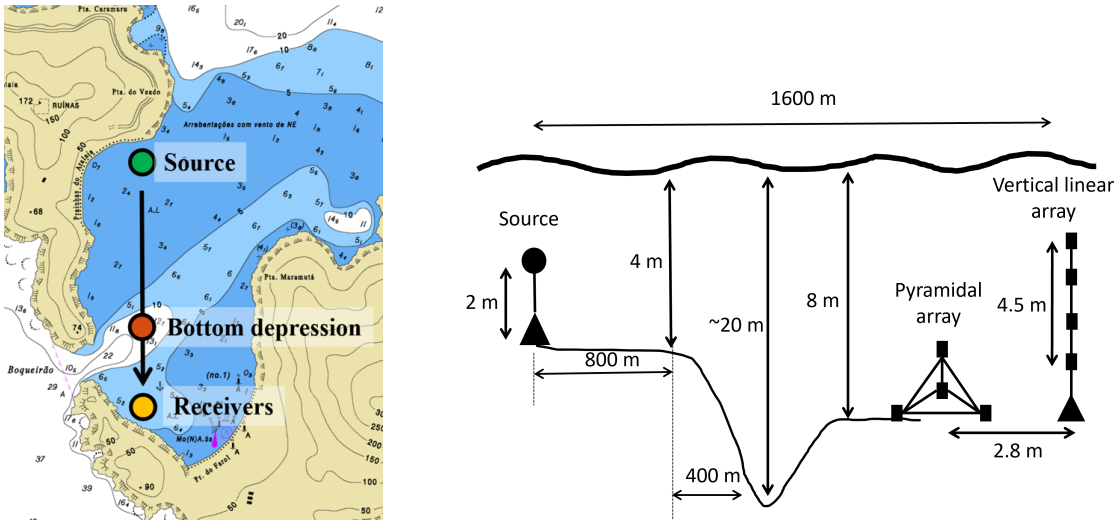

(a) (b)

Figure 4.2: a) The nautical chart shows that the propagation track crosses a bottom depression through which cold water sips into the bay. b) Experimental setup of the BioCom'19 experiment. The source-receiver range is 1600m. The sketch indicates the relative position of the VLA and the pyramidal array, and the approximate location of the bottom depression.

iment took place close to the city harbor and rocky shores with substantial coverage of soniferous invertebrates [59], adding natural broadband impulsive noise to received signals.

The nautical chart in Fig. 4.2 (a) shows the experimental site influenced by the upwelling phenomena in the region of Cabo Frio Island, where one can observe that the bathymetry changes drastically along the propagation path. The strong currents flowing in and out of the bay through the Boqueirão strait created a bottom depression at mid-distance between the source and receivers, also shown as the darker area in Fig. 4.3 (left). The rapid changes in the ocean temperature stratification affect the sound wave propagation [56], making this

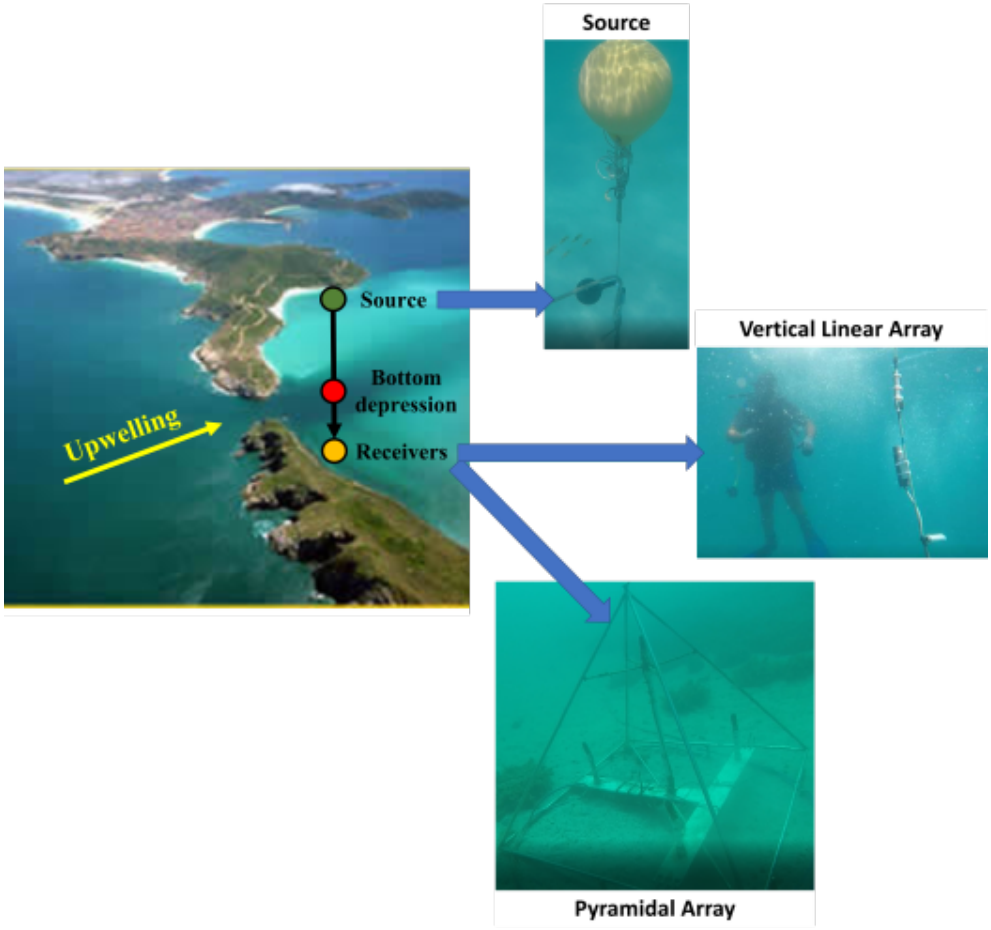

Figure 4.3: Left) An aerial view of the BioCom'19 experiment shallow water site, off the Cabo Frio island (Brazil), indicates the approximate positions of the source and receivers and shows the bottom depression through which cold water sips into the bay. Right) The source (black sphere), the vertical linear array, and the pyramidal array.

a challenging site for underwater communication experiments.

Fig. 4.2 (b) shows the experimental setup. The omnidirectional acoustic source was located at mid-water in a 4 m deep water column, approximately 1.6 km away from the receiver location. To monitor the upwelling, several SSPs were acquired by a CTD at three locations (source, bottom depression, and receiver), reaching depths varying from 4-20m. Furthermore, a time series of temperature profiles were continuously recorded along the water column at the receiver location. Fig. 4.4 shows the temperature profiles from Jan16, 10:45 a.m. to Jan 18,10:30 a.m. where one can observe two upwelling events, with the cold water entering the bay and moving towards the sea surface.

The experiment explored both temporal and spatial diversities to allow error correction through coherent averaging. Thus, a bitstream was repeated 55 times per minute, every five minutes. All four data packets in each bitstream have the same content. Data was recorded on two different geometry arrays of 4 hydrophones each. The vertical line array (VLA) with a 4.5 m aperture was deployed in an 8 m height water column. The triangular pyramidal array

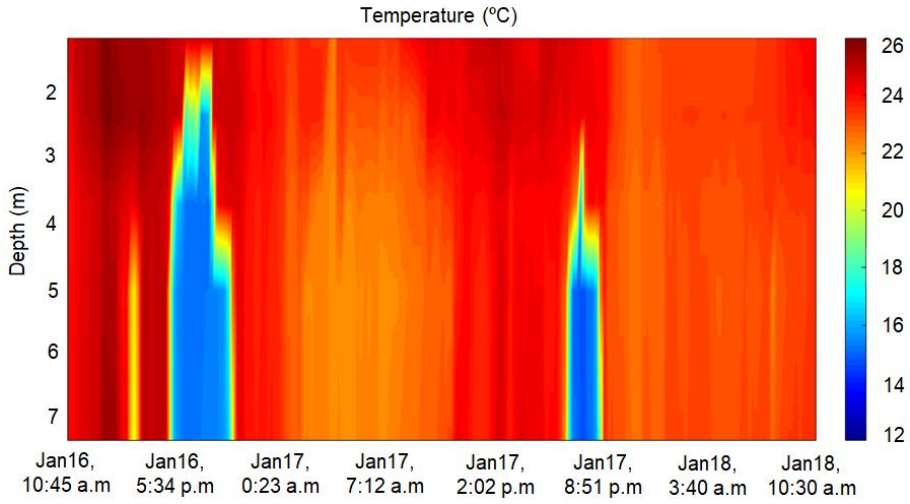

Figure 4.4: Time-series of temperature profiles along the water column at the receiver location, recorded from Jan16, 10:45 a.m. to Jan18, 10:30 a.m. Short-term drastic temperature changes of more than 10 degrees Celsius in a few hours indicate the upwelling occurrences.

was composed of 3 hydrophones in the base,and one at the top, separated by approximately 1 m. The frame was posed at the bottom, approximately 2.8 m from the VLA location. The communication signals were set up with a central frequency of 7.5 kHz, and a bandwidth of 3 kHz. The data acquisition system has a sampling frequency of 52734Hz, but signals were downsampled to 30KHz, 4 times f_c, before processing. The hydrophones have a sensitivity of -174.9 dB re 1V/1μPa and a flat frequency response between 0.1 and 40 kHz.

4.3 The communication system receiver

Despite the multiple hydrophones of the VLA and the pyramidal array (PA), the analysis of the impacts of upwelling over communications is based only on the hydrophone #1 from the PA, placed on the bottom. In the Biocom'19 experiment, the low power superimposed training bitstreams had the same composition as those detailed in Sec. 3.2. The probe and the data have 2047 bits, where data was composed of 4 packets of 480 bit-message. The amplitude ratio between the probe and the data is 5/4. Several packets of 55 low-power superimposed training bitstreams were transmitted, once every 5 minutes, to explore temporal diversity and to perform error correction through coherent averaging. To evaluate the proposed communication system performance in a low SNR environment, the signal power was kept constant during the first 30 minutes, and reduced by 1 dB after each transmission, in the remaining 30 minutes. The signal power variation in addition to the high impulsive noise levels in the site, related to both man-made and biological factors, provided a wide SNR variation for data analysis.

In shallow water, the acoustic energy interacts several times with ocean boundaries, sea surface, and bottom, inducing multiple replicas at the receiver. Fig. 4.5 shows the receiver

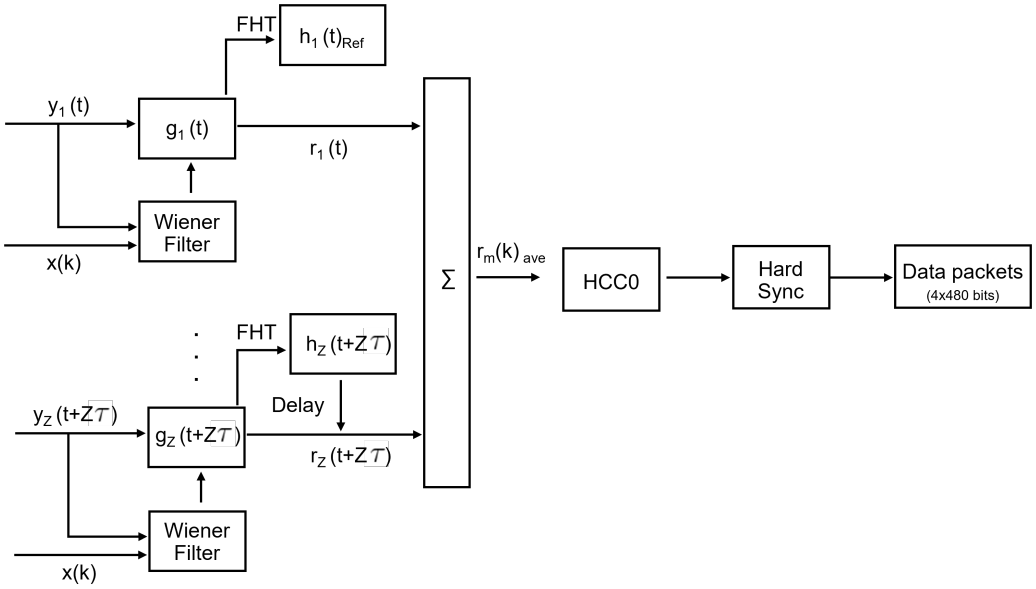

Figure 4.5: Diagram of the single channel communication receiver composed of a Wiener filter for equalization, soft synchronization in time, coherent averaging of Z low power bitstreams, HCC0, hard synchronization and data retrieval.

structure. The CIR were estimated by a FHT of each received sequence $y_z(t + z\tau)$. Each $y_z(t + z\tau)$ was equalized using a Wiener filter to mitigate multipath, where z is the sequence number and τ is the period of the transmitted bitstream. Then, the filtered $g_z(t + z\tau)$ were matched filtered with the M-sequence probe $x(k)$. Based on the strongest peak of the cross-correlation results $h_z(t + z\tau)$, the bitstreams $r_z(t + z\tau)$ were synchronized (time-aligned). To achieve a high processing gain at the receiver the bitstreams were coherently averaged. The error-corrected bitstream $r_m(k)_{ave}$, of each m channel from the pyramidal array, was processed using the HCC0 method to remove the probe interference. After a hard synchronization and averaging of the four 480-bit data packets, the message is retrieved [60].

4.4 The acoustic propagation in an upwelling scenario

In order to better understand the acoustic propagation in this complex environment, the communication channel was modeled using geological parameters and approximate bathymetry

for the experimental site. Based on the Cabo Frio region substratum composition , the bottom was assumed as fine sand with a compressional speed of 1684 m/s [35]. Two representatives SSP, upwelling (Fig. 4.6 (top plot, right)) and slightly downward refractive SSP (Fig. 4.6 (bottom plot, right)), collected from CTD at the depression on Jan16, 3:32 p.m., and Jan17, 1:38 p.m. were inserted in the MMPE model to simulate the propagation for the same center frequency and bandwidth of the signals transmitted in the experiment. For both SSP, the transmission loss (TL) plots show multiple interactions of the acoustic energy with the bottom and sea surface, between the source location and the valley (Fig. 4.6, left). However, along this deeper region, for the upwelling condition, the propagation is much different. As one can observe in Fig. 4.6 (top plot, right)), at the depth of 9m, there is an

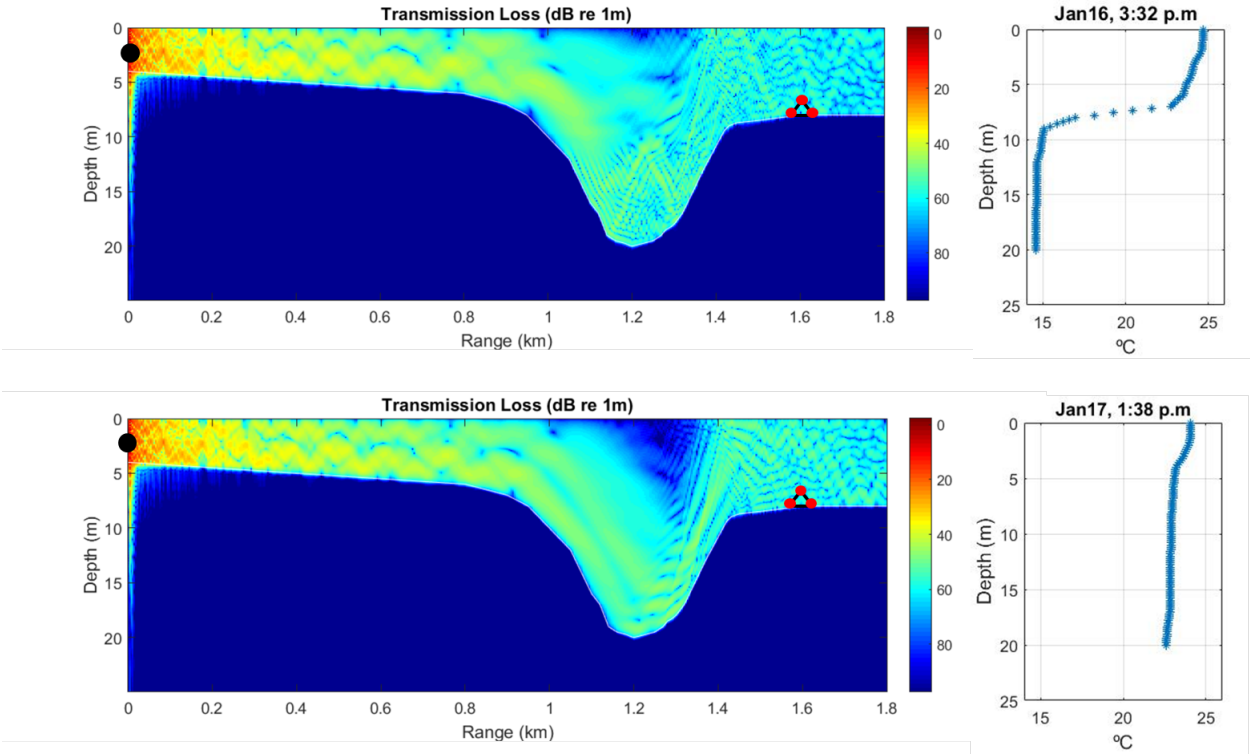

Figure 4.6: Numerical estimations of transmission loss (TL) using the MMPE acoustic model ($f_c = 7.5kHz, BW = 3kHz$). The source (black dot) is placed mid-water in a 4 m deep water column. The pyramidal array (red dots) is located 1.6 km far from the source, posed at the bottom in an 8 m water column. Calculations were performed for an upwelling SSP recorded on Jan16, 3:32 p.m (top plot), and a slightly downward refracting SSP from Jan17, 1:38 p.m (bottom plot).

abrupt reduction of temperature of approximately 10°C in just 3m, creating two layers of distinct propagation. Therefore, the TL plot shows that most of the energy refracts towards the bottom and becomes trapped in this depression, reducing significantly the energy available at the hydrophones (Fig. 4.6 (top plot, left)). Conversely, for the slightly downward refracting SSP, the energy propagates following the bottom geometry, and therefore more energy reaches the hydrophones (Fig. 4.6 (bottom plot, left)).

Fig. 4.7 and 4.8 show both the CIR estimated from data recorded by hydrophone #1 (three plots on the left) and the noiseless CIR predicted by the MMPE acoustic model (plot on the right), for the upwelling and no upwelling SSP, respectively. For the upwelling SSP condition (Jan17, 7 p.m), Fig. 4.7 (left) shows the 55 estimated CIR. The noisy CIR exhibit low amplitudes and a time-varying fading. Several bitstreams cannot be even detected, as one can observe between seconds 10 to 20. On the other hand, in a no upwelling condition, for a slightly downward refracting SSP (Jan17, 2 p.m), the estimated CIR show higher amplitudes. In an almost isothermal condition, all bitstreams were detected, pointing to a more stable propagation channel with hydrophones receiving more energy (Fig. 4.8 (left)).

To observe the multipath structure, the two plots in the middle of Fig. 4.7 and 4.8 focus on two specific CIR, indicated by the red dots. For the upwelling SSP, the low SNR CIR #33 and #50 present a long delay spread of approximately 10 ms, including a strong arrival much before the most significant peak that complicates the synchronization and equalization processes. However, for the slightly downward refracting SSP, the CIR #12 and #42 present a higher SNR, showing more energetic arrivals and a shorter multipath compared to the upwelling CIR. In Fig. 4.7 and 4.8 (right), the CIR predicted by MMPE show the fading and multipath structure in agreement with the estimated CIR. The communication system

uses several consecutive M-sequences to estimate the channel. Performing a comparison, one can observe a high degree of similarity between the CIR from MMPE and the CIR #50 and #42 from real data. This is an interesting result and may validate the accuracy of the numerical simulation, based on real data.

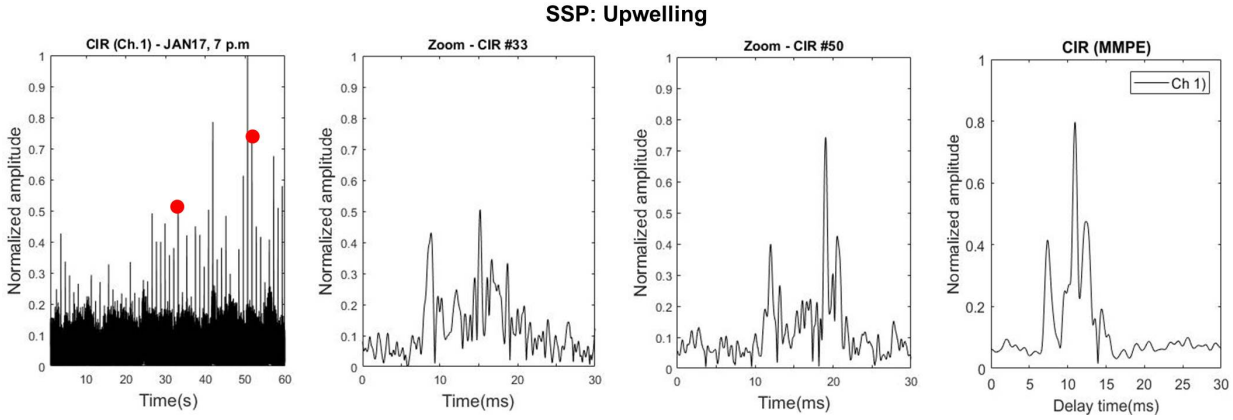

Figure 4.7: For an upwelling SSP, the first three plots, from left to right, show the CIR estimated from the 55 bitstreams recorded by hydrophone #1, and the multipath structure for the sequences #33 and #50 (red dots), respectively. On the right, a CIR shows the multipath arrivals predicted by the MMPE model, for a receiver depth of 7m, approximately the same of hydrophone #1 of the pyramidal array.

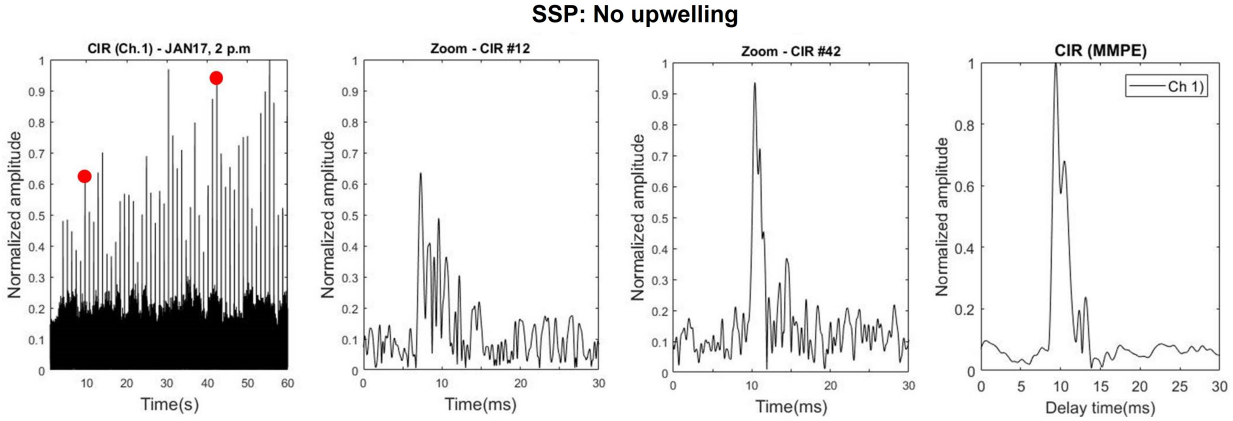

Figure 4.8: For a no upwelling SSP, or a slightly downward refracting SSP, the first three plots on the left show the CIR estimated from the 55 bitstreams recorded by hydrophone #1, and the multipath structure for the sequences #12 and #42 (red dots). On the right, a CIR shows the multipath arrivals predicted by the MMPE model, for a depth of 7m, approximately the same of hydrophone #1 of the pyramidal array.

4.5 CIR variability during upwelling

In this section, the analysis of CIR variability during upwelling is performed based only on the T profiles. The sea surface conditions, important factors that impact channel variability and the multipath structure due to the sea surface reflections, are not considered here as there was no monitoring of the sea surface state during the experiment.

Figure 4.9 (bottom plot) shows the temperature evolution in time measured by a thermistor placed at the same depth of the hydrophone #1, approximately 1.5 m above the bottom. The temperature vs. time plot shows several upwelling events. However, to observe the channel degradation as upwelling occurs, Fig. 4.9 (top plots) presents three different CIR structures estimated from signals recorded by hydrophone #1 (top of the pyramidal array) in a restricted time frame from Jan. 17, 4 p.m. to 8:30 p.m (top, left to right).

On Jan. 17, from 4 p.m. to 7 p.m., the temperature at the receiver remained approximately stable. However, the structures of the two CIR shown in Fig. 4.9 (top plot, left and middle) indicate the occurrence of the upwelling. As cold water seeps into the bay through the depression located at mid-range between the source and the receiver, the sound speed profiles (SSP) changed from a warm isothermal to a downward refracting condition. At 4 p.m., the CIR presents stronger arrivals and a short multipath spread of approximately 5 ms. However, at 7 p.m., the CIR presents weaker arrivals, spreading over more than 10 ms. As the temperature at the receiver is still around 24°C, one can infer that the upwelling process has already started, mixing cold water with warm layers along the propagation track and therefore, degrading the CIR. Comparing both CIR plots (4 p.m. and 7 p.m.), one can expect a severe degradation of the communication system due to the longer multipath

spread and the reduction of the available acoustic energy at the receivers. As the cold water spread throughout the channel and moved towards the sea surface, a drastic short-term drop in temperature of about 10°C was observed at the receiver location from 7 p.m. to 8:30 p.m. Observing the respective CIR shown in Fig. 4.9 (top plot, middle and right), one can conclude that the channel evolved from a downward refracting SSP, when less energy reaches the receivers and severe multipath arrives from bottom interactions inside the valley, to a cold isothermal SSP which allows an even ensonification of the channel. Thus, at 8:30 p.m., the arrivals are strong and the CIR presents a short multipath spread of approximately 2 ms, indicating an improvement in the system performance.

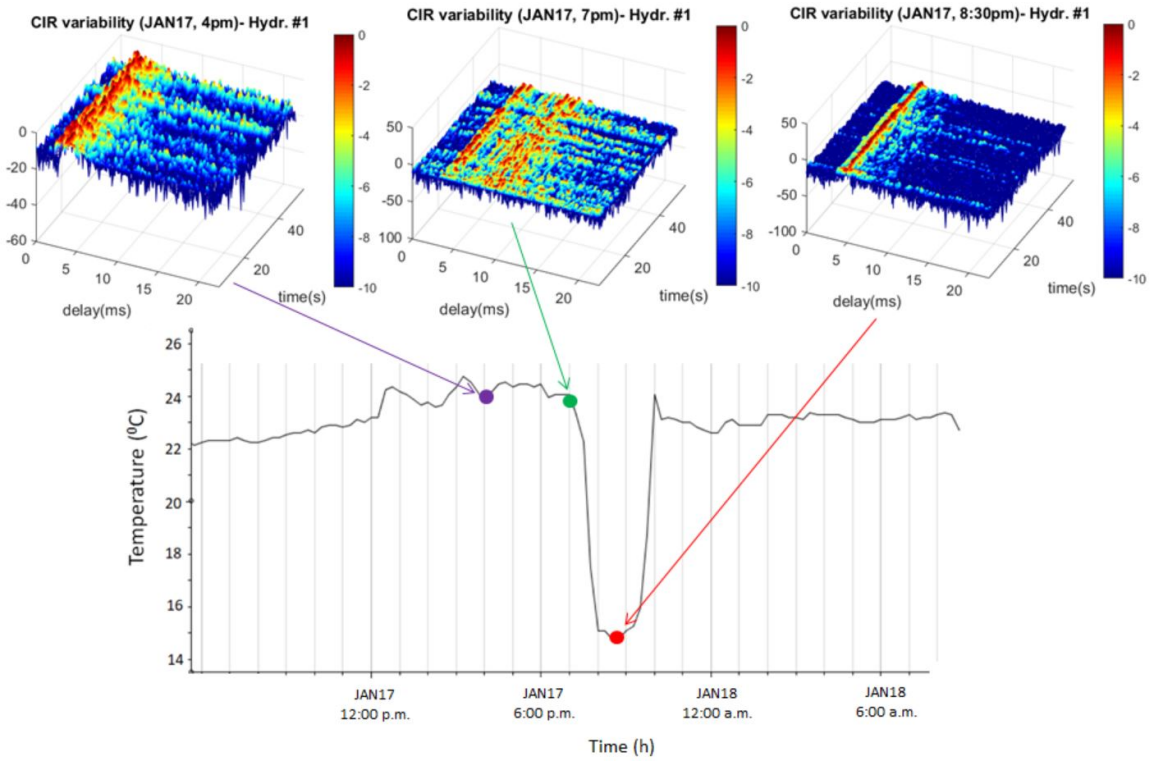

Figure 4.9: Top plot: CIR variability in a restricted upwelling time frame from Jan. 17, 4 p.m. to Jan. 17, 8:30 p.m. Bottom plot: temperature evolution in time, measured by a thermistor located close to hydrophone #1 at the top of the pyramidal array, approximately 1.5m above the bottom.

4.6 Temperature evolution vs. Communication performance

Coherent communications are generally affected by Doppler effects. However, in this experiment, as the source and receiver were maintained steady in the water, signal processing was performed using zero Doppler probe replicas. The in-band SNR (dB) for channel #1 was estimated according to (2.20), using 20 sequences ($Z = 20$), where N was estimated from a period after transmissions.

For the time window from Jan17, 1 p.m. to Jan18, 7 a.m., the SNR or temperature vs. time plot (Fig. 4.10 (top plot)) shows the correlation between the upwelling indicated by the sensor temperature close to the top of the array, and the signal power measured by the hydrophone #1. Observing the SNR and temperature evolution in time, the SNR starts to decline several hours before the climax of the upwelling at 8 p.m., when the cold water reaches the array location. This may be an indicator of the upwelling occurrence. Despite the T around 24°C at the receiver location, from 2 p.m. to 7 p.m., as cold water sips into the bay, temperature stratification along the propagation track changes so that more energy refracts to the bottom and becomes trapped in the depression. When the cold water reaches the T sensor location, between 7 p.m. and 8 p.m., the channel presents an almost isothermal condition (slightly downward refracting SSP). Thus, the SNR increases as more energy reaches the sensors.

In addition to the ocean temperature stratification, the high noise levels in the region, related to both man-made and biological factors, and the severe multipath structure that changes for each received signal also contributed to hampering the demodulation of the

received low power signals.

Fig. 4.10 (bottom plot) shows the BER vs.Time estimated from hydrophone #1. To evaluate the single channel system robustness and to perform error correction in this challenging environment, the BER were estimated using 20 bitstreams (22 bps). Fig. 4.10 (top plot) shows that a large range of SNR (-5.2 to 9.1 dB). During the upwelling, as propagation conditions changed, the single hydrophone system achieved BER $> 10^{-2}$. As the channel

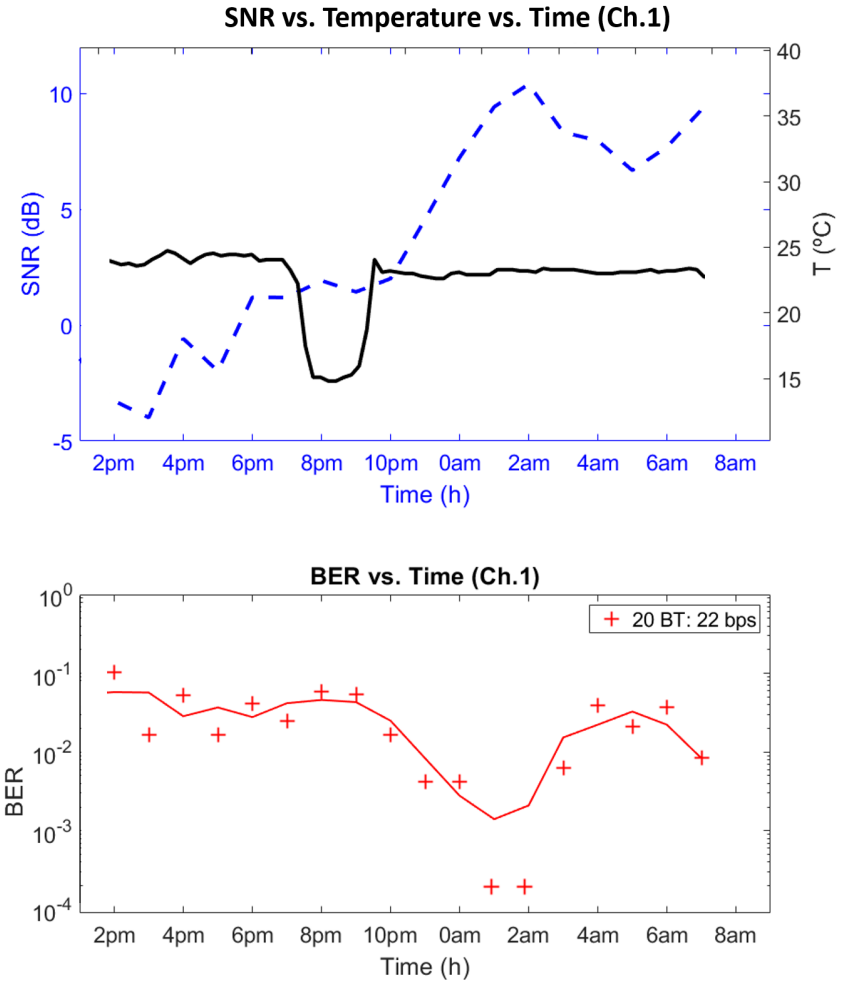

Figure 4.10: Top plot: SNR vs. Temperature vs. Time measured at the array location from Jan17, 1 p.m. to Jan18, 7 a.m. The dashed line (blue) indicates SNR estimated by the hydrophone #1 using 20 bitstreams. Superimposed on the SNR plot, the temperature profile (black) estimated by the sensor close to the top of the array. Bottom plot: BER vs. Time for an effective bit rate of 22 bps, equivalent to averaging for 22 seconds (20 bitstreams). The red line represents a smooth fitting curve of data.

returned to a more stable condition, SNR increased and the communication system retrieved BER $< 10^{-2}$, including error-free messages, for consecutive hours. However, the BER curve does not follow the SNR trend, as one could expect, because the signal demodulation depends on some other factors than the noise levels such as the multipath structure, and the efficiency of the error correction through coherent averaging.

4.7 Discussion

In this chapter, we studied the effects of the upwelling oceanographic phenomena over low SNR communications in shallow water, based on modeling and on a small subset of data from the BioCom'19 experiment. Improving knowledge about the oceanographic processes over communication signals may help to develop systems suitable for sensors operating in these harsh environments, saving power and reducing acoustic pollution. The acoustic propagation for the upwelling and slightly downward refracting SSP were simulated using the Monterey-Miami parabolic equation model. The CIR predicted by the MMPE model were in agreement with data from the experiment. The TL plot indicated a severe multipath in both situations, but a reduction of available energy at the receiver for the upwelling SSP, as the sound became trapped inside the depression through which the cold water sips into the bay. The author analyzed the SNR vs. temperature vs. time and the BER plots for the hydrophone at the top of the array. A reduction of the SNR indicates the occurrence of the upwelling where water masses of different temperatures mix, affecting the propagation. Thus, the communication system may be used, indirectly, to monitor the upwelling phenomena using low-power acoustic signals, instead of conventional temperature sensors.

Chapter 5

Coherence as a criterion for multichannel combining and the double Wiener filter

Abstract *This chapter presents a study on both temporal (TCOH) and spatial (SCOH) coherence of low power signals transmitted during the BioCom19, including a criterion for multichannel combining. Dealing with coherent communications, in which the phase carries the information, understanding the temporal and spatial coherence in a challenging environment may also contribute to improving the communication system. Another topic considered in this chapter is a double Wiener filter for single-channel systems which is proposed to mitigate the residual intersymbol interference that affects the signal coherence. Section 5.1 defines both temporal and spatial coherence and presents a criterion for multichannel combining. Section 5.2 presents the double Wiener filter for low SNR communications. In Section 5.3 a brief discussion about the topics presented in the chapter.*

5.1 Coherence and multichannel combining

Much effort has been dedicated to measuring and understanding coherence in shallow water. Coherence (COH) describes the rate of signal fluctuation, in time or space. Defined as a statistical measure of the change of a waveform, coherence depends on both amplitude and phase of the signal [61, 62]. Previous work reported in the literature measured both temporal and spatial coherence in shallow water for different reasons. In [61], DeFerrari

studied the propagating modes decorrelation of low-frequency broadband transmissions in shallow water, at a range of 10 km, and compared results to those of a numerical model. In [62], Yang measured temporal coherence in three shallow-water sites with low to high internal wave activity using signals with frequencies from 1.5 to 20kHz, in a range up to 42 km. Therefore, an analysis was conducted on the relationship between coherence, source frequency, range, and sound speed profile.

In this section, the main goal is to understand the impact of both temporal (TCOH) and spatial coherence (SCOH) on low SNR communications in an upwelling channel and how to use coherence as a criterion to perform multichannel combining. Data presented here are a small subset from those recorded during BioCom'19 on JAN17, 2019 - 11 a.m by the vertical linear and pyramidal arrays. Thus, coherence covering short periods (seconds) will be used to express the rate of signal fluctuation in time and space, influencing the time of integration and therefore the effective bit rate of the communication system. All four channels of both pyramidal and vertical linear arrays are analyzed independently. Based on estimated TCOH and SCOH, channels are combined to improve the gain of the array. Assuming that noise is uncorrelated between channels, coherent averaging of several sequences increases the SNR and thus, reduces the bit error rate (BER). All coherence estimates are matched to the BER to understand implications over receiver performance. Both arrays are also compared to determine the advantages of their geometry.

5.1.1 Coherence definition

Coherence measures, in a statistical sense, the difference in waveform and depends on the amplitude and phase of the signals. Coherence is estimated by the autocorrelation of the

signals separated by a delay-time (temporal coherence) or distance intervals along an array of sensors (spatial coherence), normalized by the power of the signals as given by

$$COH(t,\tau) = \frac{\left\langle |h^{\dagger}(t)h(t+\tau)|^2 \right\rangle}{\langle h^{\dagger}(t)h(t)\rangle \langle h^{\dagger}(t+\tau)h(t+\tau)\rangle} \tag{5.1}$$

where h(t) is a channel impulse response (CIR) obtained after matched filter pulse compression of the received signals, τ is the lag time, $\langle\rangle$ denotes ensemble average over time t and † denotes complex conjugate.

5.1.2 Temporal Coherence

Fig. 5.1 (a) shows the single channel receiver diagram. The TCOH was estimated before and after the channel equalization. Before equalization, each received bitstream $y_Z(t+Z\tau)$ was used to estimate the channel impulse responses $h_z(t+Z\tau)$ through M-sequence $x(k)$

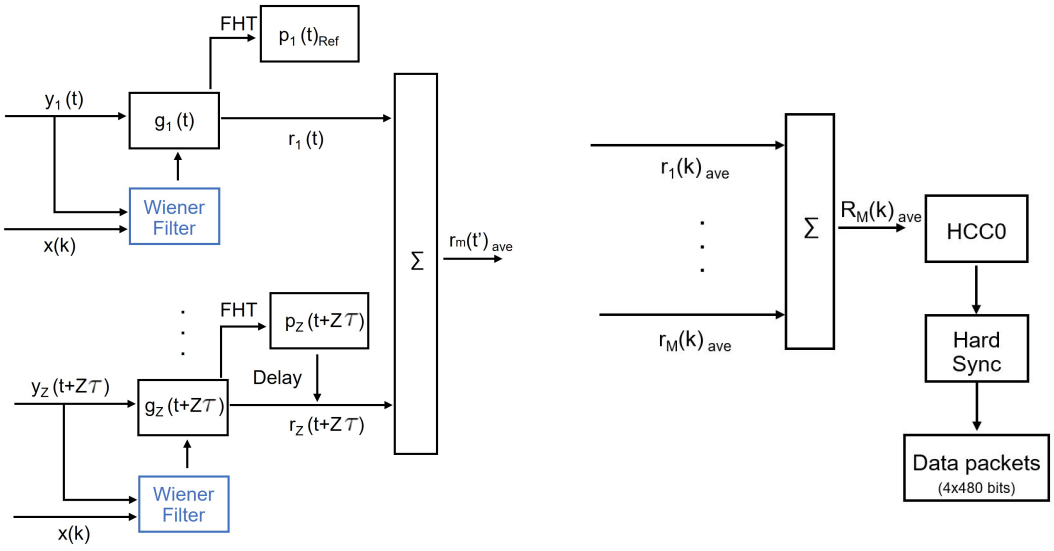

(a) (b)

Figure 5.1: a) Diagram of the communication system, in time, shows the following steps: channel equalization (single Wiener filter), soft synchronization, and temporal coherent averaging of Z received bitstreams. b) Diagram of the communication system, in space, shows the multichannel combining, probe interference removal (HCC0), hard synchronization, and data retrieval.

crosscorrelation. In a low SNR environment, time-gating the CIR can avoid the inclusion of excessive noise in the calculations of TCOH, improving results. Thus, an arbitrarily defined section of 100 ms of each CIR including all the dominant multipath arrivals was selected. Based on these time-gated $h(t)$ and choosing the first CIR $h_{1Ref}(t)$ as the reference, the TCOH of bitstreams arriving at later times can be calculated using (5.1). Fig. 5.2 (a/b) (upper plot) shows that multipath severely degrades TCOH of signals recorded by the hydrophone #3 from the VLA and hydrophone #4 from the pyramidal array.

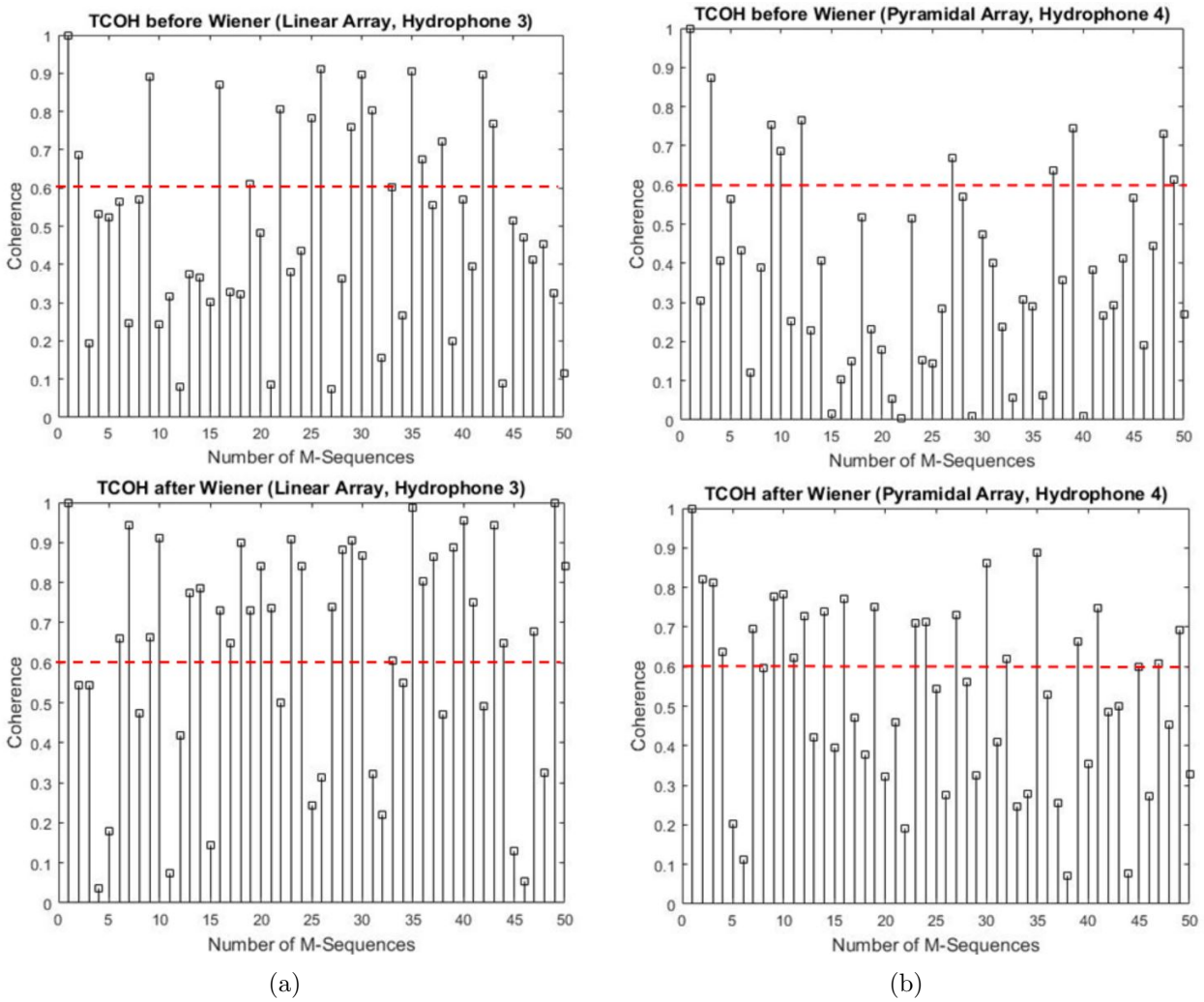

Figure 5.2: a) Temporal coherence before (top plot) and after Wiener filter (bottom plot) of bitstreams recorded by hydrophone #3 of the vertical linear array. Dashed line in red, at 0.6, marks the threshold for TCOH; b) Temporal coherence before (top plot) and after Wiener filter (bottom plot) of bitstreams recorded by hydrophone #4 from pyramidal array. Dashed line in red, at 0.6, marks the threshold for TCOH

To estimate TCOH after the Wiener filter equalization, the received signals $y_Z(t + Z\tau)$ were processed with a Wiener filter. Using filtered $g_Z(t + Z\tau)$, the multiple channel impulse responses $p_z(t + Z\tau)$ were estimated. After time-gating the filtered CIR, TCOH was recalculated improving results. Fig. 5.2 (a/b) (bottom plot) shows a significant improvement of TCOH using filtered signals. When the resulting TCOH, estimated over the filtered sequences, was above a given threshold ζ, the respective bitstreams were coherently averaged. The averaged bitstream $r_{ave}(t)$ represents the channel in the SCOH calculations.

5.1.3 Spatial Coherence

Fig. 5.1 (b) shows the multichannel receiver diagram. SCOH between different channels of the same array can also be determined using (5.1), replacing time $(t + \tau)$ for the hydrophone spacing (η). SCOH was calculated using the averaged bitstream $r_{ave}(t)$, formed by Z sequences $r_Z(t + Z\tau)$ whose TCOH were above a certain threshold ζ. For each channel, the CIR $p_{ave}(\eta)$ was estimated by matched filtering the averaged signal $r_{ave}(t)$ with the transmitted bitstream replica $x(k)$. After time-gating $p_{ave}(\eta)$ from all four channels, these sequences were aligned in time to correct the misalignment of the wavefront and the array. As the phase shifts related to the position in the array were corrected, SCOH was estimated between two channels choosing any CIR $p_{ave}(\eta)$ as the reference.

The SCOH above a threshold ζ is the criteria to perform multichannel combining. Previous work [62] showed that coherence of approximately 0.8 was required to process communication signals. However, improvement was achieved by combining sequences in which TCOH and SCOH were above a lower threshold, placed at 0.6. Therefore, the averaged bitstreams of all channels were combined to improve the gain of the array. But if SCOH was below ζ,

the channel was discarded as it degraded the combined result.

5.1.4 Communication performance results

In this section, the in-band SNR (dB) for each independent channel was estimated according to (2.20), using 50 bitstreams ($Z = 50$), where N was estimated from a period after transmissions. For multichannel combining, the in-band SNR (dB) was estimated using (2.21). Fig. 5.3 (a) shows the evolution of CIR for the vertical linear array, from bitstreams recorded by hydrophone #1 and hydrophone #3, installed 1.5 m and 4.5 m above the bottom in approximately 8 m water depth, respectively. One can observe that signals recorded on hydrophone #3 show severe multipath and an in-band higher noise level compared to hydrophone #1. The average SNR were SNR_{ave}Ch#1= -0.77 dB and SNR_{ave}Ch#3= -2.41 dB, but SNR fluctuates according to the number of sequences used in the calculations. Therefore, signals decorrelate in time much faster in channel #3 than in channel #1.

TCOH for channel #3 is shown in Fig. 5.2 (a), before and after the Wiener filter. Using the threshold (dashed line) as a reference, one can observe that the instantaneous TCOH exhibits a high degree of fluctuation. The large variance may be related to the upwelling oceanographic processes in the region of the experiment that affects the propagation conditions. These results of TCOH impact directly SCOH and data retrieval. Table 5.1 shows SCOH, BER, and SNR for several combinations of channels based on TCOH estimated previously. All SCOH estimations including channel #3 were below the 0.6 threshold and the corresponding BER were deeply degraded due to the high noise levels in the channel. Therefore, channel #3 was discarded and the combination of channels #1,2 and 4 retrieved the transmitted data with a lower BER.

Fig 5.3 (b) shows the evolution of CIR for the pyramidal array. Hydrophone #1 was placed at the top of the pyramid and #4 was posed in the bottom over the base of the array. As this array had all four hydrophones just a few wavelengths from each other, one could expect that the signals in the channels were similar and noise correlated. However, comparing channels in Fig. 5.3 (b), one can observe that both noise levels and multipath were different in time and space. Averaging 50 sequences, the SNR_{ave}Ch#1= -1.27 dB and SNR_{ave}Ch#4= -1.64 dB. Also, both channels present several arrivals of high amplitude, but

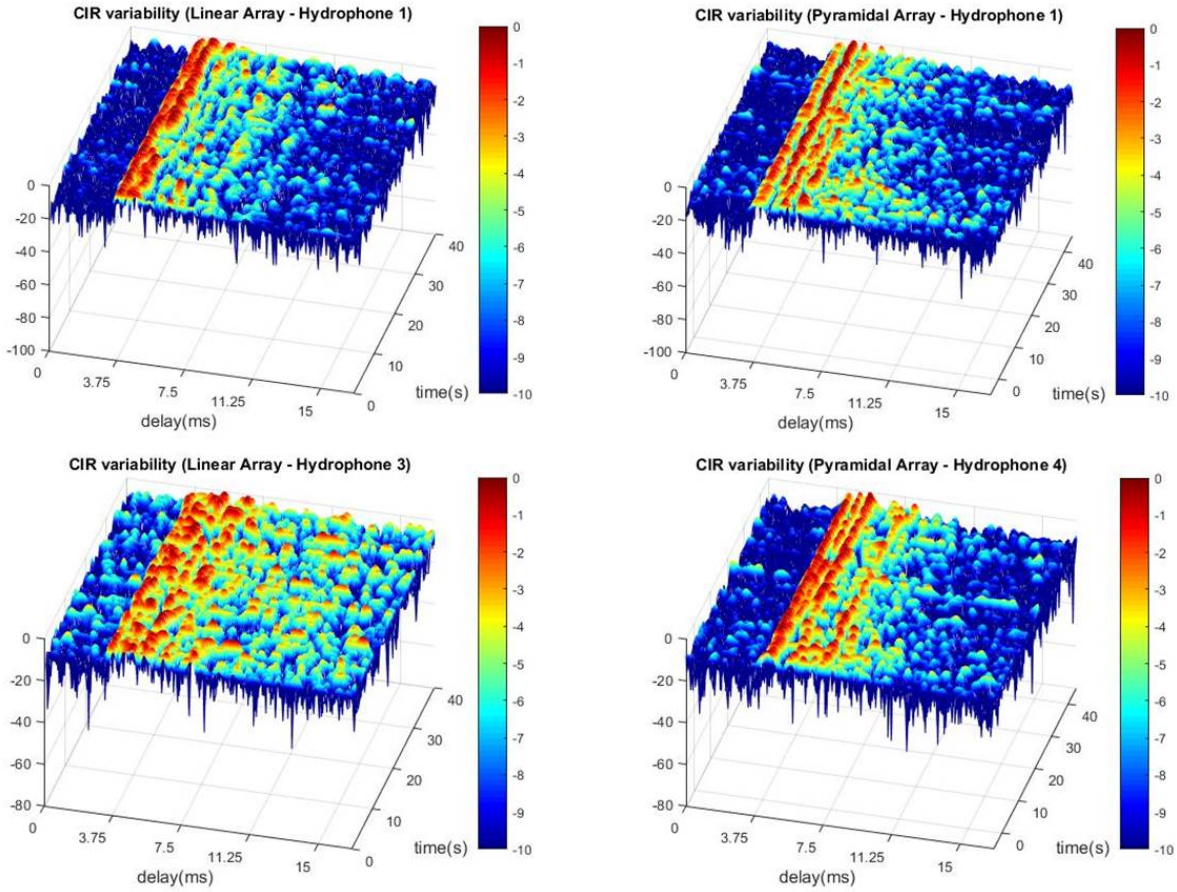

(a) (b)

Figure 5.3: a) CIR variability in time, estimated using 50 bitstreams (Fc:7.5 kHz, BW: 3 kHz). Data were recorded by hydrophone #1 (top plot) and #3 (bottom plot) of the vertical linear array, installed at 1.5 m and 4.5 m above the bottom in approximately 8 m water depth. b) CIR variability in time, estimated using 50 bitstreams (Fc:7.5 kHz, BW: 3 kHz). Data were recorded by hydrophone #1 (top plot) and #4 (bottom plot), installed at the top (1m above the bottom) and at the base of the pyramidal array.

Table 5.1: Vertical array: SCOH[1], BER and SNR from multichannel combining, averaging 10 and 20 bitstreams (44 and 22 bps)[2]

	10 bitstreams (44 bps)			20 bitstreams (22 bps)		
Channels	SCOH	BER %	SNR	SCOH	BER %	SNR
1+2	0.61	1.2	-3.7	0.91	1.8	-3.4
1+3	0.30	34.2	-9.9	0.54	9.6	-10.2
1+4	0.70	0.8	-0.4	0.75	1.2	-0.3
2+3	0.29	34.5	-5.3	0.39	15.2	-11.5
2+4	0.82	1.8	+0.5	0.95	4.3	+0.5
3+4	0.42	19.5	-1.2	0.21	18.5	-1.1
1+2+3+4		5.8	-2.2		3.5	-1.8
1+2+4		2.4	-1.8		1.5	-0.6

[1] SCOH: Spatial coherence
[2] The effective bit rate is related to the number of the averaged bitstreams

channel #4 presents strong and much-delayed multipath at 7.5 ms which complicated data retrieval. The combination of severe multipath and high impulsive noise in the band deeply degraded TCOH, especially for channel #4 (Fig. 5.2 (b) (top plot)). Even after filtering the bitstreams, most of the recalculated TCOH continued lower than the 0.6 threshold (Fig. 5.2 (b) (bottom plot)).

Table 5.2 shows SCOH, BER, and SNR for combinations of the channels of the pyramidal array. Based on SCOH estimations, the channel to be discarded was the #4. In a low SNR environment, repetition of the same signal is used as an error correction tool. In general, longer averaging times provide lower BER but reduce the effective bit rate. Averaging over 10 bitstreams, approximately 10 seconds, the effective bit rate was 44 bps against 22 bps for 20 sequences. Defining an optimum averaging time was a hard task due to signal fluctuations in time and channel noise levels. But the use of the array increased the processing gain, even if the sensors were just a few wavelengths from each other. Even not taking advantage of spatial diversity along the water column as the vertical linear array, the pyramidal array still

Table 5.2: Pyramidal array: SCOH[1],BER and SNR from multichannel combining, averaging 10 and 20 bitstreams (44 and 22 bps)[2]

	10 bitstreams (44 bps)			20 bitstreams (22 bps)		
Channels	SCOH	BER %	SNR	SCOH	BER %	SNR
1+2	0.62	6.2	-5.1	0.73	0.2	-3.4
1+3	0.69	4.3	-4.2	0.64	2.7	-2.8
1+4	0.44	10.7	-3.9	0.49	0.3	-2.5
2+3	0.71	5.1	-6.1	0.67	4.3	-4.2
2+4	0.56	12.2	-5.8	0.54	1.2	3.9
3+4	0.51	9.2	-4.8	0.59	6.8	-3.2
1+2+3+4		7.3	-5.1		4.4	-3.7
1+2+3		3.3	-4.2		0.5	-2.8

[1] SCOH: Spatial coherence
[2] The effective bit rate is related to the number of the averaged bitstreams

provided low BER.

5.2 Double Wiener filter

This section proposes a double Wiener filter scheme, for low SNR communications. To mitigate residual intersymbol interference over the temporal averaged bitstream $r_m(k)_{ave}$, a second Wiener filter is applied before the probe removal (HCC0). The objective is to improve the communication system's robustness during the upwelling occurrence. To demonstrate the double Wiener filter approach, a small subset of data from the BioCom'19 experiment (Sec. 4.2) recorded by the four hydrophones of the pyramidal array is employed. In the previous section, the estimated CIR were compared for different temperatures at the receiver depth to observe the degradation of the communication system over time. Thus, to evaluate the performance in terms of bit error rate (BER) and MSE, the four channels were processed independently. Moreover, the BER vs. SNR and the MSE vs. time were plotted to compare the single and double Wiener approaches.

5.2.1 Communication system receiver diagram

Figure 5.4 presents the single channel receiver diagram of the proposed double Wiener filter communication system [46–48].

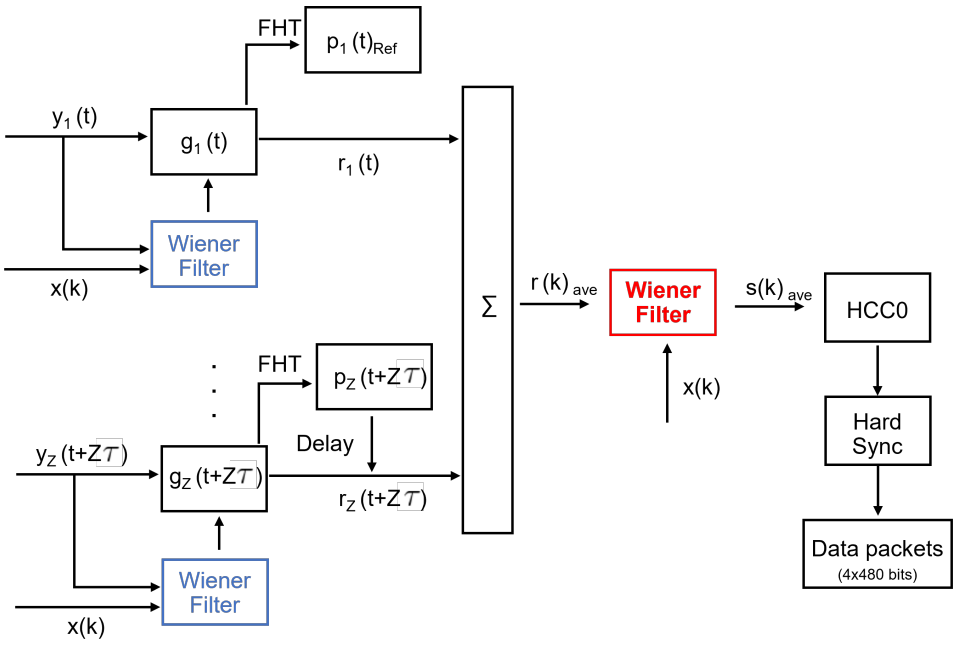

Figure 5.4: Diagram of the double Wiener filter communication system, for a single channel, shows the following steps: channel equalization (single Wiener filter), soft synchronization, temporal coherent averaging of Z received bitstreams, double Wiener filter over the averaged bitstream, probe interference removal (HCC0), hard synchronization, and data retrieval.

5.2.2 Double Wiener filter coefficients

Calculated in a similar way to the first Wiener filter , shown in Sec. 2.6, but over the averaged sequence $r(k)_{ave}$, the second Wiener filter coefficients $W(\gamma)$ compensate the residual intersymbol interference (5.2)

$$\mathbf{W} = \mathbf{R}_{\mathbf{rr}}^{-\mathbf{1}}\mathbf{r}_{\mathbf{xr}} \tag{5.2}$$

The output signal is given by $s_{ave}(k) = r_{ave}(k) * W_L$ or $s_L = W_L r_{ave}$ in matrix form. Then, the HCC0 removes the probe interference, and the hard synchronization is performed,

as detailed in Sec. 2.7.

5.2.3 CIR evolution in time

Fig. 5.5 shows the evolution of the CIR, in 4 locations of the receiver, to illustrate the filtering process described in Fig. 5.4, and to understand the role of coherent averaging of several received bitstreams. The 4 snapshots are marked from 1 to 4, in red. Snapshot #1 shows the multiple CIR estimated from $y_z(t)$ and the severe multipath. In snapshot #2, one can observe a reduction of multipath in $g_z(t)$ after the first Wiener filter. Snapshot #3

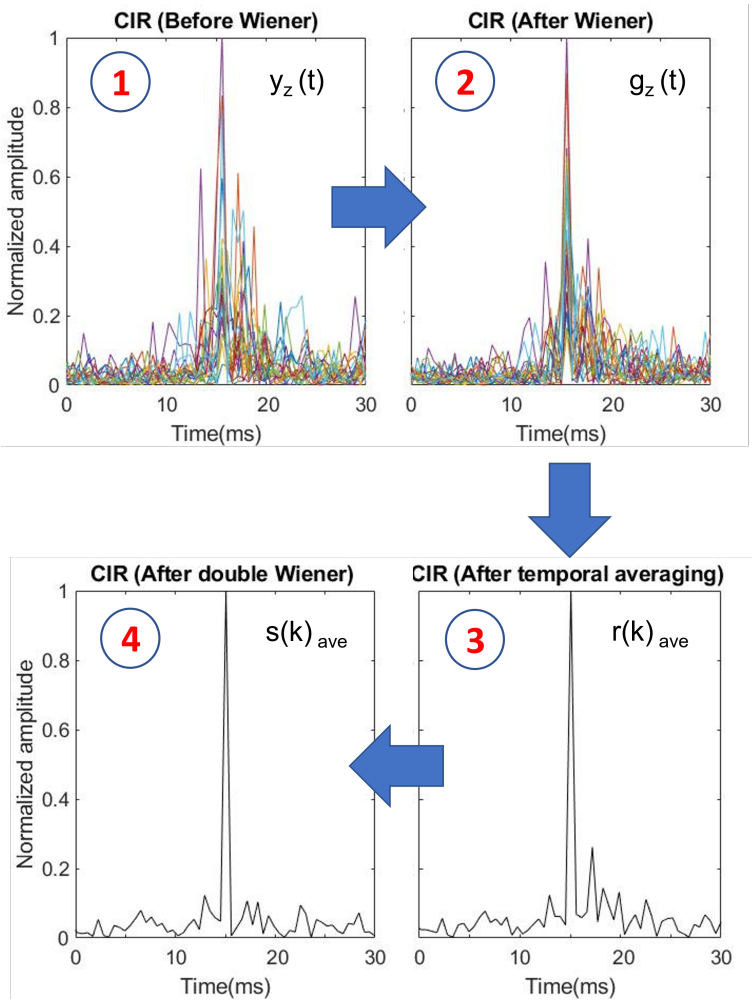

Figure 5.5: The 4 snapshots indicate the evolution of the CIR. Snapshots #1 and #2 show the CIR before and after the Wiener filter. Snapshot #3 shows the CIR after temporal coherent averaging. Snapshot #4 shows the CIR after the second Wiener filter, mitigating the residual ISI.

shows a strong focalization of the pulse energy and a significant reduction of the ISI over the CIR estimated using the temporal averaged bitstream $r_{ave}(k)$. Finally, snapshot #4 shows the CIR estimated from $s_{ave}(k)$, after the second Wiener filter to mitigate the residual ISI. Similar to a Dirac delta function, the CIR points to a significant performance improvement. Despite the low SNR, both the double Wiener and the temporal averaging were able to cope with the severe multipath, reducing the ISI.

5.2.4 Communication performance results

To observe and compare the performance of the single and the double Wiener filter approaches in this challenging environment, a small subset of data from the shallow water BioCom'19 experiment was used. From Jan. 17, 4 p.m. to Jan. 18, 1 a.m., once every hour, the four channels of the pyramidal array were analyzed independently. Doppler is generally an issue in coherent communication systems. However, in this chapter, as the source and receiver were steady in the water, Doppler effects were not relevant. The average SNR was estimated using (2.20), but using only 20 bitstreams ($Z = 20$), where N was estimated from a period after transmissions. The BER were also estimated after averaging 20 bitstreams, from the 55 in each file, equivalent to an effective bit rate of 22 bps. Increasing the number of sequences in the averaging process improves the error correction and tends to provide a better estimation of the transmitted signal, masking the efficiency of the proposed double Wiener filter scheme.

Figure 5.6 (a) shows the SNR vs. BER estimated from all four channels, independently. Despite the power of the transmitted signals being kept constant, SNR levels varied from -5 to 6 dB. This large SNR variation is related to both the channel degradation caused by the

upwelling that reduced the acoustic energy at the receivers, and to the time-varying noise levels in the region, related to man-made and biological factors. The BER is related to the SNR for both filters: the higher the SNR, the lower the BER. However, the double Wiener filter improved the single Wiener filter results, reducing the BER towards the 10^{-2} threshold

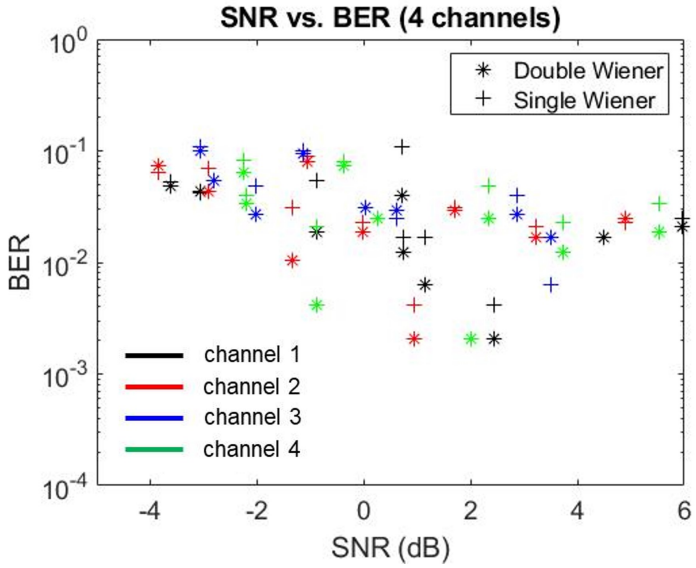

(a)

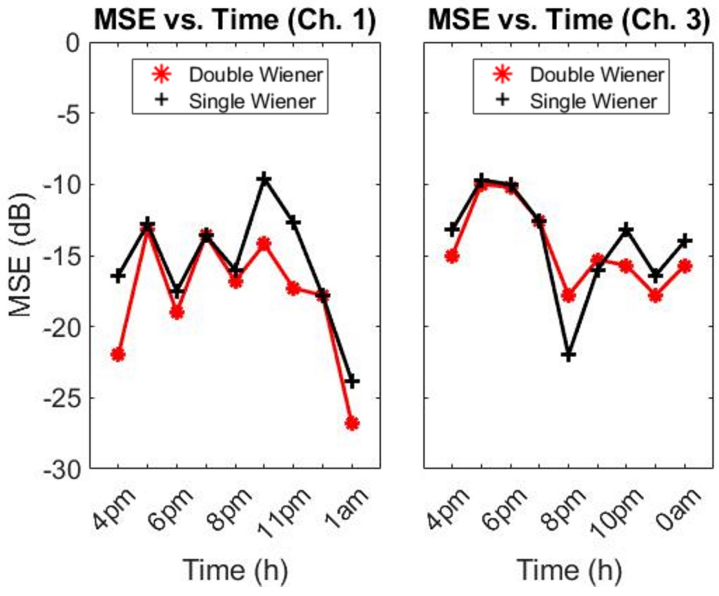

(b)

Figure 5.6: a) SNR vs. BER estimated for the four channels, independently, using both single and double Wiener filter approaches. b) MSE vs. Time estimated for channel #1 and #3 during the upwelling window, to compare the performance of the single and double Wiener filter.

Table 5.3: Average MSE difference ($MSE_{double}-MSE_{single}$) for the 4 channels (dB).

Channel	**Average MSE difference (dB)**
#1	-2.78
#2	-1.81
#3	-0.67
#4	-2.89

in most cases, in all four channels.

To compare the performance of both single and double Wiener filters in terms of BER, during the upwelling window, Fig. 5.6 (b) shows the MSE vs. Time estimated from channels #1 and #3. Furthermore, in Table 5.3, one can observe the average MSE difference between the double and single Wiener filter, in dB, for all four channels. A factor that may have contributed to the achieved BER and MSE results is the severe multipath observed by each hydrophone. Even being separated from each other by just a few wavelengths, the hydrophones presented different multipath structures and noise levels. The hydrophone #3, positioned over the bottom presented a lower averaged MSE difference compared to the hydrophone #1 at the top of the array. But in all channels, the double Wiener filter outperformed the single Wiener filter providing an average mean square error gain of up to 2.8 dB.

5.3 Discussion

In the first section of this chapter, we performed an analysis of the impact of temporal and spatial coherence over low SNR communications in an upwelling environment. Furthermore, we defined a criteria to perform multichannel combining based on both temporal and spatial coherence. Using low power data from both vertical linear and pyramidal arrays, temporal coherence was estimated before and after equalization to show the impact of multipath over

data retrieval. The results indicate that TCOH and SCOH can be used as criteria to combine consecutive signals and multiple channels of the arrays. In the second section, we presented a double Wiener filter approach. The proposed approach applies a Wiener filter over each received bitstream. Then, a second Wiener filter is estimated over the averaged sequence to remove any residual intersymbol interference, improving the signal coherence. To evaluate the performance, the four channels of the pyramidal array were processed independently. Despite BER fluctuation in time, the double Wiener filter approach proved robust in dealing with these short time scale signal fluctuations, and high noise levels that hamper efforts to recover the message.

Chapter 6

Superimposed training passive time reversal for low SNR communications

Abstract *This chapter presents a superimposed training passive time-reversal (STpTR) approach to deal with the acoustic channel response mismatch between the probe and the message transmissions. The proposed method uses a real-time Doppler corrected probe to estimate the channel and perform pTR. The chapter compares 3 alternative strategies: the temporal diversity provided by consecutive signals of the same content, the spatial diversity provided by two different geometry arrays of 4 hydrophones, and a combination of both with 8 hydrophones. Section 6.1 presents the passive Time-Reversal issue and the proposed solution using superimposed training signals. The communication system is detailed in Section 6.2. The communication system performance is presented in Section 6.3. Section 6.4 concludes the chapter, discussing the results and the feasibility of the proposed method for LPD communications.*

6.1 The passive Time-Reversal issue and the proposed solution

PTR usually relies on a spatio-temporal matched filter estimated by a probe sent before the data and requires a receiver array. In the absence of noise and considering that neither the channel oceanographic structure nor the geometry between source and receiver has changed, the received probes can be time-reversed and used to filter the message. However, in the case of moving platforms and variable source-receiver geometries, especially in a fast time-varying

ocean waveguide where coherence time may be short, the classic approach of pTR sending the probe ahead of data may not be able to cope with the environmental mismatch between the probe and the message transmissions, even at high SNR [10, 27, 29]. Therefore, this chapter presents an alternative for the pTR channel mismatch due to the environmental variability between the probe and the data transmissions, for single and multichannel systems, based on a low-power superimposed training method [60]. At the receiver, the superimposed training pTR (STpTR) approach performs multipath recombination. A Wiener filter removes the residual ISI. The method explores both temporal diversity, provided by consecutive signals of the same content, and spatial diversity provided by an array of hydrophones. Coherent averaging of low power signals increases the SNR at the receiver and performs error correction.

To prove the concept, this chapter relies on a subset of data from the Biocom'19 shallow water experiment [51], detailed in Sec. 4.2. Low power signals were transmitted from a single source and recorded by pyramidal and vertical linear arrays (VLA), with 4 hydrophones each. The received signals were processed independently and combined. A more complex and spatially spread system composed of all 8 hydrophones was also studied to understand the tradeoff between the system robustness, effective bit rate, and the number of receivers.

Despite most LPD systems are based on direct sequence spread spectrum (DSSS) which could be used as benchmark, the STpTR signal structure is different. Thus, a previous method based on a Wiener filter, described in Sec. 2.6, is used as a reference. Performance is compared using STpTR alone, and STpTR as a pre-Wiener equalizer.

6.2 Superimposed training passive time-reversal

The STpTR concept relies on the same superimposed training bitstream, described in Sec. 3.2. The same low power bitstream is also transmitted Z times, but recorded by several receivers. The redundancy of signals in both time and space allows error correction and multichannel gain through coherent averaging.

The following subsections discuss the receiver structure according to the block diagram of Fig. 6.1. Fig. 6.1 (a) shows the STpTR, channel equalization, soft synchronization in time, and coherent averaging of Z low power bitstreams. Fig. 6.1 (b) shows the multichannel combining, hyperslice cancellation by coordinate zeroing (HCC0), hard synchronization, and message retrieval.

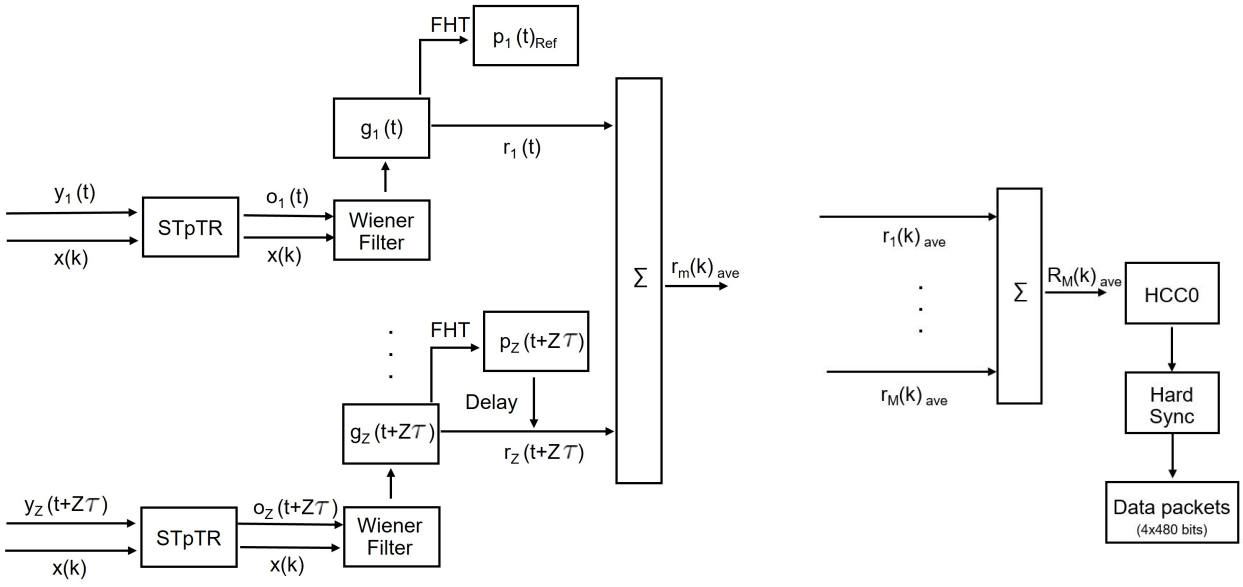

Figure 6.1: a) Diagram of STpTR, channel equalization, soft synchronization in time, and coherent averaging of Z low power bitstreams; b) Diagram of multichannel combining, HCC0, hard synchronization, and message retrieval.

6.2.1 Detection and Doppler compensation

In a reverberating channel or in the presence of relative motion between source and receiver, Doppler frequency spread/shift of transmitted binary probes must be compensated to improve detection and synchronization [7, 18, 29]. In shallow water, the signal arrives through multiple paths that may be subject to different time-scaling factors [63]. Assuming that all paths have approximately the same Doppler-scaling factor, each z received bitstream $y_z(t + z\tau)$ is correlated with a bank of matched filters composed replicas $x(t)_{f'_c}$, frequency-shifted to f'_c, for expected source-receiver velocities.

The resulting dynamic Doppler index ($I_{Dop_{f'_c}}$) is based on the maximum absolute value of the correlation, in bandpass, given by (6.1)

$$I_{Dop_{f'_c}} = max[|\tilde{y}_z(t + z\tau) * \tilde{x}^{\dagger}(-t)_{f'_c}|] \tag{6.1}$$

where $\tilde{x}^{\dagger}(-t)_{f'_c}$ is a bandpass time-reversed frequency-shifted replica known to the receiver. Then, the bitstream is resampled for the f'_c corresponding to the highest $I_{Dop_{f'_c}}$.

During the BioCom'19 experiment, Doppler was studied based on signals recorded by a hydrophone hanging from a drifting vessel, approximately 3m below the sea surface. Fig. 6.2 (left) shows the Doppler shift Δ estimated for the moving vessel. The receiver velocity v'_r can be estimated assuming a fixed source, and a reference sound speed of c=1528 m/s observed during the experiment (6.2).

$$v'_r = c\left[\frac{f_c - \Delta}{f_c} - 1\right], \tag{6.2}$$

where Δ is the Doppler shift.

Therefore, the average Doppler shift of Δ_{ave}=−5 Hz corresponds to a vessel drifting

velocity of v=−1.01 m/s, approximately 2 knots, in agreement with the drifting vessel velocity moving away from the fixed source.

Successful STpTR demodulation depends on the efficiency of Doppler compensation. To observe the impact of Doppler correction over detection, Fig. 6.2 (middle) shows the matched filter outputs for signals based on the original center frequency f_c. The peaks are low and several bitstreams were not even detected. However, using a dynamic Doppler frequency f_c' according to the output of (6.1), detection is improved significantly. Fig. 6.2 (right) shows correlation peaks much stronger than those in Fig. 6.2 (middle). The matched filter outputs are also more stable in time, indicating a correct Doppler estimation and resampling of the received signals. After Doppler compensation, each sequence is converted from bandpass to baseband as detailed in Sec. 3.3. Thus, a single 2047-bit baseband bitstream is created containing most of the original bandpass sequence energy.

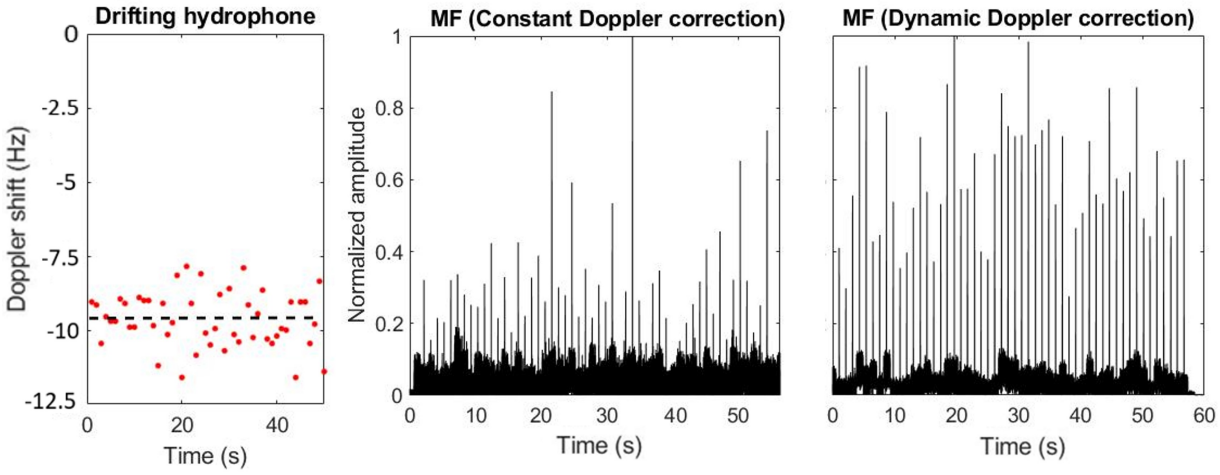

Figure 6.2: Left) Doppler shift estimated from a drifting hydrophone. Middle) Matched filter output for Doppler correction using a constant sampling frequency. Right) Matched filter output for Doppler correction using a dynamic sampling frequency.

6.2.2 STpTR in time, Wiener equalization and temporal soft synchronization

Block diagram in Fig. 6.1(a) describes the STpTR in time, the Wiener equalization, and the temporal soft synchronization. In a noiseless and time-invariant channel, the received signal may be represented by $y_z(t) = s(t) * h_z(t)$, where $s(t)$ is the transmitted bitstream, and $h_z(t)$ is the channel impulse response (CIR). However, ocean waveguides are typically noisy and fast time-varying. Therefore, the superimposed training method approximates a time-varying channel to a linear time-invariant (LTI) during the period of the signal. The probe and the message are transmitted simultaneously. As the probe and the message are using the same sound channel, there is no channel mismatch due to the environmental variability. Thus, the FHT crosscorrelation estimates the noisy CIR $\widehat{h}_z(t)$ using $y_z(t)$ and the known baseband probe for zero Doppler $x(k)$, where k is a discrete time-index.

The STpTR works in time and space. In time, for each sensor, STpTR acts like a single matched-filter convolving received bitstreams $y_z(t)$ with their own time-reversed CIR $\widehat{h}_z(-t)$ (6.3).

$$o_z(t') = y_z(t') * \widehat{h}_z^{\dagger}(-t') = s(t') * \left[h_z(t') * \widehat{h}_z^{\dagger}(-t')\right] \tag{6.3}$$

where $t' = t + z\tau$ is the z bitstream time slot. To avoid the inclusion of excessive noise in the matched filtered bitstream $o_z(t')$, the CIR $\widehat{h}_z(-t')$ is time-gated, in a trial and error process, to include only the main arrivals. The result is the focusing of the weak pulse energy, after multipath recombination. However, there is always a residual ISI, which requires equalization to be eliminated [18, 29].

In this work, the STpTR will be followed by an adaptive Wiener filter equalizer [45, 47, 48, 64, 65]. Reducing the length of multipath, STpTR as a pre-equalizer also reduces the

length n of the Wiener filter, avoiding ill-conditioning that could result in a unstable matrix inversion [64,65]. For each channel m, $g_z(t')$ are time-aligned based on the strongest peak of $p_z(t')$, where $p_{1ref}(t')$ is the reference. After soft synchronization, Z sequences are averaged providing a high SNR bitstream $r_m(k)_{ave}$ (6.4).

$$r_m(t')_{ave} = \frac{1}{Z}\sum_{z=1}^{Z} g_z(t') = s(t') * \left[\frac{1}{Z}\sum_{z=1}^{Z}\left[w_z(t') * h_z(t') * \widehat{h}_z^{\dagger}(-t')\right]\right] \tag{6.4}$$

6.2.3 STpTR, and soft synchronization in space

The $r_m(t')_{ave}$ is calculated for all M elements of the array (Fig. 6.1(b)). The synchronization in space is similar to that performed in time. The output of the STpTR $R_M(t')$ is obtained after coherent averaging all M channels (6.5).

$$R_M(t') = \frac{1}{M}\sum_{m=1}^{M} r_m(k)_{ave} = s(t') * \left[\frac{1}{MZ}\sum_{m=1}^{M}\sum_{z=1}^{Z} w_z(t') * h_z(t') * \widehat{h}_z^{\dagger}(-t')\right] \tag{6.5}$$

where the term in brackets may be interpreted as the Q-function [27, 44], modified by the Wiener coefficients. The Q-function is represented by the summation of the autocorrelation of the channel impulse responses as a function of the number of receivers [29, 44]. Main lobe contributions of different sensors add up in phase. However, secondary lobes are not aligned in delay and phase, not reinforcing each other. The temporal focusing is indicated by the peak-to-sidelobe (PSL) ratio that depends on factors such as the multipath structure, the number of receivers and their spatial distribution, and the SNR [29, 44]. As the Q-function approaches a Dirac delta function, the performance of the STpTR increases.

6.2.4 Probe interference cancellation

To remove the probe from the time/space averaged bitstream $R_M(k)$, the HCC0 process is applied. Described in Section 2.7, HCC0 removes the probe interference and applies an inverse FHT to decompress the message energy.

6.2.5 Hard synchronization and message retrieval

A hard synchronization is performed using cross-correlation peaks from FHT of Mseq31 which precedes data packets [60]. After synchronization, the receiver retrieves the four 480-bit payloads.

6.3 STpTR communication performance

A small subset of data from BioCom'19 (Sec.4.2), recorded on Jan 17, 2019, between 1:10 p.m and 2:30 p.m, at both linear and pyramidal arrays, was used to prove the STpTR concept. The nautical chart (Fig. 6.3 (left)) shows the propagation path. Fig. 6.3 (right) shows the SSP acquired at 1:38 p.m at the source and receiver locations and the bottom depression located at the bay entrance. The slightly downward refracting sound speed profiles indicate that sensors close to the bottom may receive more acoustic energy compared to those placed along the water column.

To evaluate the proposed communication system performance in a low SNR environment, the signal power was kept constant during the first 30 minutes, and reduced by 1 dB after each transmission, in the remaining 30 minutes. The signal power variation in addition to the high impulsive noise levels in the site, related to both man-made and biological factors, provided a wide SNR variation for data analysis. The average in-band SNR (dB)

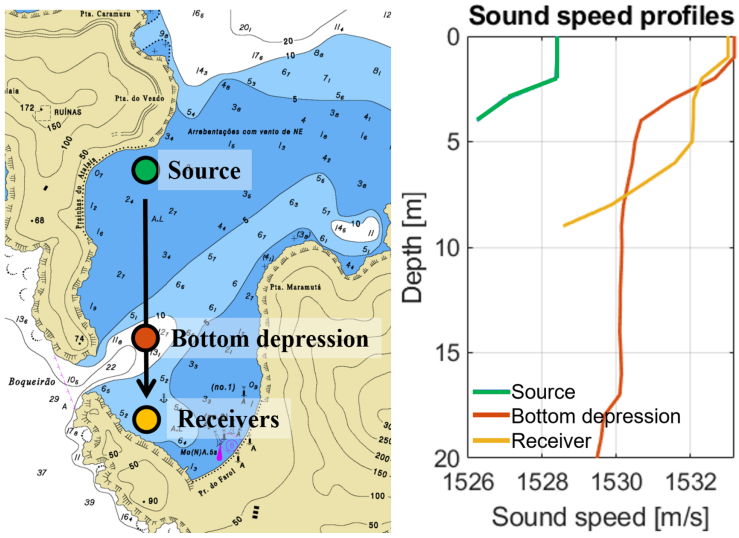

Figure 6.3: Left) Nautical chart indicates the propagation track. Right) Sound speed profiles acquired by a CTD on Jan 17, 2019 at 1:38 p.m at the source (green), receiver (yellow), and bottom depression (red) locations .

for independent channels was estimated according to (2.20), where N was estimated from a period after transmissions. For multichannel combining, the average input SNR of the array was estimated using (2.21).

Fig. 6.4 shows the Doppler shift estimated from bitstreams recorded on Jan 17, 2019, at 1:15 p.m., by all 8 sensors from both arrays. Fig. 6.4 (left) shows the Doppler shift for the pyramidal array (PA), varying from -1.9 Hz to +1.6 Hz. The average standard deviation (σ_{PA}) of the Doppler shift among the 4 channels is 0.9 Hz. As the hydrophones were fixed, σ_{PA} may be related to the small random displacements of the anchored source, the sea surface state, or local currents. Fig. 6.4 (right) shows the Doppler shift for the VLA, varying from -2.2 Hz to +2.4 Hz. The hydrophones on the VLA moved randomly around the vertical equilibrium position. Sensor #4 the most far from the array anchor point presented longer displacements than sensor #1 closer to the bottom. The VLA sensors and the source moving simultaneously contributed to generating an average standard deviation (σ_{VLA}) of the Doppler shift equal to 1.4 Hz, larger than σ_{PA}.

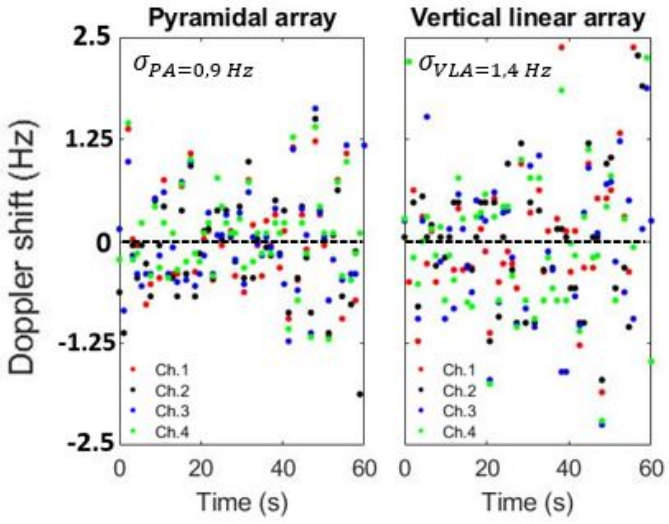

Figure 6.4: Left) Doppler shift estimated from 55 bitstreams recorded on Jan 17, 2019 at 1:15 p.m. Doppler shift and the average standard deviation among the 4 channels of the pyramidal array ($\sigma_{PA} = 0.9Hz$). Right) Doppler shift and the average standard deviation among the 4 channels of the vertical linear array ($\sigma_{VLA} = 1.4Hz$)

Fig. 6.5 shows the matched-filter (MF) outputs for comparing the 55 consecutive Doppler compensated bitstreams (Jan 27, 2019 - 1:15 p.m.). The correlation results from each channel were normalized to the maximum peak of each array. Fig. 6.5 (upper row) shows that the hydrophones from the pyramidal array, separated by approximately 5 wavelengths at f_c = 7.5 kHz, recorded uncorrelated signals. The SSP points to a stable propagation region close to the bottom, ensonifying the hydrophones evenly. Conversely, Fig. 6.5 (lower row) presents the matched-filter outputs for the VLA hydrophones. Placed along the water column, VLA element spacing is 7.5 wavelengths at f_c, providing a broader spatial diversity compared to the smaller pyramidal array. The VLA sensor #1 closer to the bottom received more acoustic energy and presented stronger correlation peaks, compared to sensor #4, closer to the sea surface. The VLA correlation peaks exhibit a more aggressive time-varying fading compared to those of the pyramidal array. Between 55 and 60 seconds, most bitstreams were barely detected by all hydrophones due to a source power level reduction. The amplitude

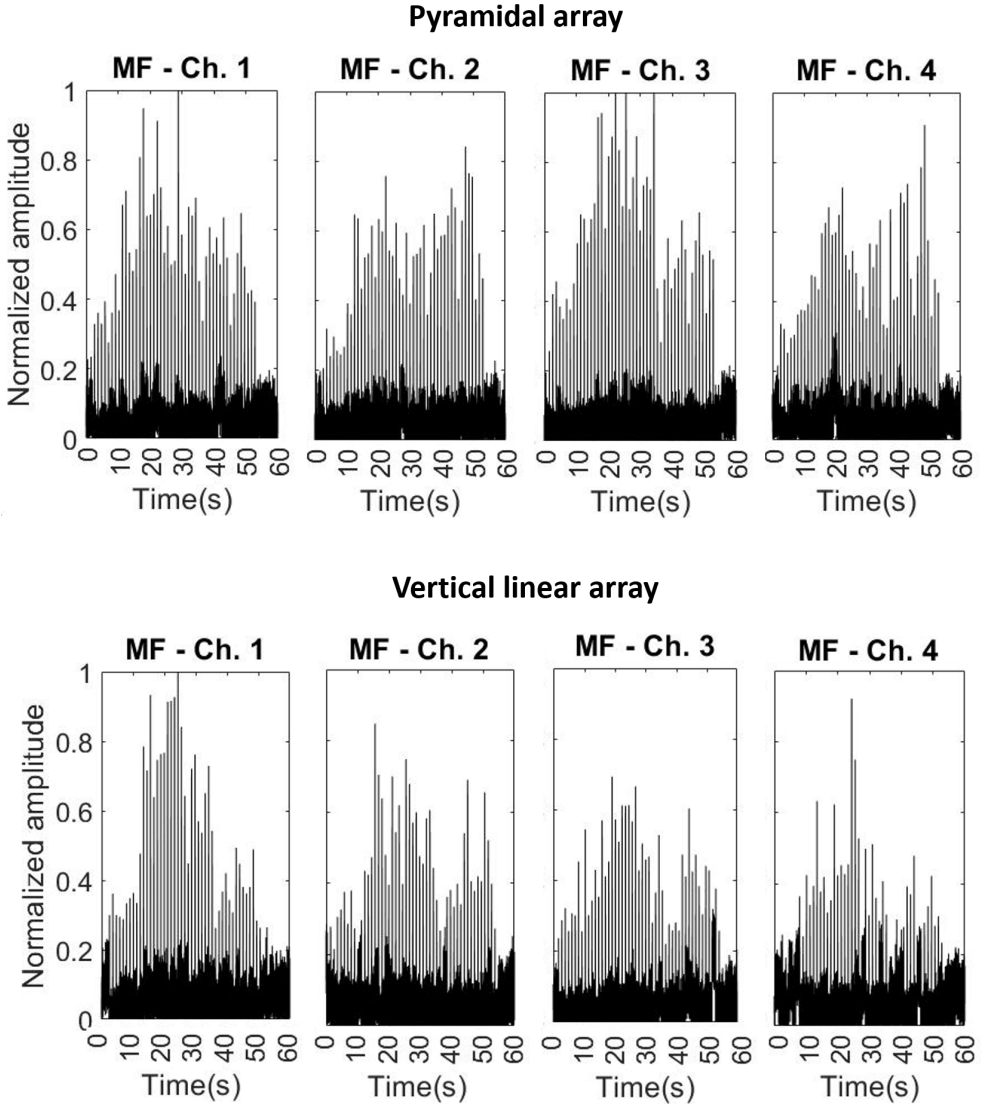

Figure 6.5: Matched filter (MF) outputs from 55 Doppler compensated bitstreams, recorded on Jan 17, 2019 at 1:15 p.m. Upper row: MF from each channel of the pyramidal array. Lower row: MF from each channel of the VLA.

fluctuation (fading) of the dominant correlation peaks, in both time and space, above the background noise points to a challenging environment for communications.

6.3.1 Single receiver

Fig. 6.6 presents the estimated CIR, STpTR pulse compression, and Q function using the first 5 Doppler compensated bitstreams (Jan 27, 2019 - 1:15 p.m.) recorded by two representative sensors. Fig. 6.6 (upper row, left) details the multipath structure of the normalized and

time-aligned CIR estimated from hydrophone #1 placed at the top of the pyramidal array. Located approximately 1 m above the bottom, the CIR present multiple strong arrivals and short multipath. Fig. 6.6 (lower row, left) shows the CIR estimated from hydrophone #4 of the VLA, placed approximately 2.5 m below the sea surface. The CIR present a delay spread longer than 15 ms, including energetic late arrivals that may complicate the synchronization and equalization processes.

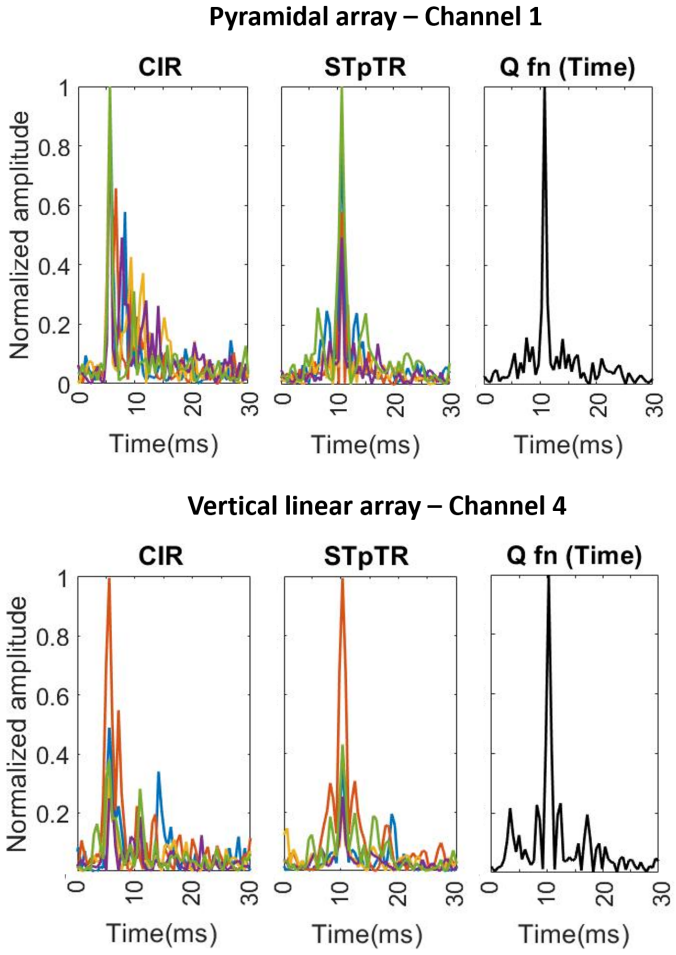

Figure 6.6: Channel impulse responses, STpTR multipath recombination, and the Q-function in time for the first 5 received bitstreams recorded on Jan 17, 2019 at 1:15 p.m. Upper row: CIR, STpTR , and Q-function for channel #1 of the pyramidal array. Lower row: CIR, STpTR, and Q-function for channel #4 of the pyramidal array.

Before implementing the matched-filter, the estimated CIR $\widehat{h}_z(-t')$ in (6.3) was time-gated to 20 ms to include only the main arrivals and to mitigate noise interference. Fig. 6.6

(middle) demonstrates the ability of the STpTR to overcome these harsh conditions and perform the multipath recombination for each sequence, independently. The sharpness of the resulting focus depends on the multipath structure as one can compare in Fig. 6.6 for sensor #1 from the pyramidal array (upper row, middle) and sensor #4 from VLA (lower row, middle). The remaining sidelobes are related to the residual ISI. Thus, STpTR is followed by a Wiener filter equalizer. Considering the Wiener coefficients in (6.3) equal to one, the STpTR is analyzed for one sensor (M=1) of each array to compare the Q function for different propagation conditions.

The Q-function in time is obtained after summing the 5 previous matched filtered sequences. The main lobes of the autocorrelation functions add up coherently while the sidelobes interfere destructively. Fig. 6.6 (upper row, right) shows that the Q-function, from sensor #1 (pyramidal array), has a peak-to-sidelobe (PSL) ratio of 8.2 dB. Meanwhile, the Q-function from sensor #4 (VLA), in Fig. 6.6 (lower row, right), presents higher sidelobes with a PSL ratio of 6.1 dB. The sidelobes in channel #4 are not only 2.1 dB higher but also separated from the main lobe by several symbols in time, compared to the previous case. To reduce the sidelobes, and therefore mitigate residual ISI, one can use a higher number of bitstreams taking advantage of the temporal diversity at the cost of a lower effective bit rate.

This work adopts a minimum MSE Wiener filter method as reference [60]. The performances of 2 filter combinations are studied: STpTR and STpTR followed by a Wiener filter (STpTR+W). To observe the communication system performance using a single receiver at different ranges and depths, received bitstreams from each hydrophone were processed and plotted independently. To increase the processing gain and to perform error correction, the

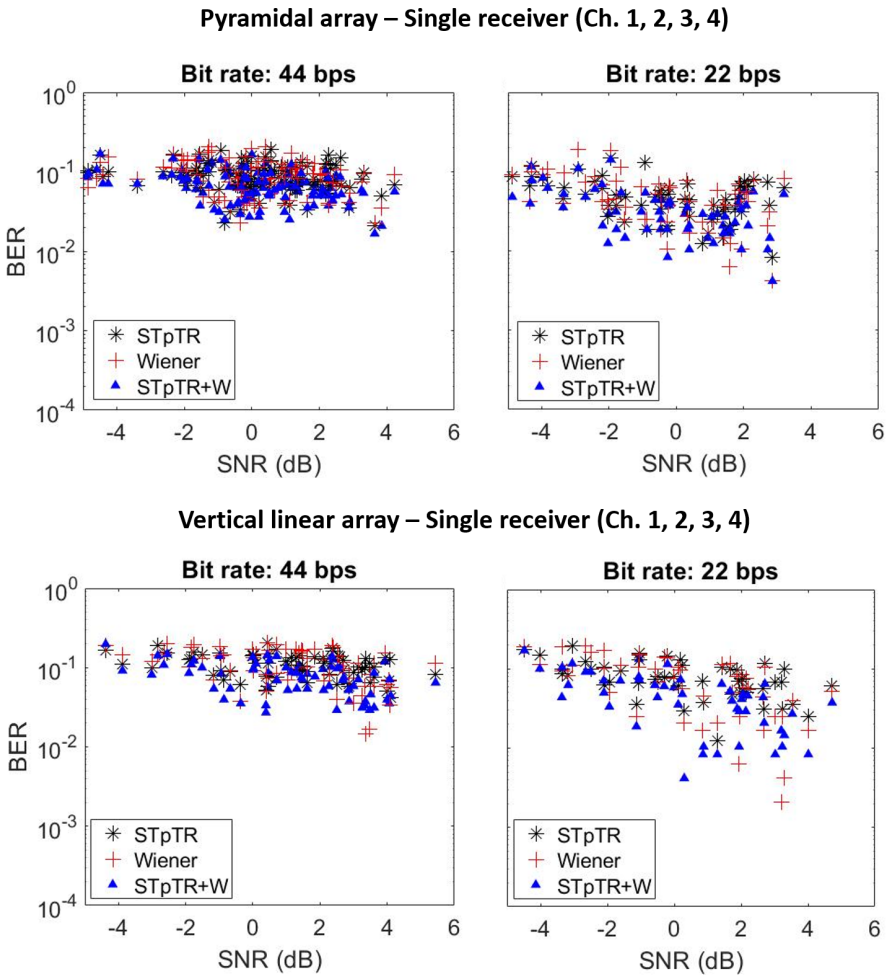

Figure 6.7: BER vs. SNR for STpTR+W (blue triangles), STpTR (black star), and Wiener filters (red cross) from the four channels of the pyramidal array (upper row), and VLA (lower row). Left: 44 bps, averaging for 10.9 seconds. Right: 22 bps, averaging for 21.8 seconds.

bitstreams were averaged for 10.9, and 21.8 seconds (10, and 20 bitstreams), for an effective bit rate of 44, and 22 bps. Fig. 6.7 shows the BER vs. SNR for all four sensors of the pyramidal (top) and the vertical linear array (bottom). The average input SNR varied between -5 and +6 dB during the experiment. In most cases, the BER provided by the STpTR+W (blue triangles) are lower than the BER from STpTR (black star) and Wiener filter (red cross) equalization. However, for several transmissions at high SNR, the Wiener achieved BER lower than STpTR+W probably due to a short multipath spread and to better conditioning of the matrix to be inverted. Lower BER were achieved by averaging for longer

times, increasing the peak-to-sidelobe ratio of the Q-function in time.

Table 6.1 provides the average MSE gain compared to the Wiener filter. For the pyramidal array (Fig. 6.7 (upper row)), the MSE gain from STpTR is -0.33 dB (44 bps) and -0.31 dB (22 bps) indicating a slightly better performance for the Wiener filter. However, when STpTR and Wiener are combined, the MSE gain increases significantly to 1.16 dB and 1.62 dB, for the same bit rates. For the VLA (Fig. 6.7 (lower row)), the MSE gain obtained from STpTR is -0.22 dB (44 bps) and 0.47 dB (22 bps) while STpTR+W provided a gain of 1.49 dB and 1.52 dB. However, despite exploring spatial diversity in a wider sense, sensors from VLA did not improve the performance, significantly, compared to those from the pyramidal array.

Table 6.1: Average MSE gain compared to the Wiener filter(Single channel)

Array	**Pyramidal**		**VLA**	
Bit rate (bps)	44	22	44	22
STpTR+W (dB)	1.16	1.62	1.49	1.52
STpTR (dB)	-0.33	-0.31	-0.22	0.47

6.3.2 Multiple receivers

To explore spatio-temporal multichannel combining, this work analyzes three communication arrays: the pyramidal and vertical linear arrays separately (4 hydrophones), and the combination of both arrays (8 hydrophones).

In Fig.6.8 (left), the Q-fn for the spatial averaging of the 4 hydrophones of the pyramidal array presents a peak-to-sidelobe (PSL) ratio of 10.2 dB compared to the 8.2 dB provided by the channel #1 (Fig.6.6 (upper plot,right)). For the VLA, Fig.6.8 (middle) points to a peak-to-sidelobe (PSL) ratio of 7.6 dB compared to 6.1 dB from channel #4 (Fig.6.6 (lower plot,right)). For the combination of the 8 hydrophones (PA+VLA), Fig.6.8 (right) shows a peak-to-sidelobe (PSL) ratio of 10.96 dB compared to 10.2 dB (PA) and 7.6 dB (VLA).

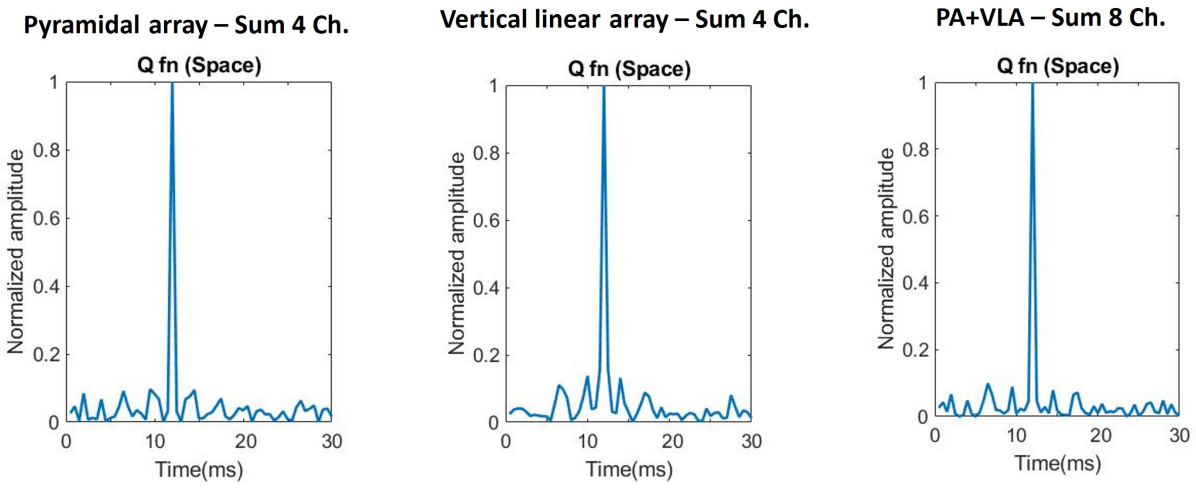

Figure 6.8: Q-function from signals recorded on Jan 17, 2019 at 1:15 p.m. Left/Middle) Q-fn provided by the 4 channels of the pyramidal and vertical linear arrays. Right) Q-fn provided by the sum of all 8 hydrophones.

Therefore, comparing to a single channel Q-function shown in Fig.6.6 (right), Fig.6.8 shows that coherent averaging of multiple sensors, in space, reduces the sidelobes of the Q-function, and therefore, the ISI. This processing gain due to spatial diversity may increase the effective bit rate, reducing the number of averaged sequences. To understand the tradeoff between the temporal and spatial diversity, received bitstreams from both 4-hydrophone arrays were averaged for approximately 4.4, 10.9, and 21.8 seconds (4, 10, and 20 bitstreams), for a bit rate of 110, 44, and 22 bps. For the 8-hydrophone case, a faster communication system is also tested reducing the averaging time to 2.2 seconds, for a bit rate of 220 bps.

Table 6.2 presents the average MSE gain from STpTR+W and STpTR compared to the Wiener filter for channel combining. Different from STpTR which provided similar results to Wiener, but at a lower computational cost, STpTR+W improved the performance of all systems. The pyramidal array (Fig. 6.9 (upper row)) achieved BER similar to those from the VLA (Fig. 6.9 (lower row)) for 110 bps, but much lower BER for the 44 and 22 bps systems, using the same number of sensors. As shown for the single channels, the reason

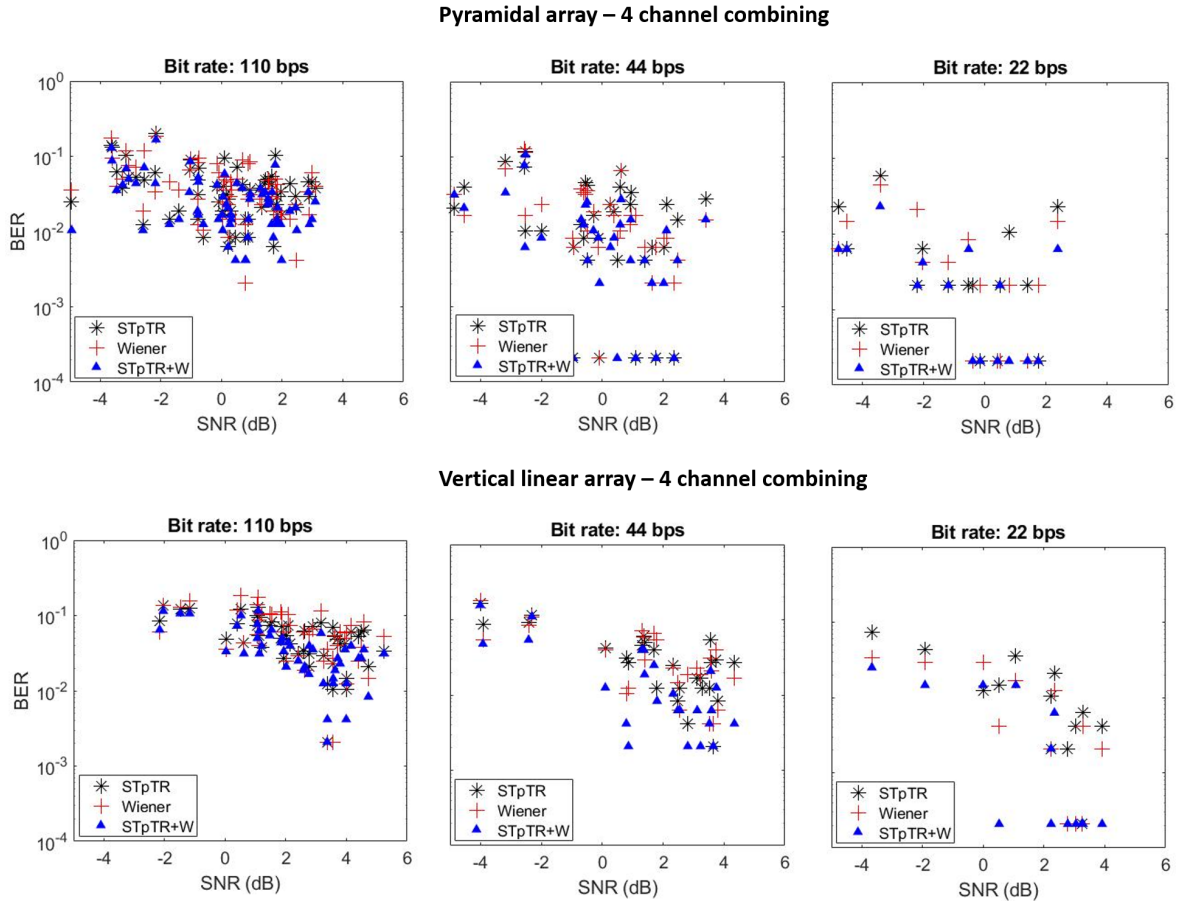

Figure 6.9: BER vs. SNR for STpTR+W (blue triangles), STpTR (black star), and Wiener filters (red cross) for the multichannel combining (4 hydrophones) of the pyramidal array (upper row), and VLA (lower row). Zero BER is represented by $2\text{x}10^{-4}$ on the logarithmic scale. Left: 110 bps, averaging for 4.4 seconds. Middle: 44 bps, averaging for 10.9 seconds. Right: 22 bps, averaging for 21.8 seconds.

may be related to the SSP profile during the transmissions, reducing the acoustic energy at receivers closer to the sea surface, causing synchronization issues. Thus, several bitstreams from sensors #3 and #4 from VLA were discarded reducing the number of results in Fig. 6.9 (lower row). Both arrays, though, provided several BER $< 10^{-2}$ for input SNR in the range -5 to +6 dB, including error-free messages.

Fig. 6.10 presents the performance of the 8-hydrophone communication system, the most complex and spatially distributed array. Separated by approximately 2.8 m, the combination of the pyramidal and VLA provided a significant improvement in the performance and an

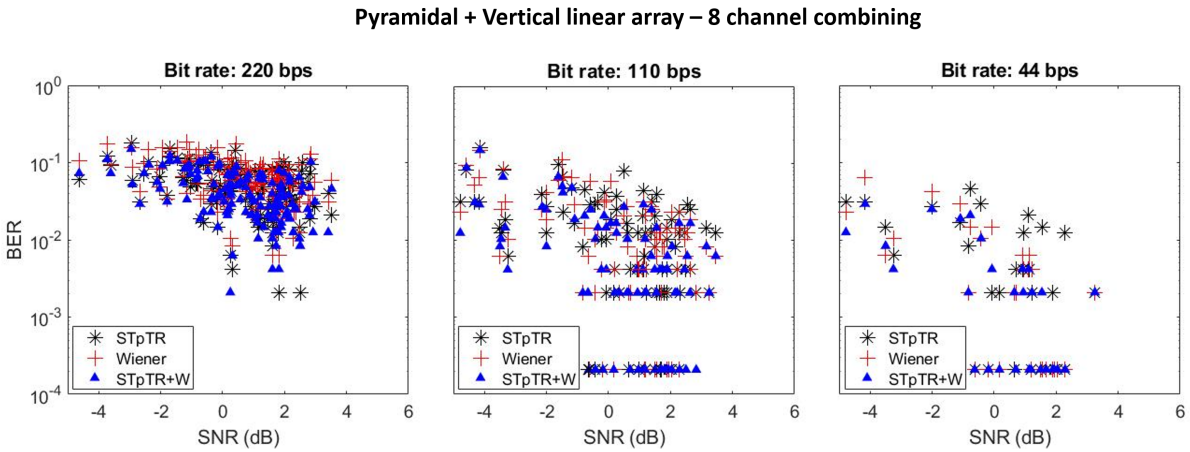

Figure 6.10: BER vs. SNR for STpTR+W (blue triangles), STpTR (black star), and Wiener filters (red cross) for the multichannel combining (8 hydrophones) from the pyramidal array and VLA. Zero BER is represented by $2\text{x}10^{-4}$ on the logarithmic scale. Left: 220 bps, averaging for 2.2 seconds. Middle: 110 bps, averaging for 4.4 seconds. Right: 44 bps, averaging for 10.9 seconds.

increase in the bit rate, as a function of the number of the receivers. The system has shown robust in time, achieving BER $< 10^{-2}$ consistently for the 220 bps system (Fig. 6.10 (left)). For 110 and 44 bps systems (Fig. 6.10 (middle and right)), several error-free messages were also achieved. The reason is the reduction of the Q-function sidelobes due to a higher number of independent sensors, mitigating the ISI. Moreover, temporal diversity also played a role in the performance, reducing the BER for lower effective bit rates.

Table 6.2: Average MSE gain compared to the Wiener filter(Multichannel combining)

Array	**Pyramidal**			**VLA**			**Pyramidal+VLA**		
Bit rate (bps)	110	44	22	110	44	22	220	110	44
STpTR+W (dB)	1.51	1.86	3.13	1.27	1.88	2.34	1.71	1.79	1.92
STpTR (dB)	0.41	-0.02	-0.59	0.76	-0.39	-2.05	0.91	0.27	-0.67

6.4 Discussion

This chapter presented an alternative approach for dealing with the environmental mismatch between the probe and the data transmissions, in passive time-reversal applications for communications. Based on superimposed training low power signals, the method uses a

Doppler corrected real-time probe to estimate the channel and mitigate multipath distortions over data. After STpTR, the residual ISI is treated by the Wiener filter equalizer. Results from the Biocom'19 shallow water experiment proved the concept for single and multichannel receivers. Achieved results show that STpTR may help to reduce acoustic pollution using low-power signals and can be further explored for covert communications. Due to the double synchronization, based on coded sequences known only to legitimate receivers, the method may be said to provide LPI, protecting the privacy of communications. The high noise levels, varying between -5 and +6 dB, combined with the aggressive fading in time and space have impacted the equalization performance. Thus, the method explored both temporal and spatial diversity to increase the SNR and to perform error correction through coherent averaging. Separated by just a few wavelengths, the hydrophones from the pyramidal array observed the channel from almost the same depth. However, their combination provided a higher processing gain than those from the VLA, positioned along the water column. This fact may be related to the temperature stratification of the water column, and therefore, to the downward refracting sound speed profile which directs the acoustic energy to the bottom.

To understand the tradeoff between the number of averaged sequences and the number of receivers, BER vs. SNR was estimated for several bit rates and sensors configuration. The 4-hydrophone arrays achieved BER $< 10^{-2}$, including several error-free messages. A more complex 8-hydrophone array also allowed increasing the bit rate to 220 bps, reducing the integration time. STpTR when operating alone presented a similar performance to the Wiener filter, but at a lower computational cost. The performance was improved using STpTR as a pre-equalizer, providing an average MSE gain of up to 1.62 dB for single channels and 3.13 dB for multichannel combining. Therefore, the use of the STpTR before Wiener

improved the communications, i) reducing the BER, for a fixed bit rate, and ii) allowing an increase of the bit rate, averaging a lower number of bitstreams.

Chapter 7

A study on the VS multichannel combining for LPD communications

Abstract *This chapter presents a study on the low probability of detection communications using a single 2-D vector sensor (VS). A VS experiment took place off the coast of Algarve/Portugal on Nov 24th, 2021. Broadband signals were transmitted from several positions, varying both the source-receiver range and the direction of arrival. Recorded noise was added to the signals to reduce the SNR from 0 to −10 dB. Results show that VS multichannel combining may provide an average SNR and mean squared-error gain of up to 9.4 and 3.1 dB, respectively, compared to the pressure channel. Section 7.1 presents the objective and methodology adopted in this study about vector sensors for LPD communications. The theoretical framework is presented in Section 7.2. In Section 7.3, the EMSO'21 VS experiment is detailed. Section 7.4 explains the noise addition to reduce the SNR, the detection scheme, and Doppler compensation. The LPD communication performance is addressed in Section 7.5. A discussion about the use of VS for LPD communications, based on experimental results, concludes the chapter in Section 7.6.*

7.1 Vector sensors for LPD communications

As shown in Chapter 6, most common systems for covert communications rely on arrays of pressure sensors to deal with multipath and to increase the signal-to-noise ratio (SNR) through multichannel combining. However, these large-size arrays are not suitable for autonomous platforms, such as AUVs. Acoustic vector sensors (VS) are an alternative for con-

ventional hydrophone arrays, being widely employed for sonar applications, such as passive source localization [66], and tracking [67]. Compact in size, the VS measure both the scalar acoustic pressure and the orthogonal particle velocities in a co-located device. However, despite providing diversity gain, just recently the VS started being explored for underwater communications [68–70].

This chapter presents a study on the VS multichannel combining for LPD communications in shallow water. Based on a superimposed training passive time-reversal (STpTR) approach described in Sec. 6.2, this study explores both the temporal diversity provided by repetition of the same signal and the spatial diversity given by the pressure and particle velocity channels. To support this work, a VS communication experiment took place off the coast of Algarve/Portugal on Nov 24th, 2021. A single 2D VS mounted on a tripod was deployed on the bottom. An omnidirectional source hanged from a vessel transmitted broadband bitstreams from several positions, varying both the source-receiver range and the direction of arrival. The bitstream has a low probability of interception (LPI) properties, as the message is embedded in the training sequence [60]. Furthermore, the method employs double synchronization using codes shared between the transmitter and receiver. The bitstreams were acquired in a high SNR. Thus, recorded noise was added to the signals to reduce the in-band SNR from 0 to -10 dB. An arbitrary threshold of SNR< -8dB at the receiver location is considered for benchmark [23]. Experimental results show the suitability of VS multichannel combining for covert communications, providing an average SNR and mean squared-error gain (MSE) gain of 9.4 and 3.1 dB, respectively, compared to the pressure channel.

7.2 Theoretical framework

In this section, the theoretical VS system equations and the superimposed training pTR receiver are briefly presented.

7.2.1 Vector sensor data model

Composed by a pressure sensor and particle velocity channels, the VS system equations can be defined as (7.1).

$$\begin{aligned} y_p &= s * h_p + n_p, \\ y_{v_x} &= s * h_{v_x} + n_{v_x}, \\ y_{v_y} &= s * h_{v_y} + n_{v_y}, \\ y_{v_z} &= s * h_{v_z} + n_{v_z}, \end{aligned} \tag{7.1}$$

where $y_{p,v_{x,y,z}}$ are the received pressure/pressure equivalent particle velocity signals, s is the transmitted signal, $h_{p,v_{x,y,z}}$ are the channel impulse responses of respective pressure/particle velocity channels, and $n_{p,v_{x,y,z}}$ is the additive ambient noise, assumed spherically isotropic. Despite all signals $y_{p,v_{x,y,z}}$ are measured at a single point, previous studies have shown that the pressure and particle velocity channels may provide spatial diversity [69, 70]. Therefore, the approach developed in Chapter 6 for low SNR communications based on both temporal and spatial diversity, using an array of pressure sensors only, may be extended for VS receivers.

7.2.2 Superimposed training pTR receiver

For convenience, the superimposed training passive time-reversal (STpTR), detailed in Sec. 6.2, is summarized in this section.

Fig. 7.1 shows the receiver diagram. The received bitstreams $y_z(t + z\tau)$ are bandpass filtered, Doppler compensated, and converted to baseband. The STpTR convolves each

bitstream $y_z(t + z\tau)$ with its own time-reversed complex conjugate CIR $\widehat{h}_z^{\dagger}(-t)$ (7.2).

$$o_z(t') = y_z(t') * \widehat{h}_z^{\dagger}(-t') = s(t') * \left[h_z(t') * \widehat{h}_z^{\dagger}(-t')\right] \tag{7.2}$$

where $s(t)$ is the transmitted ST bitstream, $t' = t + z\tau$ is the z bitstream time slot, and τ is the period. The Wiener filter remove residual intersymbol interference (ISI). The filtered bitstreams $g_z(t + z\tau)$ are matched filtered with the M-sequence probe $x(k)$. Based on the strongest peak of the cross-correlation results $p_z(t + z\tau)$, the bitstreams $r_z(t + z\tau)$ are synchronized (time-aligned) and coherent averaged, providing a high SNR signal $r_m(k)_{ave}$ and performing error correction, in each m available channel of the vector sensor unit (7.3).

$$r_m(t')_{ave} = s(t') * \left[\frac{1}{Z}\sum_{z=1}^{Z}\left[w_z(t') * h_z(t') * \widehat{h}_z(-t')\right]\right] \tag{7.3}$$

where $w_z(t')$ are the Wiener coefficients, and k is the discrete-time index.

Spatial diversity is also explored through VS multichannel combining. The high SNR averaged bitstream $r_m(k)_{ave}$ from both pressure and particle velocity channels are combined

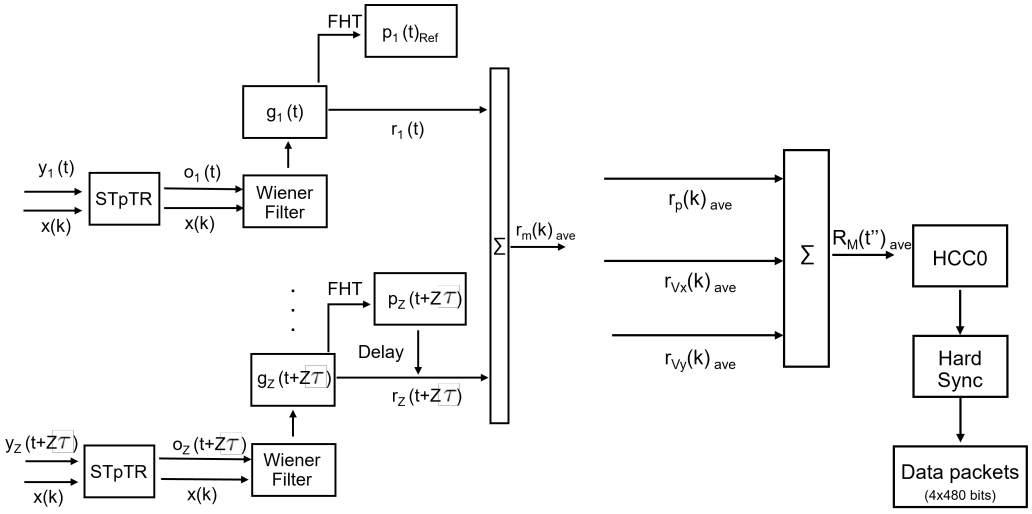

Figure 7.1: Diagram of STpTR, channel equalization, soft synchronization in time, coherent averaging of Z bitstreams, VS multichannel combining, HCC0, hard synchronization and data retrieval.

according to (6.5).

Therefore, a high processing gain may be achieved at the VS receiver taking advantage of both temporal and spatial coherent averaging. After HCC0 and hard synchornization, the message is retrieved.

7.3 The EMSO'21 VS experiment

The EMSO'21 VS experiment took place off the coast of Algarve/Portugal on Nov 24th, 2021 (Fig. 7.2). The experiment deployed a single 2D vector sensor (Geospectrum VS, model 35) that measures both the pressure and the horizontal particle velocities (Vx, Vy), attached at the top of a bottom-mounted tripod. The VS was placed in a 20 m deep water column, approximately 2 m above the bottom. An omnidirectional source (Lubell-916C) hanged from a vessel approximately 7 m below the sea surface, transmitted broadband bitstreams with a central frequency of 7.5 kHz, and bandwidth of 3 kHz, from several locations, varying the source-receiver range and the direction of arrival. The transmissions were performed inside

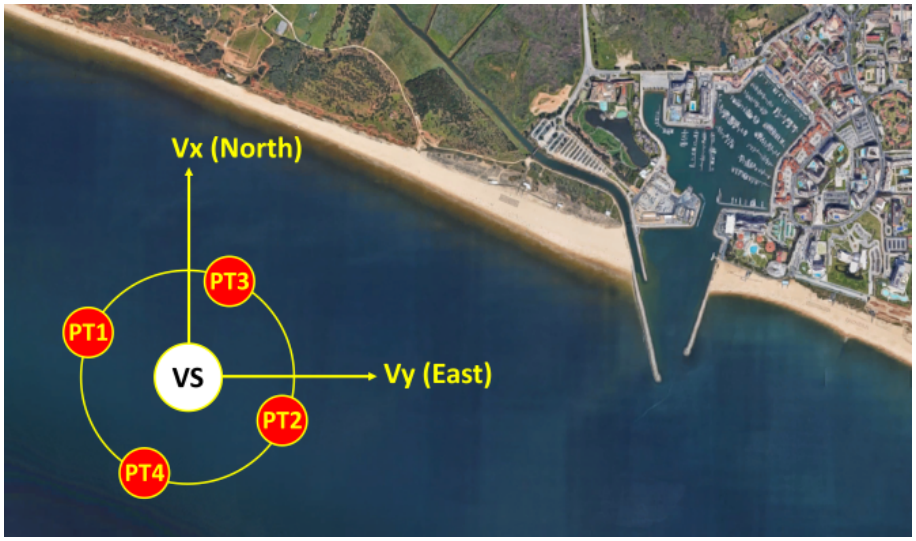

Figure 7.2: (Not to scale) Layout of the EMSO'21 VS experiment indicates four points of transmissions (PT1, PT2, PT3, PT4) placed in an approximately circular area of radius 2 km, centered on the VS.

a circular area of a maximum radius of 2.3 km, centered on the VS. Data recorded from transmissions from 4 locations (PT1, PT2, PT3, and PT4) with the vessel just drifting, and another transmission from PT4 with the vessel moving towards the VS are analyzed. The source to VS range was 1900 m (PT1), 2200 m (PT2), 1250 m (PT3), and 1500 m (PT4). Transmissions from PT1, and PT2 were approximately parallel to the coastline, over the isobath of 20 m, in a predominant E-W direction. The VS Vy channel was pointing to the East. Transmissions from PT3 and PT4 were approximately perpendicular to the coastline, in a predominant N-S direction. The VS Vx channel was pointing to the North. The bathymetry varied from 15 m (PT3) to 30 m (PT4).

7.4 Noise addition, detection and Doppler

The experimental data were received at a high SNR. To simulate a realistic scenario for LPD communications, ambient noise recorded by each channel, at the beginning of the experiment before transmissions, was added to the data files to reduce the in-band input SNR from 0 to -10 dB. The in-band signal-to-noise ratio (SNR), in dB, was estimated for each channel (p, Vx, Vy) and for the VS multichannel combining according to (2.20) and (2.21), respectively. The noise addition and the SNR estimation are detailed in Section 2.8.2.

Assuming that an eavesdropper closer to the receiver location has limited knowledge about the signal, such as the frequency band, conventional detection employs energy detectors. Using the directional information from the Vx channel, Fig. 7.3 shows the power spectrum density of both the background noise (red) and the transmitted signal (blue), filtered in the communication frequency band 6-9 kHz. In Fig. 7.3 (left), the original signal transmitted from PT4, with the vessel in movement, is clearly visible above the noise. How-

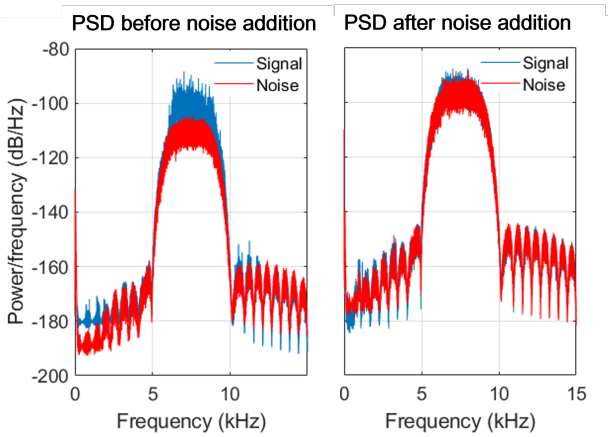

Figure 7.3: Power spectral density (PSD) of background noise (red), and the transmitted signals (blue) from PT4 measured by the Vx channel, and filtered in the band 6-9 kHz. Left) PSD before noise addition. Right) PSD after noise addition.

ever, with an average SNR=−4.7 dB, the signal is barely visible hidden in the noise spectrum (Fig. 7.3 (right)). The pressure and the Vy channel provide even lower SNR, −9.2 dB, and −7.1 dB, respectively. Therefore, the LPD requirement, at the receiver location, may be assumed, and the system performance evaluated.

Fig. 7.4 (left) shows the normalized matched filter outputs for comparing detection of the 55 bitstreams transmitted from PT4, with the vessel moving towards the VS, and recorded by the Vx channel. One can also observe that several bitstreams were barely detected. Doppler frequency shift must be estimated and compensated to improve detection in a low SNR environment. Fig. 7.4 (right) shows that all VS channels tracked the vessel movement, including a sudden acceleration to increase speed. During the first 25 s, the average Doppler shift was 4 Hz, for a vessel speed of 1.5 knots. The Doppler shift rises to 6.2 Hz during the acceleration. The last 20 s show a turbulent period faced by the hanging source until the vessel stabilizes the course and speed around 2.4 knots.

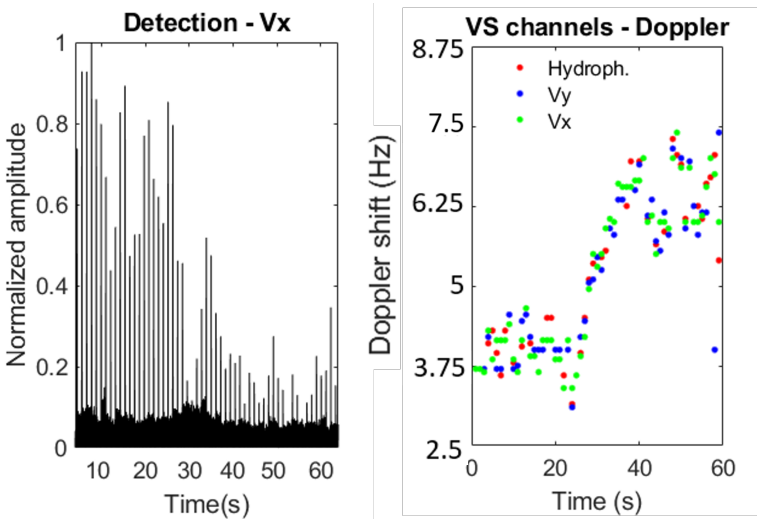

Figure 7.4: Left) Matched filter (MF) outputs, used for detection, from 55 Doppler compensated bitstreams transmitted from PT 4 while the vessel was moving towards the VS, and measured by the Vx channel. Right) Doppler shift estimated from the same bitstreams, for all 3 VS channels.

7.5 LPD communication performance

Fig. 7.5 (left) shows the CIR estimated from signals transmitted from PT4 while the vessel was moving towards the VS, and measured by the Vx channel. The CIR present multiple energetic arrivals and a multipath spread longer than 20 ms. To cope with this challenging environment, the CIR used for pTR were time-gated to 25 ms, in a trial and error process, to include only the most representative arrivals. Fig. 7.5 (right) shows the STpTR multipath recombination for each one of the first 10 bitstreams, independently. The average peak-to-sidelobe (PSL) ratio of the resulting STpTR is 4.2 dB.

Fig. 7.6 (left) shows the normalized Q-function, after summing 10 previously matched filtered signals. The ISI is mitigated as the main lobes add up coherently, while the out-of-phase sidelobes fade away. Thus, one can observe a sharp focus with a PSL ratio of 6.8 dB, 2.6 dB higher than the average STpTR PSL ratio. Fig. 7.6 (right) shows the Q-function in space, after VS multichannel combining (p, Vx, and Vy). A significant reduction of the

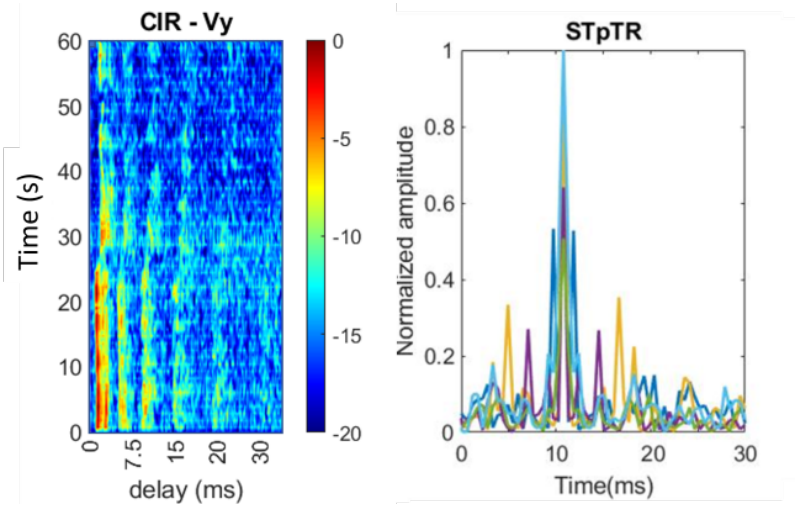

Figure 7.5: Left) 55 channel impulse responses from the bitstreams transmitted from PT4 while the vessel was moving towards the VS, and measured by the Vx channel. Right) STpTR multipath recombination for the first 10 received bitstreams.

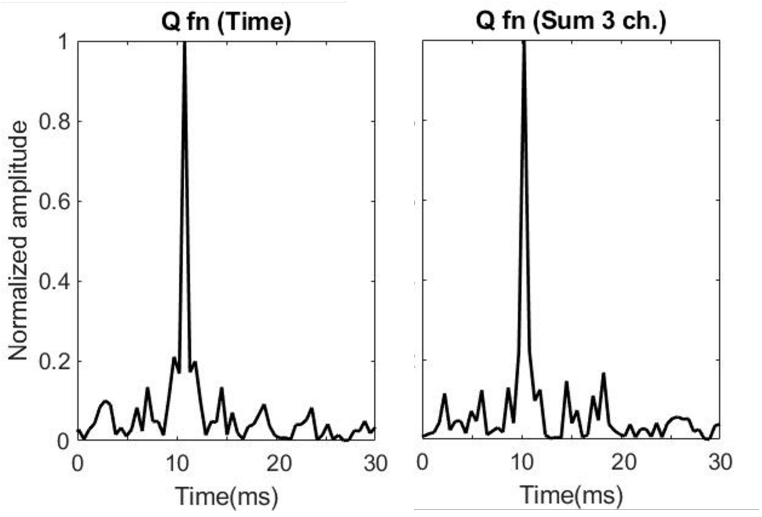

Figure 7.6: Left) Q-function, in time, for the first 10 received bitstreams transmitted from PT4 while the vessel was moving towards the VS, and measured by the Vx channel. Right) Q-function in space, after VS multichannel combining (p, Vx, and Vy)

remaining ISI is observed. The Q-fn in space provided a PSL ratio of 9.6 dB, 2.8 dB higher than the Q-fn in time, pointing to an efficient multichannel combining, even for sensors located at the same point in space. Further reduction of multipath may be achieved using a higher number of bitstreams, to take advantage of temporal diversity but at the cost of a lower effective bit rate. Equalization to mitigate any residual ISI is performed by the Wiener filter.

Fig. 7.7 (upper row) shows the BER performance from signals transmitted from PT1, and PT2, parallel to the coastline, and predominantly aligned to the Vy channel. The

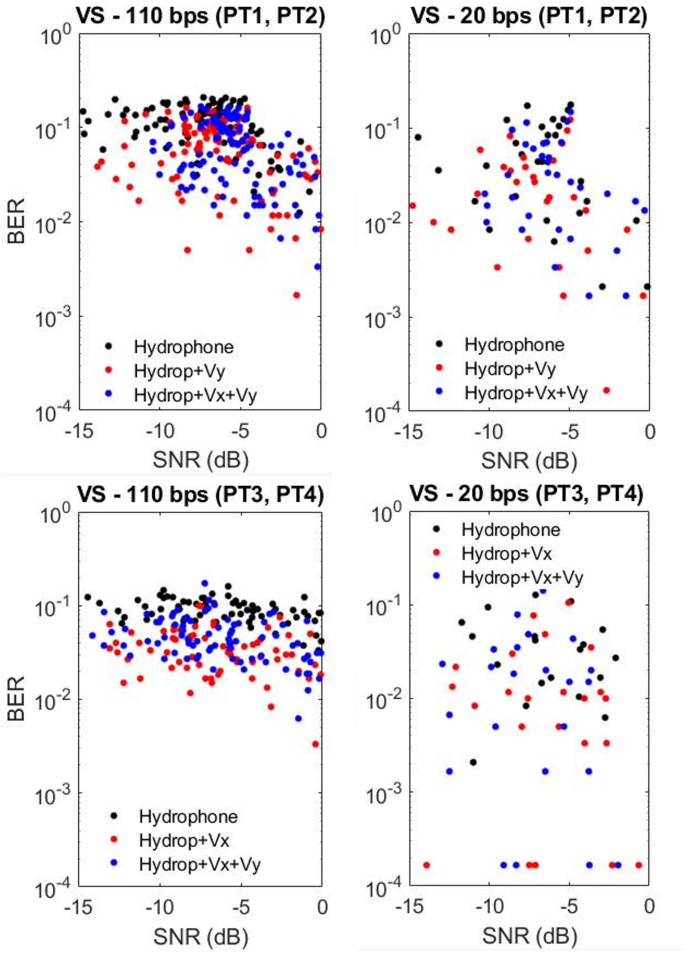

Figure 7.7: BER vs. SNR for 3 VS channel combining: hydrophone (black), hydrophone+Vx or hydrophone+Vy (red), and hydrophone+Vx+Vy (blue). Upper row) Results for PT1, and PT2, for 110 bps (left) and 20 bps (right). Lower row) Results for PT3, and PT4 for 110 bps (left) and 20 bps (right).

BER were estimated for the hydrophone (pressure sensor), for the hydrophone combined with the Vy, and for all 3 channels (hydrophone+Vx+Vy). Fig. 7.7 (lower row) shows the BER from signals transmitted from PT3, and PT4 predominantly aligned to the Vx channel, and perpendicular to the coastline. The same comparison is performed, except that the hydrophone is combined with the Vx channel, instead of Vy. To evaluate the system robustness, the BER were estimated using 4 and 22 bitstreams for an effective bit rate of 110 and 20 bps, shown in Fig. 7.7, left and right, respectively.

7.6 Discussion

In this chapter, the high noise levels needed to keep covertness, and the severe multipath structure contributed to hampering the demodulation of the received signals. Fig. 7.7 shows that the STpTR required a longer coherent averaging, for error correction, to achieve BER $< 10^{-2}$, for SNR between 0 and -10 dB. The objective was to analyse the STpTR performance in a possible covert condition at the receiver location, as shown in the power spectrum density in Fig. 7.3 (right). One can observe in Fig. 7.7 that the combination of the pressure channel to the particle velocity channel approximately aligned to the propagation increased the average input SNR, providing lower BER compared to a single hydrophone. Lower BER were also achieved by averaging a higher number of bitstreams, improving error correction, and therefore, reducing the data rate. However, for any bit rate, the inclusion of the channels perpendicular to the propagation degraded the performance. The LPD benchmark of SNR< -8 dB at the receiver was not defined for directional receivers. Thus, the pressure sensor may be in a LPD condition while the particle velocity channels may have higher SNR, an interesting feature to be explored in LPD communications. To observe the

VS multichannel combining performance compared to a single hydrophone, for the highest bit rate of 110 bps, the average SNR and MSE gain are estimated. For PT1, and PT2 (Fig. 7.7(upper row)), the hydrophone combined with the Vy provided an average SNR and MSE gain equal to 6.9 dB and 2.7 dB. However, for PT3, and PT4 (Fig. 7.7(lower row)), the hydrophone combined with the Vx channel provided a SNR and MSE gain of 7.6 and 3.1 dB. Combining all 3 channels, the resulting SNR and MSE gain are 9.4 dB and 2.4 dB (PT1, and PT2), and 7.6 and 2.8 dB (PT3, and PT4). In all communication scenarios, the VS multichannel combining outperformed the pressure sensor results.

Chapter 8

Conclusions

Abstract *This chapter presents an overview of the work done in this thesis, including the main results, the contributions, and the open questions for future work. Section 8.1 presents the research strategy and the main results. Section 8.2 indicates the published contributions. Section 8.3 states the questions proposed to guide future work.*

8.1 Concluding remarks

This thesis aimed at developing low probability of detection underwater acoustic communications in shallow water. Based on modeled and real data from three shallow water experiments, this thesis studied the impacts of the environment on communications, proposed new signal processing techniques, and integrated them into the state-of-the-art vector sensors. The research strategy to develop LPD communications was to address the different topics separately, to create an overview of possible contributions.

Guided by the objectives stated at the beginning of this work, and considering the LPD threshold of -8 dB [16], a superimposed training method was proposed. The algorithm explored temporal diversity to increase the processing gain and used a Wiener filter for equalization. Experimental results presented bit-error rates (BER) $< 10^{-2}$ for signal-to-

noise ratios (SNR) < -8 dB. To understand the effects of coastal upwelling phenomena over low SNR communications, a study compared the acoustic propagation for different sound speed profiles using a propagation model and analyzed data from the BioCom'19 experiment. Temporal and spatial coherence of low power signals were estimated, and both a criterion for multichannel combining and a double Wiener filter to improve equalization were presented. To address the passive time reversal channel mismatch due to the environmental variability between the probe and the data transmissions, this work proposed a superimposed training pTR approach for single and multichannel systems. Despite the high noise levels, with SNR varying from -5 to +6 dB, the STpTR combined with a Wiener filter achieved BER $< 10^{-2}$, for bit rates up to 220 bps. This work also presented a study about vector sensor multichannel combining. To improve covert communications for AUVs, an experiment using the proposed STpTR approach and a single vector sensor was performed on the coast of Algarve/Portugal. Results indicated that combining the pressure and particle velocity channels of a vector sensor may provide an average SNR and mean squared-error gain of up to 9.4 and 3.1 dB, respectively, compared to the pressure channel.

Therefore, the scientific contributions of this thesis are (i) the proposal of a superimposed training method for LPD communications, (ii) the understanding of the effects of coastal upwelling over communications, and how temporal and spatial coherence are impacted, (iii) the proposal of superimposed training passive time-reversal to avoid the environmental mismatch between the probe and the data channels, and (iv) the vector sensor multichannel combining for LPD communications. A better understanding of the environment and the use of the superimposed training pTR employing a vector sensor may improve the LPD communication system's performance and robustness while keeping covertness.

8.2 Contributions

The contributions of this thesis have been presented in the following publications and conferences:

1. F. B. Louza and H. DeFerrari, "Superimposed training low probability of detection underwater communications", J.Acoust. Soc.Am., vol. 148, no. 3, EL273-278, 2020. https://doi.org/10.1121/10.0001934

2. F. B. Louza and S. M. Jesus, "Coherence as a criterion for multichannel combining low SNR communications in an upwelling environment", Global Oceans 2020: Singapore , U.S. Gulf Coast, 2020, doi: 10.1109/IEEECONF38699.2020.9389147.

3. F. B. Louza and S. M. Jesus, "Low SNR communications using a double Wiener filter in an upwelling environment", 6th Underwater Acoustics Conference Exhibition (UACE2021), https://doi.org/10.1121/2.0001493

4. F. B. Louza and S. M. Jesus, "The effects of upwelling over low SNR communications in shallow water", Oceans Porto/San Diego,2021 - doi: 10.23919/OCEANS44145.2021.9705746

5. F. B. Louza and S. M. Jesus, "Superimposed training passive time reversal for low SNR communications", Submitted to IEEE Journal of Oceanic Engineering, 2022.

6. F. B. Louza and S. M. Jesus, "Low probability of detection underwater communications using a vector sensor", Underwater Communications and Networking Conf. (UComms), 2022 (Accepted).

8.3 Future work

In this work, most proposed objectives were achieved. The thesis of superimposed training pTR low probability of detection underwater acoustic communications has shown feasible. However, there are still open questions. The STpTR communication system characteristics may be adaptive to improve the performance. Furthermore, the communication covertness from an interceptor perspective has not been analyzed, requiring a larger experiment with multiple sensors to estimate the probability of detection from different locations. Therefore, the following questions has been proposed:

- Can the LPD communication system be adaptive, reducing the number of transmitted signals, and therefore, increasing the bit rate?

- Can we reduce the number of Wiener filters for channel equalization, which involves computationally intensive matrix inversion, to improve the system performance? What is the gain using the Wiener over the averaged bitstream $r_{ave_m}(t)$ only, instead of over each received bitstream $y_z(t)$?

- Can the length of the time-reversal window be adjusted, automatically, to improve the multipath recombination?

- How adaptive weighting of the VS channels may improve LPD communications?

- How the STpTR performs from multiple interceptors perpective? Can the STpTR system adaptively modify the probe to message amplitude ratio to improve robustness or covertness, depending on the location of interceptors?

Future work points to long-term field experiments, in different scenarios, to verify the communication covertness from an interceptor perspective, using the proposed methods de-

scribed in this thesis. Therefore, new solutions composed of systems that are able to observe the ocean, and modify parameters adaptively may be achieved. Moreover, integrated solutions using vector sensors may improve significantly the AUVs and submarine communication performance, reliability, and covertness.

Bibliography

[1] M. Stojanovic. *Underwater Acoustic Communication*. John Wiley & Sons, Ltd, 1999.

[2] R.J. Urick. *Principles of Underwater Sound*. Peninsula Publishing, 1983.

[3] A. Palmeiro, M. Martin, I. Crowther, and M. Rhodes. Underwater radio frequency communications. In *OCEANS 2011 IEEE - Spain*, pages 1–8, 2011.

[4] M. Khalighi, C. Gabriel, T. Hamza, S. Bourennane, P. Leon, and V. Rigaud. Underwater wireless optical communication; recent advances and remaining challenges. In *2014 16th International Conference on Transparent Optical Networks (ICTON)*, pages 1–4, 2014.

[5] M. Stojanovic and J. Preisig. Underwater acoustic communication channels: Propagation models and statistical characterization. *IEEE Communications Magazine*, 47(1):84–89, January 2009.

[6] O. C Rodriguez. *Fundamentos de acústica submarina, 1a. Ed.* Universidade do Algarve Editora, 2021.

[7] D.B. Kilfoyle and A.B. Baggeroer. The state of the art in underwater acoustic telemetry. *IEEE J. Ocean. Eng.*, 25(1):4–27, January 2000.

[8] M. Stojanovic, J. A. Catipovic, and J. G. Proakis. Phase-coherent digital communications for underwater acoustic channels. *IEEE J. Ocean. Eng.*, 19(1):100–111, 1994.

[9] W A Kuperman, William S Hodgkiss, Hee Chun Song, T Akal, C Ferla, and Darrell R Jackson. Phase conjugation in the ocean: Experimental demonstration of an acoustic time-reversal mirror). *J. Acoust. Soc. Am.*, 103(1):25–40, 1998.

[10] Joao Gomes, Antonio Silva, and Sergio Jesus. Adaptive spatial combining for passive time-reversed communications. *J. Acoust. Soc. Am.*, 124(2):1038–1053, August 2008.

[11] H. C. Song, W. A. Kuperman, and W. S. Hodgkiss. A time-reversal mirror with variable range focusing. *J. Acoust. Soc. Am.*, 103(6):3234–3240, June 1998.

[12] R. Diamant and L. Lampe. Low Probability of Detection for Underwater Acoustic Communication: A Review. *IEEE Access*, 6:19099–19112, 2018.

[13] P. Van Walree. UUV covert acoustic communications. In *Proc. Underwater Defense Technology (UDT)*, pages 1–8, Hamburg, Germany, 2006.

[14] R. Diamant, L. Lampe, and E. Gamroth. Bounds for Low Probability of Detection for Underwater Acoustic Communication. *IEEE J. Ocean. Eng.*, pages 1–13, 2016.

[15] T. C. Yang. and W B Yang. Interference suppression for code-division multiple-access communications in an underwater acoustic channel. *J. Acoust. Soc. Am.*, 126(1):220–228, July 2009.

[16] T.C. Yang and Wen Bin Yang. Low probability of detection underwater acoustic communications for mobile platforms. In *OCEANS 2008*, pages 1–6, Quebec City, QC, Canada, 2008. IEEE.

[17] R. Schoolcraft. Low probability of detection communications-LPD waveform design and detection techniques. In *MILCOM 91 - Conference record*, pages 832–840, McLean, VA, USA, 1991. IEEE.

[18] M. Chitre, S. Shahabudeen, L. Freitag, and M. Stojanovic. Recent advances in underwater acoustic communications and networking. In *OCEANS 2008*, pages 1–10, 2008.

[19] Editorial underwater acoustic communications: Where we stand and what is next? *IEEE Journal of Oceanic Engineering*, 44(1):1–6, 2019.

[20] G. Leus, P. van Walree, J. Boschma, C. Fanciullacci, H. Gerritsen, and P. Tusoni. Covert underwater communications with multiband OFDM. In *OCEANS 2008*, pages 1–8, Quebec City, QC, Canada, 2008. IEEE.

[21] J. Ling, H. He, J. Li, W. Roberts, and P. Stoica. Covert underwater acoustic communications. *J. Acoust. Soc. Am.*, 128(5):2898–2909, November 2010.

[22] K. Pelekanakis and L. Cazzanti. On adaptive modulation for low SNR underwater acoustic communications. In *OCEANS 2018 MTS/IEEE Charleston*, pages 1–6, 2018.

[23] T. C. Yang and Wen Bin Yang. Performance analysis of direct-sequence spread-spectrum underwater acoustic communications with low signal-to-noise-ratio input signals. *J. Acoust. Soc. Am.*, 123(2):842–855, February 2008.

[24] A. Lempel and M. Cohn. On fast M-sequence transform. *IEEE Trans. Inf. Theory*, 23(1):135–137, 1977.

[25] B. Sherlock, J. A. Neasham, and C. Tsimenidis. Spread-spectrum techniques for bio-friendly underwater acoustic communications. *IEEE Access*, 6:4506–4520, 2018.

[26] Z. Hijaz and V. S. Frost. Exploiting OFDM systems for covert communication. In *2010 - MilCom 2010 Military Communications Conference*, pages 2149–2155, 2010.

[27] H. C. Song, W. S. Hodgkiss, W. A. Kuperman, W. J. Higley, K. Raghukumar, T. Akal, and M. Stevenson. Spatial diversity in passive time reversal communications. *J. Acoust. Soc. Am.*, 120(4):2067–2076, 2006.

[28] S. M. Jesus. Time-Reversal and Spatial Diversity: Issues in a Time-Varying Geometry Test. In *AIP Conference Proceedings*, volume 728, pages 530–538, La Jolla, California (USA), 2004. AIP. ISSN: 0094243X.

[29] Hee-Chun Song. An overview of underwater time-reversal communication. *IEEE Journal of Oceanic Engineering*, 41(3):644–655, 2016.

[30] U. Vilaipornsawai, A. J. Silva, and S. M. Jesus. Underwater communications for moving source using geometry-adapted time reversal and dfe: Uan10 data. In *OCEANS 2011 IEEE - Spain*, pages 1–7, 2011.

[31] L. P. Maia, A. Silva, and S. M. Jesus. Environmental Model-Based Time-Reversal Underwater Communications. *IEEE Access*, 6:10041–10051, 2018.

[32] Jongmin A., Hojun L., Yongcheol K., Sangkug L., and Jaehak C. Mimicking dolphin whistles with continuously varying carrier frequency modulation for covert underwater acoustic communication. *Japanese Journal of Applied Physics*, 58(SG):SGGF05, jun 2019.

[33] S. Liu, G. Qiao, and A. Ismail. Covert underwater acoustic communication using dolphin sounds. *The Journal of the Acoustical Society of America*, 133(4):EL300–EL306, 2013.

[34] P.C. Etter. *Underwater Acoustic Modeling and Simulation, Fourth Edition*. Taylor & Francis, 2013.

[35] M. S. Simoes, F. Xavier, L. Barreira, L. Artusi, H. Macedo, Y. Alvarez, R. Romano, and J Hermand. Medicões geoacústicas em sedimentos marinhos da plataforma continental proxima a Arraial do Cabo/RJ. In *Jornadas de Engenharia Hidrografica*, Lisboa, Portugal, 2012.

[36] K. B. Smith and F. D. Tappert. UMPE: The University of Miami Parabolic Equation Model, Version 1.1. *MPL Technical Memorandum 432*, 1994.

[37] F.B. Jensen, W.A. Kuperman, M.B. Porter, and H. Schmidt. *Computational Ocean Acoustics*. Modern Acoustics and Signal Processing. Springer New York, 2011.

[38] A. Tolstoy, Kevin Smith, and N. Maltsev. The swam'99 workshop - an overview. *Journal of Computational Acoustics*, 09, 11 2011.

[39] K. Smith. Convergence, stability, and variability of shallow water acoustic predictions using a split-step fourier parabolic equation model. *Journal of Computational Acoustics*, 09(01):243–285, 2001.

[40] W. B. Yang and K. Sayrafian-Pour. A low complexity interference cancellation technique for multi-user ds-cdma communications. In *2010 IEEE International Conference on Communications*, pages 1–5, 2010.

[41] H. DeFerrari and A. Rodgers. Eliminating clutter by coordinate zeroing. *J. Acoust. Soc. Am.*, 117(4):2494, 2005.

[42] R. K. R. Yarlagadda and J. E. Hershey. *Hadamard Matrix Analysis and Synthesis With Applications to Communications and Signal/Image Processing*. Springer New York, NY, 1st edition, 1997.

[43] H. S. Chang. *Detection of weak, broadband signals under Doppler-scaled, multipath propagation*. Ph.D. dissertation, Univ. Michigan, Michigan, MI, 1992.

[44] T.C. Yang. Temporal resolutions of time-reversal and passive-phase conjugation for underwater acoustic communications. *IEEE Journal of Oceanic Engineering*, 28(2):229–245, 2003.

[45] W.K. Pratt. Generalized Wiener Filtering Computation Techniques. *IEEE Transactions on Computers*, C-21(7):636–641, July 1972.

[46] B. Farhang-Boroujeny. *Adaptive filters: theory and applications*. Wiley, 2nd edition, 2013.

[47] C.B. Ribeiro, M.L.R. de Campos, and P.S.R. Diniz. A new approach for channel equalization using Wiener filtering. In *GLOBECOM'01. IEEE Global Telecommunications Conference*, pages 290–294, San Antonio, TX, USA, 2001. IEEE.

[48] R. Carvajal, K. Mahata, and J. C. Aguero. Low Complexity Wiener Filtering in CDMA Systems Using a Class of Pseudo-Noise Spreading Codes. *IEEE Communications Letters*, 16(9):1357–1360, September 2012.

[49] D. A. Abraham and M. Siderius. *Underwater Acoustic Signal Processing Modeling, Detection, and Estimation*. ASA Press : Modern Acoustics and Signal Processing : Springer, Cham, Switzerland, 2019.

[50] National Research Council. *Ocean Noise and Marine Mammals*. The National Academies Press, Washington, DC, 2003.

[51] F. B. Louza, J. Osowsky, F. C. Xavier, E. E. Vale, L. P. Maia, R. P. Vio, M. V. S. Simoes, V. Barroso, and S. M. Jesus. Communications and biological monitoring experiment in an upwelling environment at Cabo Frio island bay. In *OCEANS 2019 - Marseille*, pages 1–7, 2019.

[52] P. Hoeher and F. Tufvesson. Channel estimation with superimposed pilot sequence. In *Global Telecommunications Conference. GLOBECOM'99*, volume 4, pages 2162–2166, Rio de Janeireo, Brazil, 1999. IEEE.

[53] W. K. Pratt. Generalized wiener filtering computation techniques. *IEEE Trans. Computers*, C-21(7):636–641, 1972.

[54] J. Kämpf and P. Chapman. The functioning of coastal upwelling systems. In *Upwelling Systems of the World (Springer International Publishing)*, pages 31–66, 2016.

[55] S. Coelho-Souza, M. S. López, J. D. Guimarães, R. Coutinho, and R. N. Candella. Biophysical interactions in the Cabo Frio upwelling system, southeastern Brazil. *Brazilian Journal of Oceanography*, 60:353–365, 2012.

[56] L. Calado, O.C. Rodriguez, G. Codato, and F.C. Xavier. Upwelling regime off the Cabo Frio region in Brazil and impact on acoustic propagation. *J. Acoust. Soc. Am.*, 143(3):EL174–EL180, 2018.

[57] M. Siderius, M. B. Porter, P. Hursky, V. McDonald, and the KauaiEx Group. Effects of ocean thermocline variability on noncoherent underwater acoustic communications. *J. Acoust. Soc. Am.*, 121(4):1895–1908, April 2007.

[58] A. Chen-Tung and F. Millero. Speed of sound in seawater at high pressures. *J. Acoust. Soc. Am*, 62:1129–1135, 11 1977.

[59] E. L. Ferreira, J. E. A. Goncalves, and R. Coutinho. Community structure of fishes and habitat complexity on a tropical rocky shore. *Environ. Biol. Fishes*, 61:353–369, 2001.

[60] F. B. Louza and H. A. DeFerrari. Superimposed training low probability of detection underwater communications. *J. Acoust. Soc. Am.*, 148(3):EL273–EL278, September 2020.

[61] H. A. DeFerrari. Observations of low-frequency temporal and spatial coherence in shallow water. *J. Acoust. Soc. Am.*, 125(1):EL45–EL49, January 2009.

[62] T C Yang. Measurements of temporal coherence of sound transmissions through shallow water. *J. Acoust. Soc. Am.*, 120(5):2595–2614, 2006.

[63] S. F. Mason, C. R. Berger, and P. Willett. Detection, Synchronization, and Doppler Scale Estimation with Multicarrier Waveforms in Underwater Acoustic Communication. *IEEE J. Sel. Areas in Communications*, 26(9):1638–1649, 2008.

[64] T.H. Eggen, A.B. Baggeroer, and J.C. Preisig. Communication over Doppler spread channels. Part 1: Channel and receiver presentation. *IEEE Journal of Oceanic Engineering*, 25(1):62–71, 2000.

[65] T.H. Eggen, J.C. Preisig, and A.B. Baggeroer. Communication over Doppler spread channels. Part 2. receiver characterization and practical results. *IEEE Journal of Oceanic Engineering*, 26(4):612–621, 2001.

[66] P. Felisberto, O. Rodriguez, P. Santos, E. Ey, and S. M. Jesus. Experimental results of underwater cooperative source localization using a single acoustic vector sensor. *Sensors*, 13(7):8856–8878, 2013.

[67] K. G. Nagananda and G. V. Anand. Underwater target tracking with vector sensor array using acoustic field measurements. In *OCEANS 2017 - Aberdeen*, pages 1–10, 2017.

[68] A. Song, M. Badiey, P. Hursky, and A. Abdi. Time reversal receivers for underwater acoustic communication using vector sensors. In *OCEANS 2008*, pages 1–10, 2008.

[69] A. Song, A. Abdi, M. Badiey, and P. Hursky. Experimental demonstration of underwater acoustic communication by vector sensors. *IEEE Journal of Oceanic Engineering*, 36:454–461, 2011.

[70] F. A. Bozzi and S. M. Jesus. Joint vector sensor beam steering and passive time reversal for underwater acoustic communications. *IEEE Access*, 10:66952–66960, 2022.